Energy Harvesting and Control of a Regenerative Suspension System using Switched Mode Converters

by

Chen-Yu Hsieh

M.ASc. (Electrical and Computer Engineering), Concordia University, 2011
B.Sc. (Electrical and Computer Engineering), University of Ottawa, 2008

Thesis Submitted in Partial Fulfillment of the
Requirements for the Degree of
Doctor of Philosophy

in the
School of Mechatronic Systems Engineering
Faculty of Applied Sciences

SIMON FRASER UNIVERSITY
Fall 2014

Approval

Name:	Chen-Yu Hsieh
Degree:	Doctor of Philosophy
Title:	*Energy Harvesting and Control of a Regenerative Suspension System using Switched Mode Converters*
Examining Committee:	Chair: Dr. Carolyn Sperry, P.Eng. Assistant Profesor, School of Mechatronic Systems Engineering

Dr. Farid Golnaraghi, P.Eng.
Co-Senior Supervisor
Professor

Dr. Mehrdad Moallem, P.Eng.
Co-Senior Supervisor
Professor

Dr. Jiacheng Wang, P.Eng.
Supervisor
Assistant Professor

Dr. Krishna Vijayaraghavan, P.Eng.
Internal Examiner
Assistant Professor
School of Mechatronic Systems
Engineering

Dr. Shahruar Mirab, P.Eng.
External Examiner
Professor
Electrical and Computer Engineering,
University of British Columbia

Date Defended/Approved: December 12, 2014

Partial Copyright License

The author, whose copyright is declared on the title page of this work, has granted to Simon Fraser University the non-exclusive, royalty-free right to include a digital copy of this thesis, project or extended essay[s] and associated supplemental files ("Work") (title[s] below) in Summit, the Institutional Research Repository at SFU. SFU may also make copies of the Work for purposes of a scholarly or research nature; for users of the SFU Library; or in response to a request from another library, or educational institution, on SFU's own behalf or for one of its users. Distribution may be in any form.

The author has further agreed that SFU may keep more than one copy of the Work for purposes of back-up and security; and that SFU may, without changing the content, translate, if technically possible, the Work to any medium or format for the purpose of preserving the Work and facilitating the exercise of SFU's rights under this licence.

It is understood that copying, publication, or public performance of the Work for commercial purposes shall not be allowed without the author's written permission.

While granting the above uses to SFU, the author retains copyright ownership and moral rights in the Work, and may deal with the copyright in the Work in any way consistent with the terms of this licence, including the right to change the Work for subsequent purposes, including editing and publishing the Work in whole or in part, and licensing the content to other parties as the author may desire.

The author represents and warrants that he/she has the right to grant the rights contained in this licence and that the Work does not, to the best of the author's knowledge, infringe upon anyone's copyright. The author has obtained written copyright permission, where required, for the use of any third-party copyrighted material contained in the Work. The author represents and warrants that the Work is his/her own original work and that he/she has not previously assigned or relinquished the rights conferred in this licence.

Simon Fraser University Library
Burnaby, British Columbia, Canada

revised Fall 2013

Abstract

Harvesting road induced vibration energy through electromagnetic suspension allows extension of the travel range of hybrid and fully electrical powered vehicles while achieving passenger comfort. The core of this work is to investigate development of power converters for an electromagnetic suspension system which allows for regeneration of vibration energy and dynamics control of vehicle suspension. We present a variable electrical damper mechanism which can be controlled using unity power-factor AC/DC converter topologies. By controlling the synthesized electrical damper, the system is capable of providing variable damping forces, ranging from under-damped to over-damped cases, while regenerating mechanical vibration energy into electric charge stored in a battery. To demonstate the concept, the developed converter is attached to a small-scale one-degree-of-freedom suspension prototype which emulates a vehicle suspension mechanism. The energy regeneration mechanism consists of a mass-spring system and a ball-screw motion converter mechanism coupled to a DC machine, excited by a hydraulic shaker. The motion converter stage converts vibrational motion into a bi-directional rotatory motion, resulting in generation of back-emf in the rotary machine. We also introduce an optimized start/stop algorithm for the harvesting of energy using the proposed power converter. The algorithm allows for improvements in power conversion efficiency enhancement (≈ 14% under class C road profile) through turning the circuit on/off during its operation. The idea is to ensure that the converter only operates in the positive conversion efficiency region; meaning that when there is enough energy the converter starts the energy harvesting process. Furthermore, an estimation of range enhancement for a full-scale electric vehicle (EV) is furnished using regenerative suspension. It is estimated that for a full size EV (e.g., Tesla model S), a range extension of 10-30% is highly realistic, depending on the road conditions.

Keywords: Energy harvesting, bi- directional switch- mode rectifier, direct AC/DC converter, regenerative Sky-hook control, regenerative suspension system, variable electrical damper.

Dedication

For my parents.

Acknowledgements

I would like to take this opportunity to acknowledge the invaluable technical and personal supervisions by Dr. Farid Golnaraghi, Dr. Mehrdad Moallem. With their strong technical and financial supports allowed me to persevere through the years of my Ph.D study at Simon Fraser University, BC. Moreover, I would like to thank my comitte members Dr. Jiacheng Wang and Dr. Shahriar Mirabbasi from University of British Columbia for taking their time and effort in reviewing my thesis. Lastly, I would like to thank my collegue Mr. Bo Huang for the greatful research collaborations.

Mostly importantly, I would like to express deep gratitudes to my parents, relatives, and Grace Chen for their strong support in making my Ph.D pursing days the most pleasant periods of my academic journey.

Table of Contents

List of Tables

List of Figures

List of Acronyms

SK	Sky-hook
DB- HCC	Double- band Hysteresis Current Control
EPA	Environmental Protection Agency
DOE	Department of Energy
EV	Electric Vehicle
RV	Recreational Vehicle
PV	Photovoltaic
MR	Magnet- rheological
ESR	Equivalent series resistance
SOA	Safe operating area
PWM	Pulse Width Modulation
KVL	Kirchhoff's voltage law
KCL	Kirchhoff's current law
ISO	International Organization for Standardization
PM	Permanent Magnets
DOF	Degree of Freedom
ICE	Internal Combustion Engine
MBC	Magic Body Control
RMS	Root Mean Square
FRF	Frequency Response Functions
DCM	Discontinuous Conduction Mode
VMC	Voltage Mode Code
EMI	Electromagnetic Interference
THD	Total Harmonic Distortion
PF	Power Factor
LRD	Limited Relative Displacement
RS	Rakheja Sankar

Nomenclature

Symbol	Description	Symbol	Description
m	Sprung mass	R_{load}	Terminal Connected Load Resistor
k	Stiffness Coefficient	R_{int}	Motor Internal Resistor
c	Damping Coefficient	L_{int}	Motor Internal Inductance
m_t	Tire Mass	i_{in}	Converter Input Current
L	Inductor	k_e	Motor Torque Coefficient
C	Capacitor	k_t	Tire Stiffness or Motor Torque Coefficient
R	Resistor	k_g	Planetary Gear Ratio
ω	Angular Frequency	m_{eq}	Total Equivalent Mass
ω_n	Resonance Freuqnecy	c_f	Friction Based Damping Coefficient
ζ	Critical Damping Coefficient	F_b	Motor Feedback Force
v	Vehicle Linear Velocity	F_{road}	Force from Road
l	Linear Travel Distance	J_m	Motor Moment of Intertia
$T_{suspension}$	Load Torque	J_b	Ball-screw Moment of Intertia
T_e	Motor Electrical Torque	J_g	Gearbox Moment of Inertia
D	Road Profile Sampling Rate	d	Lead Ratio
G_r	Road Roughness Coefficient	Y	Ground Excitation Amplitude
N	Vector Length	Φ	Power Spectral Density
Z_s	Generator Internal Impedance	Ψ	Pseudorandom Phase
V_x	Terminal Voltage	L_a	Line Inductor
i_{ref}	Reference Current	V_c	Controlled Voltage Source Amplitude
k	HCC Modulation Index	R_s	DC Motor Coil Equivalent Loss Resistor
ΔI	Small Current Error Band	L_s	DC Motor Internal Inductance
i_{err}	Error Current	T_s	EMF Line Period
η_m	Mechanical Domain Effiency	T_{sw}	MOSFET Switching Period
η_e	DC Machine Conversion Effiency	R_{in}	Synthesized Resistor
λ_{rms}	RMS Sprung Mass Acceleration	R_{ref}	Desired Synthesized Resistor
η_{rms}	RMS Relative Displacement	c_{sky}	Sky-hook Damping Ratio
$\overline{P}_L$	Average Harvester Power	$\eta_{AC/DC}$	Switched Mode Converter Efficiency
f_s	Start Sweeping Frequency	D_L	Direct AC/DC Duty Cycle
f_e	End Sweeping Frequency	E_{in}	Converter Input Energy
V_F	Diode Forward Voltage	V_o	Direct AC/DC Load Voltage
i_C	Capacitor Current	$R_{in\ ev}$	Envelope Input Resistance
v_C	Capacitor Voltage	$r_{DS,on}$	MOSFET On-time Resistance
i_L	Inductor Current	r_{ESR}	Inductor Equivalent Series Resistor
J	Rottor Moment of Intertia	i_Q	Direct AC/DC Diode Current
θ	Angular Displacement	P_{in}	Direct AC/DC Input Power
t	Time	$P_{in,SB}$	Synchronous Boost Input Power
P_{loss}	Total Power Loss of Harvesting Circuit	P_{np}	Difference between Available Harvestable Power and Total Power Loss of Harvesting Circuit

P_q	Quiesecnt Power Loss	P_{sw}	Switching Loss
P_{cond}	Conduction Loss	P_{drv}	Gate Driver Loss
P_{aux}	Auxiliary ICs Power Consumption	f_{sw}	Switching Frequency
V_{gs}	Gate-source Voltage	t_{on}	Turn On-time
Q_g	Gate Charge	t_{off}	Turn Off-time
i_t	Conducting Current	V_b	MOSFET Blocking Voltage
V_{th}	Threshold Voltage	T_c	Time Required for Entering Net-positive Region
T_r	Drive Cycle Runing Time	T_i	Idling Time
T_d	Delayed Turn-off Time	Y_t	Sprung Mass Acceleration Amplitude
T_{tot}	Total Driving Duration	μ	Damping Coefficient in Duffings Oscillator
τ	Discharge Constant	σ	Perturbation Detuning parameter
ΔT	Rectfied Voltage Averaging Duration	T_0	Normal Time Scale
c_{eq}	Equivalent Damping Cefficient	T_1	Slow Time Scale
ε	Level of Nonlinearity in Duffings Oscillator	I	Efficiency Improvement
α	Stiffness Coefficient in Duffings Oscillator	x	Sprung Mass Displacement
K	Forced Excitation Amplitude	y	Ground Displacement
ω_o	Resonance Frequency	z	Relative Displacement
A	Mass Oscillation Amplitude of Duffings Oscillator		

Chapter 1.

Introduction

With the rapid growth of global population, not only the number of vehicles but also the demand of fuel consumption have experienced a record leap [1]. A high rate of consumption by various fossil-fueled transportation systems results in excessive carbon foot print and emissions. According to United States Environmental Protection Agency (EPA), the primary contributors of greenhouse gas emissions are electricity production and transportation [1]. In the United States, the transportation contribution to greenhouse emission mainly comes from burning petroleum-based fossil fuels (e.g., diesel and gasoline). According to a recent study [2], the US is projected to reduce the greenhouse emission by 16% from 2015 in 2020, which is 1% short of the pre-scheduled target. This goal would not have been met without the moderate adoption rate of electric vehicles (EVs or HEVs) in the US.

According to the United States Department of Energy (DOE), the number of EVs driving on the roads are expected to reach one million by 2015 [3]. With the existing demand in US, the supplies of EVs target several market positions ranging from Fisker Karma, Tesla Model S, X (see Figure 1-1 and Figure 1-2), to Think City EV [3]. Other than minimal carbon emission, electric- motor powered vehicles outperform the running efficiency of a conventional internal combustion engines (ICE), which is roughly 20%. This is due to a maximum of 80% of total energy dissipation takes place in engine, drive train, wheel, and braking. To date, according to EPA [7]-[8], the most fuel efficient ICE powered vehicle is Mitsubishi Mirage CVT, with the combined efficiency of 40 miles per gallon (mpg), which is significantly inferior to that of an EV (e.g. in the same product segment, estimated 110 mpg combined for Nissan Leaf. In part, the superior efficiency of an EV comes from its' ability to regenerate energy of the drive in event of vehicle braking (i.e. recycling kinetic energy into chemical energy for battery storage). Other than regenerative braking, another form of renewable energy recovery for automotive application has been identified. Traditionally, the primary objective of a vehicle suspension system is to isolate road disturbances, such as vehicle acceleration and cornering while providing better ride comfort and handling. Similar to energy loss in vehicle braking, the shock absorber/dash-pot (i.e. suspension damper) dissipates road energy instantaneously for various purposes.

Figure 1-1: Tesla Model S [4].

Figure 1-2: Tesla Model X [5].

To date, the usage of regenerated suspension energy still waits for exploaration. Other than placing as a secondary battery-pack of an EV (to be outlined in Chapter 2, 2.5), in this work, a feasible application is identified, which is providing required energy for supplying the on-board electrical appliances and amenities of a recreational vehicle (RV). In essence, a RV requires both 12 (V) DC and 120 (V) AC for powering on-board appliances (e.g. refrigerators, stove, microwave, laptops, etc). Conventionally, the appliances are powered by either AC chargers at campgrounds or AC generators fuel by unleaded gasoline. According to [9], the maximum rated energy of EG6500 generator is roughly 42 kW-h (120/ 240V, 6500 W for 7 hours under full load). Moreover, since the generator operates synonymous to that of a lawn mower, therefore, the additional drawbacks can be unpleasant gasoline odor and obnoxious mechanical noise. Alternatively, the 12 (V) DC rechargeable batteries can be rejuvenated by RV solar panels [10]. However, a typical single mono-crystalline photovoltaic (PV) solar panel (e.g. Nature Power 50131) is rated at 140 (Watt-hr). Typical energy consumption of electrical appliances onboard a RV is roughly 1.2 to 3.3 (kW-hr), which makes PV incapable of being the main source of energy provider. In addition, so far, PV panels suffer drawbacks, such as low PV panel efficiencies, being prone to ambient temperature, irradiance variations, sizable charging apparatuses (e.g. Maximum Power Point Tacking controller, DC/AC inverter) and attentive maintenance [10]-[11].

In this work, a regenerative suspension system capable of energy storage and control of dynamics are investigated. Compared to regenerative braking, suspension based energy harvesting offers various distinctive characteristics, as follows: (a) Continuous generation of electricity by the suspension generator given the vehicle is in motion (e.g. vehicle accelerating, braking), as opposed to continuous draining of traction batteries onboard a battery-powered EV (b) Through energy harvesting from the applied damping, the sprung mass dynamics is modified, therefore, enabling control of vehicle performance. The available energy of a vehicle suspension, that can be regenerated, is studied based on vehicle weight mass, road roughness, vehicle speed, and number of suspension setups. The primary sources of energy dissipation are identified to be mechanical damping (for “fail- safe” operation), suspension friction, and generator coil losses. The details of power regeneration potential of a full- sized RV will be illustrated in later sections.

1.1. Present State of Vehicular Suspension Control

In the design of vehicular suspensions, the efforts of simultaneously maintaining passenger comfort, chassis body control, and vehicle handling under various driving conditions have long been a challenging topic. Generally speaking, the purpose of a vehicular suspension is to provide vibration isolation. At lower driving speeds, a suspension system with a lower stiffness and damping is desired for passenger comfort. On the contrary, for a vehicle travelling at high speeds, superior dynamic handling with higher stiffness and damping are required for reducing the relative travel between road and tire movements as well as limiting the physical play restrictions of physical shocks and struts.

The control strategies of vehicular suspensions are categorized as active, passive, and semi-active methods. For a passive control strategy, the suspension parameters are fixed. Therefore, as previously mentioned, there should be a compromise between vehicle handling and passenger comfort. With inferior performance, a passive control strategy does not consume electrical power and offers the highest robustness, lowest maintenance cost, and lowest cost to achieve vibration isolation. Active control strategy can offer performance trade-offs contrary to that of passive control. Vehicular suspension with active control is often equipped with variable mechanical actuators (e.g., hydraulic-based), which is instantaneously responsive to road unevenness or road-tire relative displacements. In other words, it offers the best tuning ability. However, the active control method is prone to low robustness, a high maintenance cost, and most expensive cost to provide vibration isolation. Combining the various compromises of the aforementioned control strategies, a semi- active control strategy is introduced in this work. The method primarily focuses on variation of suspension damping coefficients according to various performance objectives. Nowadays, the most popular implementation has been utilizing magneto-rheological (MR) based fluids for their timely response to applied magnetic fields, which leads to variations of fluids viscosity. According to several works dedicated to the area [14]-[19], it is demonstrated that the strategy offers comparable control performance to that of fully active strategy with moderate electrical power consumption, while the robustness and cost are shown to be akin to that of passive control strategy. In subsequent sections, an outline of various existing semi-active and active control technologies is provided.

1.1.1. Delphi Automotive Magne-Ride

The magneto-rheological (MR) based suspension damper developed by Delphi Automotive PLC has been among the most popular adopted actuators which utilizes a semi-active control system. As previously mentioned, the flow characteristics of MR fluids can be varied in a controlled manner by the applied magnetic field.

As illustrated in [6], a Mage-Ride damper equipped by Audi TT, the internal MR fluids passages are surrounded by electromagnets. Generally speaking, when the electromagnet is actuated, the iron particles align to increase fluid viscosity, therefore making it more resistive to flow. By adjusting the DC current flow through the coil, the thickness or viscosity of the fluid can be instantaneously adjusted (plastic viscosity) in milliseconds. As a result, with a variable resistance to the fluid flow the suspension damping coefficient can be tighter or softer. Currently, the technology is found in various types of up-scale vehicles, such as Chevrolet Corvette, Acura MDX, Cadillac CTS-V, Audi R8, and Ferrari 599. Various control algorithms, such as sky-hook, ground-hook, limited relative displacement (LRD), and Rakheja Sankar (RS) have been proposed for controlling the presence/ absence of suspension damping [13]-[19].

1.1.2. Daimler- Benz AG Magic Body Control

The detailed operating principle of the Magic Body Control (MBC) has not been made public. In general, the MBC with PRE-SCAN suspension (i.e. ADVANCED AGILITY package) developed by Daimler-Benz AG can be categorized as a full-active control strategy.To date, the technology is utilized on Mercedez Benz research vehicle F700 and S350.

According to Figure 1-3 and [12], the on-board sensors (i.e., binocular-vision cameras) pre-scan the road profiles ahead. Knowing the road roughness in-advance allows computing the appropriate actuating force, according to an adopted control law. The force is generated by the active hydraulic actuator for compensating the road unevenness. Subsequently, the suspension lifts the vehicle tire to glide along the road surface while transmitting the minimum vibration to the vehicle body. This approach actively softens the suspension stiffness while driving through bumps/ potholes.

Mercedes-Benz F 700 with PRE-SCAN® suspension

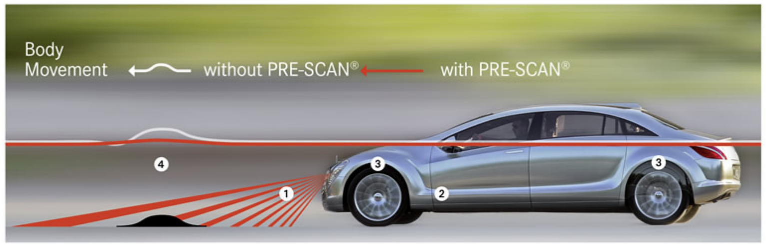

① Sensors inside the head lamps send out pulsed laser beams (approx. 70 measuring points per ray) in the infrared range to scan the road profile in front of the vehicle.

② The unevenness of the road surface is computed from the continously received data and is used for an appropriate control strategy for the ABC (Active Body Control)

③ The hydraulic actuators inside the ABC (Active Body Control) spring struts compensate the unevenness of the road at each wheel independently.

④ The wheels essentially follow the contour of the surface, but the vehicle body glides virtually unaffected over the road.

Figure 1-3: ADVANCED AGILITY with PRE- SCAN suspension [12].

1.2. Electromagnetic Vehicular Suspensions

In the aforementioned control strategies, the approaches are either dissipation of mechanical energy (i.e., passive control), or consumption electrical energy for compensating road roughness (i.e., active or semi-active control). In light of recycling the dissipated or consumed energy (i.e., energy harvesting), various electromagnetic vehicular suspensions have been proposed by numerous research groups [20]-[41]. Energy harvesting in a vibrational environment has been a popular topic of research in renewable energy. Harvesting the energies that could have been dissipated opens up a wide range of applications. Essentially, the technique converts kinetic motion of sprung mass into electrical power and reserves it in energy storing device for further uses, such as supplying power for wireless sensor networks, active control, and self-powered sensors.

1.2.1. Linear permanent magnets (PM) Actuator

Due to the linear motion of base excitation, the implementations of tubular PM (TL- PM) actuators, to act as a variable regenerative damper, have been extremely popular [20]-[32]. While many works have devoted to designing a linear PM based generator with higher energy density and linear response for large- scale energy harvesting applications. The linear generator fabricated by [26]-[27], [31], [32] are specifically targeting automotive applications. According to

[26], the linear PM generator is able to provide damping coefficient of 1138 N·s/m while harvesting maximum 35.5 W power while suspension is traveling at 0.25m/s in a mass- spring base excitation setup.

1.2.2. Rotational DC Machine

According to [34], a cylindrical DC motor can regenerate vibration energy only at high speed motion. In low speed operations, the damper has undesired nonlinear characteristics with dead zone and cannot regenerate energy. In addition, with lower cost and off- the- shelf availability, a rotational DC motor, acting as a regenerative damper in an electro- magnetic suspension system has been presented in [35]-[39]. Since the rotational DC machine regenerates electricity by the shaft's rotational displacement, a mechanism that translates linear to rotational motions is required. As mentioned in [37]-[39], the rack/pinion and ball- screw mechanisms have been fabricated for the motion transformation. As reported by [38], a peak power of 68 (Watts) and average power of 19 (Watts) can be regenerated from the shock absorber prototype when the retrofitted vehicle is driven at 48 km/h (30 mph) on a smooth road.

1.3. Root Mean Square Optimization for Improved Vehicle Performance

Other than vehicular suspension control and design of regenerative suspension systems the methods of optimizing suspension parameters have been proposed extensively [43]-[46]. According to [43] and [46] , the values of suspension stiffness and damping can be optimized by minimizing cost functions, which is the Root Mean Square (RMS) of sprung mass acceleration a and relative displacements λ over an extended range (i.e. 0 to 40π) of excitation frequencies ω can be obtained by the following

$$R = \sqrt{(40\pi)^{-1} \int_{0}^{40\pi} a^2 d\omega} \tag{1-1}$$

$$\eta = \sqrt{(40\pi)^{-1} \int_{0}^{40\pi} \lambda^2 d\omega}\,. \tag{1-2}$$

According to the optimization chart the value of suspension parameters (e.g. damping ratios ζ, natural frequencies ω_n) can be selected for complying with suspension relative displacement or sprung mass acceleration restrictions. As indicated in [43], the tradeoffs between dynamical behavior of suspension relative displacement and sprung mass acceleration are shown through their RMS values. The minimum RMS accelerations with respect to various w_n for a specific value of RMS relative displacement, indicated by line of minima, are shown in Figure 1-4 (a).

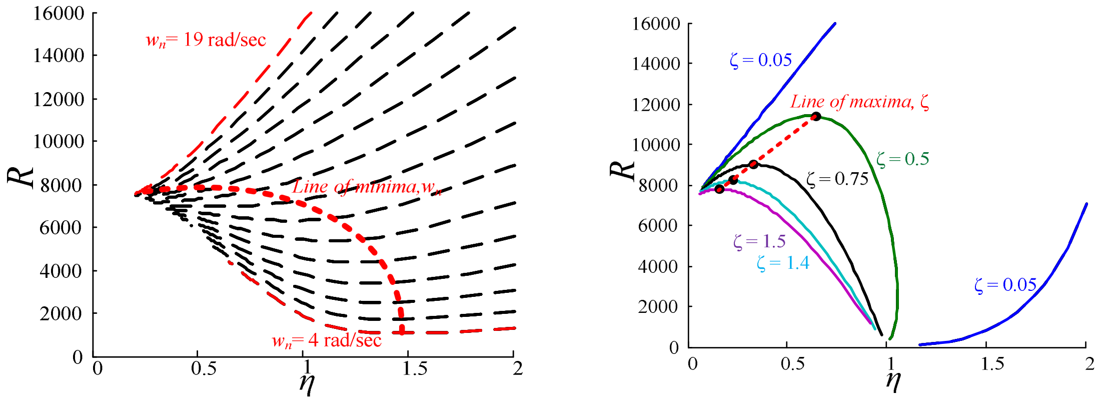

(a)

(b)

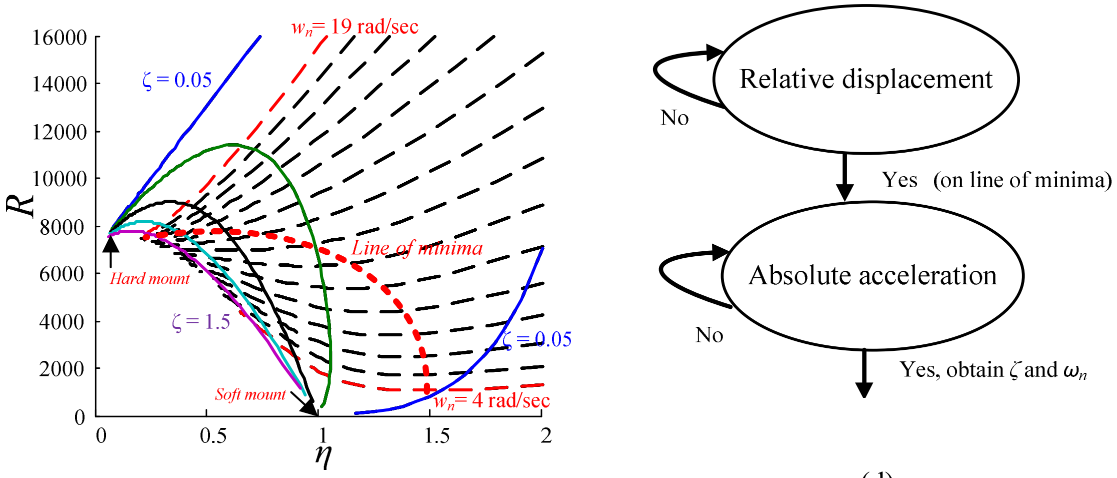

(c)

(d)

Figure 1-4: (a) Line of minima maxima for lowest RMS of absolute acceleration and (b) line of maxima for highest RMS of absolute acceleration for a specified suspension relative displacement. (c) Design chart and (d) state diagram for choosing optimal ω_n and ζ are delineated by RMS absolute acceleration line of minima with respect to RMS relative displacements.

The maximum RMS accelerations with respect to various ζ for a specific value of RMS relative displacement, indicated by line of maxima, are shown in Figure 1-4 (b). As depicted in Figure 1-4 (c), the optimal natural frequency and damping ratio values of a one degree-of- freedom suspension mount are delineated by line of minima of RMS absolute acceleration with respect to various RMS relative displacements. It is shown that increasing the natural frequency should be followed by increasing the damping ratio, and vice versa. Referring to the optimized chart and its corresponding state diagram in Figure 1-4 (d) one can select a desired value for relative displacement as the traveling space limitation (or the absolute acceleration). Subsequently, the associated value of damping ratio ζ and natural frequencies ω_n at the intersection of the associated vertical (horizontal) line on the optimal curve is obtained.

1.4. Chapter Summary

In this chapter, the status of modern suspension systems was presented. Considering cost, feasibility, and control performance, it is realized that magnetorheological-based semi-active systems have been the most widely adopted suspension mechanismscurrently adopted by most car manufactures. In addition, the anatomy of a fully active suspension control method was discussed. The technology simultaneously accomplishes superior vehicle handling and passenger comfort at the expense of extra energy requirements. Furthermore, to accomplish suspension control and energy harvesting, various electromagnetic suspension topologies, proposed by different research groups, have been discussed. The topologies are primarily categorized by utilizing linear or rotational DC machines. In the next chapter, the regenerative suspension topology proposed by the Intellegent Vehicles Technology Laboratory will be discussed in great detail.

Chapter 2.

Energy Harvesting of Regenerative Vehicular Suspension and Road Excitation Modeling

In this chapter, the modelling of standardized ISO road profile and a regenerative suspension system are studied. The power regeneration mechanism is presented for a DC machine under road excitation. By utilizing the one and two degrees-of-freedom (DOF) dynamic systems we obtain the response of a sprung mass under base excitations. Finally, a switched-mode converter is studied for the purpose of road energy harvesting. The performance is demonstrated in terms of power regeneration potentional, along with experimental results on a small-scale prototype.

2.1. Regenerative Mechatronic System

Various electromagnetic suspension setups have been presented in [37]-[39], which consist of a typical base-excited suspension systems comprised of a mechanical spring, sprung mass, and damper (for fail-safe operation). In addition, a rotational DC motor coupled to a linear-rotational motion transformation mechanism (e.g. a ball-screw device) is required for power regeneration.

The dynamics of a vehicle suspension system has been extensively modeled by two degree-of-freedom (2-DOF) mass-spring-damper dynamic systems [37]-[39], [47]-[48]. Referring to the detailed view of a vehicular suspension in Figure 2-1, the quarter of a vehicle (i.e. sprung mass) experiences road excitation through isolation of tire, spring, and damper. The mass of sprung mass and vehicle tire are indicated by m and m_r, respectively. The tire stiffness and suspension stiffness are represented by k_t and k, respectively. The damping coefficient is specified by *c*. According to Newton's second law of motion the dynamic equation of the 2- DOF base excitation model in terms of both *m* and m_r can be written as the following

$$m\ddot{x}+c\left(\dot{x}-\dot{x}_t\right)+k\left(x-x_t\right)=0 \tag{2-1}$$

$$m_t\ddot{x}_t+c\left(\dot{x}_t-\dot{x}\right)+k\left(x_t-x\right)+k_t\left(x_t-y\right)=0 \tag{2-2}$$

where *x* and x_t are the displacement response of sprung mass, vehicle tire, *y* is the base displacement response. The discrete spring stiffness and tire stiffness are indicated by *k* and k_t, respectively. The damping is represented by *c*. Defining relative displacement between sprung mass and base (i.e. $z= x\text{-}x_t$) we can rewrite the sprung mass dynamic equations into the following

$$m\ddot{z}+c\dot{z}+kz=-m\ddot{x}_t\,. \tag{2-3}$$

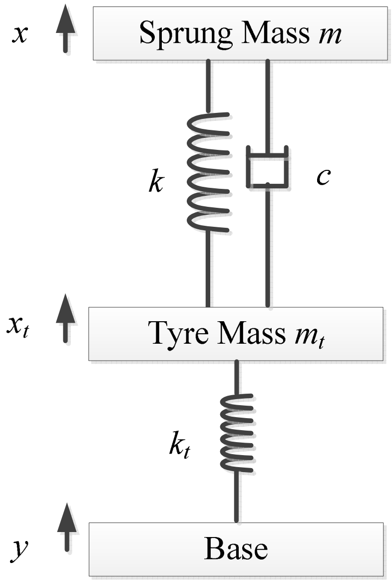

Figure 2-1: A two degree-of-freedom base excitation model.

The transfer functions between sprung mass-base $X\left(j\omega\right)Y^{-1}\left(j\omega\right)$ and tire mass-base $X_t\left(j\omega\right)Y^{-1}\left(j\omega\right)$ dynamics are derived. Applying Laplace transformation (i.e. s=jω) we can solve for (2-1) to (2-2) as the following, respectively

$$\frac{X(j\omega)}{Y(j\omega)}=\frac{sck^{-1}+1}{s^4 m m_t k^{-1} k_t^{-1}+s^3\left(c\left(m+m_t\right)k^{-1}k_t^{-1}\right)+s^2\left(k_t^{-1}\left(m+m_t\right)+k^{-1}m\right)+sck^{-1}+1} \qquad (2\text{-}4)$$

$$\frac{X_t(j\omega)}{Y(j\omega)}=\frac{s^2 mk^{-1}+sck^{-1}+1}{s^4 m m_t k^{-1} k_t^{-1}+s^3\left(c\left(m+m_t\right)k^{-1}k_t^{-1}\right)+s^2\left(k_t^{-1}\left(m+m_t\right)+k^{-1}m\right)+sck^{-1}+1} \qquad (2\text{-}5)$$

To indicate the vehicle tire dynamics x_t, the nominal values of m= 500 kg, m_t= 50 kg, c= 5 kNsec/m, k= 23245 N/m, and k_t= 2 MN/m are substituted into (2-5). The tire stiffness is assumed roughly an order of magnitude higher than that of the physical spring. In this case, the transfer function is obtained as the following

$$\frac{X_t(j\omega)}{Y(j\omega)}=\frac{4000\left(s^2+10s+46.5\right)}{(\mathrm{s}^2+10.02\mathrm{s}+53.81)\,(\mathrm{s}^2+99.98\mathrm{s}+3456)}. \qquad (2\text{-}6)$$

Due to the close vicinities of the complex poles and zeros the dynamics of the 4-th order low-pass transfer function is similar to that of a 2nd order, as indicated by the bode plot in Figure 2-2 (a)- (b). By exciting the suspension with y= 0.01sin (2πt) and y= 0.01sin (20πt), as depicted in Figure 2-2 (c), the amplitude/ phase of x_t are attenuated by the tire mass- base transfer function in (2-5).

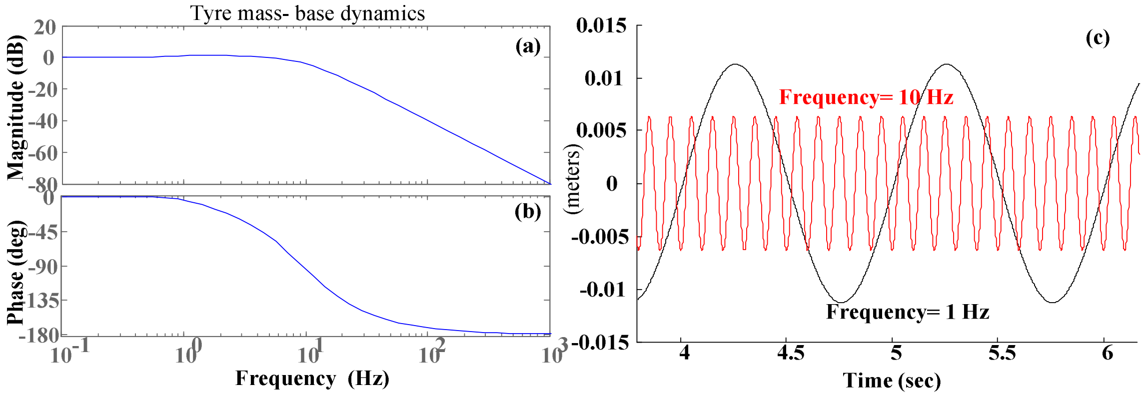

Figure 2-2: (a) Amplitude and (b) phase of tire mass- base dynamics and the (c) corresponding instantaneous response with excitation frequency of 1 and 10 Hz.

Similarly, the relative displacements between sprung mass and base movements as well as sprung mass absolute acceleration are also derived as

$$\frac{\ddot{X}(j\omega)}{Y(j\omega)}=\frac{s^3ck^{-1}+s^2}{s^4mm_tk^{-1}k_t^{-1}+s^3\left(c\left(m+m_t\right)k^{-1}k_t^{-1}\right)+s^2\left(k_t^{-1}\left(m+m_t\right)+k^{-1}m\right)+sck^{-1}+1} \tag{2-7}$$

$$\frac{Z(j\omega)}{Y(j\omega)}=\frac{-s^4mm_tk^{-1}k_t^{-1}-s^3\left(c\left(m+m_t\right)k^{-1}k_t^{-1}\right)-s^2\left(k_t^{-1}\left(m+m_t\right)+k^{-1}m\right)}{s^4mm_tk^{-1}k_t^{-1}+s^3\left(c\left(m+m_t\right)k^{-1}k_t^{-1}\right)+s^2\left(k_t^{-1}\left(m+m_t\right)+k^{-1}m\right)+sck^{-1}+1}. \tag{2-8}$$

Assuming the vehicle tire is massless (i.e. m_t= 0 kg) with minimal stiffness (i.e. k_t= 0 N/m), the quarter-car model can be represented by a linear single degree of freedom (SDOF) mass-spring-damper as shown in Figure 2-4. This can be shown by deriving the relative displacement between sprung mass and vehicle tire (i.e. $\Delta X(j\omega)=X(j\omega)-X_t(j\omega)$) as the following

$$\frac{\Delta X(j\omega)}{Y(j\omega)}=\frac{-s^2mk^{-1}}{s^4mm_tk^{-1}k_t^{-1}+s^3\left(c\left(m+m_t\right)k^{-1}k_t^{-1}\right)+s^2\left(k_t^{-1}\left(m+m_t\right)+k^{-1}m\right)+sck^{-1}+1} \tag{2-9}$$

Combining the dynamics of the vehicle tire and road excitation the 2- DOF base excitation model can be simplified to a single degree of freedom (SDOF). Traditionally, the primary objective of a vehicle suspension system is to isolate road disturbance, such as acceleration and cornering while providing better ride comfort and handling. As depicted in Figure 2-3 and Figure 2-4, a single degree of freedom (SDOF) passive suspension system under road vibration, the sprung mass (*m*) is driven by the base movement (i.e. combined dynamics of road profile/ vehicle tire) through the discrete spring (*k*) and damper (*c*). As indicated in [37], if the vehicle seat dynamics are not considered, the passenger comfort is defined by the vehicle sprung mass absolute acceleration. The vehicle handling is indicated by the contact force between tire displacement and road excitation. In radical situations, the tire can lose contact with road, therefore, to indicate vehicle handling, the relative displacement between tire and road is utilized (i.e. x_t-y). Recalling 1.3, by assuming m_t= 0 (kg) the performing index for physical restriction of suspension travel and vehicle handling can be combined.

Figure 2-3: Rendition of SDOF Mercedes- Benz S class front suspension under road- excitation [12].

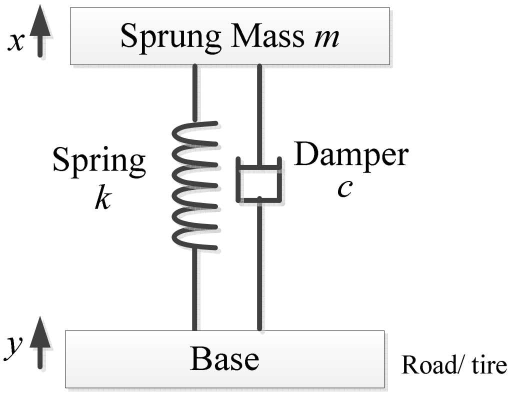

Figure 2-4: SDOF base excitation model.

2.1.1. Electro- Mechanical Analogy

To demonstrate the equivalent dynamics provided by the power electronics converter (in the electrical domain), a mechanical-electrical analogy is adopted. In this work, mechanical force is considered as the dual of electrical current, whereas speed (velocity) is the dual of voltage. Referring to a single harmonic base excitation mass-spring-damper model shown in Figure 2-4, one can apply the mechanical-electrical analogy and converter it into a current source driven parallel *RLC* resonance circuit as shown in Figure 2-5 (b).

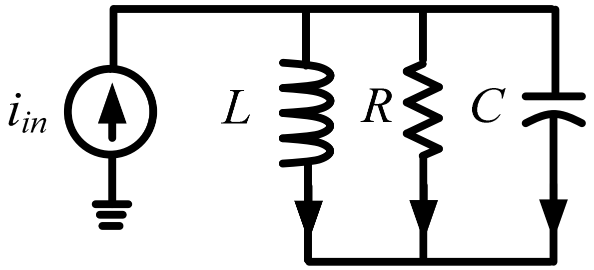

Figure 2-5: Equivalent *RLC* circuit of a base- excited mass- spring damper model.

The dynamic equation of a parallel *RLC* circuit in Figure 2-5 is obtained by noting that the total current i_{in} is the sum of currents flowing through inductor (*L*), resistor (*R*), and capacitor (*C*) as follows

$$C\frac{dV(t)}{dt}+L^{-1}\int V(t)dt+R^{-1}V(t)=i_{in}(t) \tag{2-10}$$

Similarly, the road force f_{road} of the base excitation model is the sum of forces acting on spring (*k*), sprung mass (*m*), and damper (*c*). Thus, the base excitation dynamic equation is given by

$$\begin{aligned} m\frac{d^2z(t)}{dt^2}+kz(t)+c\frac{dz(t)}{dt} &= f_{road}(t) \\ &= -A\omega^2\sin\omega t \end{aligned} \tag{2-11}$$

where $z=x-y$ is the sprung mass relative displacement, *A* is the excitation amplitude, and *ω* is the angular frequency. Comparing (2-10) to (2-11) it follows that the electrical voltage, inductance, resistance, and capacitance are essentially equivalent to relative velocity, inverse stiffness, inverse damping, and sprung mass of the base excitation model as tabulated in Table 2-1. Therefore, both equations essentially demonstrate the same response if the current source equals to road force, i_{in}(t) = $-Aw^2\sin\omega t$.

Table 2-1: Adopted electro- mechanical analogy

Mechanical	Electrical
Force F	Current
Relative velocity $\dot{z}$	Voltage
Relative displacement z	Flux
Stiffness k	Inverse inductance: L^{-1}
Damping c	Inverse resistance: R^{-1}
Mass m	Capacitance: C

To analyze the response of a single degree of freedom (SDOF) base excitation model, it is prevalent to consider the case of constant amplitude harmonic excitation (i.e. $z(s)=|z|e^{j\omega t}$ and $y(s)=|y|e^{j\omega t}$) [47]- [48]. Applying Laplace transformation to (2-3) with $x=x_t$ we can solve for sprung mass absolute acceleration $\ddot{x}(\omega)\ddot{y}^{-1}(\omega)$ in Laplace domain as the following

$$H_{acc}(\omega)=\frac{\omega^2\sqrt{\left(k^2+(c\omega)^2\right)}}{\sqrt{\left(\left(k-m\omega^2\right)^2+(c\omega)^2\right)}}\ . \tag{2-12}$$

The relative acceleration $\ddot{x}(\omega)\ddot{y}^{-1}(\omega)$ and displacement $z(\omega)\ddot{y}^{-1}(\omega)$ transfer functions are also derived as follows

$$H_{rel\_disp}(\omega)=\frac{m\omega^2}{\sqrt{\left(\left(k-m\omega^2\right)^2+(c\omega)^2\right)}} \tag{2-13}$$

$$H_{rel\_acc}(\omega)=\frac{m}{\sqrt{\left(\left(k-m\omega^2\right)^2+(c\omega)^2\right)}} \tag{2-14}$$

Next, let us on-dimensionalize the transfer functions by defining $\omega_n = \left(km^{-1}\right)^{0.5}$, $\xi = c\left(2m\omega_n\right)^{-1}$ and $r=\omega\omega_n^{-1}$. Hence, the transfer functions of sprung mass absolute acceleration, relative acceleration and displacement are as follows

$$H_{acc}\left(r\right) = \omega_n^{-2}\sqrt{\left(1+4\xi^2r^2\right)\left(\left(1-r^2\right)^2+4\xi^2r^2\right)^{-1}} \tag{2-15}$$

$$H_{rel\_disp}\left(r\right) = \frac{r^2}{\sqrt{\left(\left(1-r^2\right)^2+4\xi^2r^2\right)}} \tag{2-16}$$

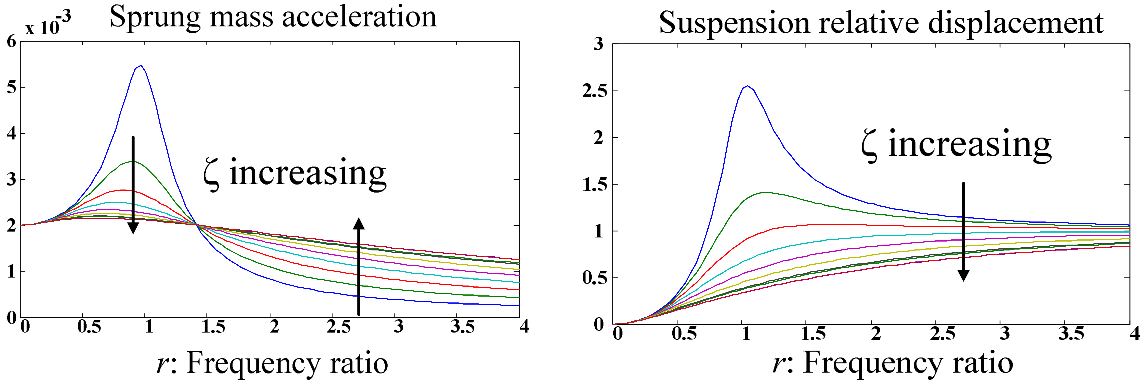

(a) (b)

Figure 2-6: Non-dimensionalized frequency response of (a) sprung mass absolute acceleration (b) suspension relative displacement.

In order to observe suspension dynamics under different excitation frequencies, we can generate frequency response functions (FRF) for absolute acceleration and relative displacement, as shown in Figure 2-6, with transfer functions in non-dimensionalized form. Again, assuming harmonic excitations, the ideal speed of a vehicle can be written as

$$v = \omega l\left(2\pi\right)^{-1} \tag{2-17}$$

where ω and l are the excitation angular frequency and distance of travel (road wavelength). As indicated in (2-12), a larger value of r represents faster vehicle speed. As shown in Figure 2-6 (a), the mass absolute acceleration frequency response indicates that in the post-resonance frequency region where frequency ratio $r > \sqrt{2}$ the absolute acceleration is inverse proportional to the damping ratio ζ. In contrast, in the region where frequency ratio $r < \sqrt{2}$ the absolute acceleration is proportional to damping ratio ζ. As shown in Figure 2-6 (b), the relative displacement response indicates that the response is inversely proportional to ζ for the entire range of frequencies and the resonance frequency is inversely proportional to ζ. The higher value of ζ indicates lower levels of relative displacements. Therefore, it is realized that under constant amplitude harmonic excitation, the passive suspension with higher value of damping results in better vehicle handling (i.e. lower relative displacement), while a lower value of damping will contribute to more comfortable ride in the region where frequency ratio $r > \sqrt{2}$ due to lower absolute accelerations.

2.1.2. Analytical Analysis of Forced Oscillator with Nonlinear Stiffness

In this section, to illustrate the nonlinear oscillation phenomenon of cubic stiffness force, so-called Duffing's equation is solved using a perturbation method (e.g. methods of multiple-scales, averaging, and Lindstedt Poincare method). To analytically solve the Duffing's equation we consider a general forced oscillation of a sprung-mass attached to a nonlinear spring under the influence of slight viscous damping so that the equation of motion has the following form

$$\ddot{x} + \omega_o^2 x + 2\varepsilon\mu\dot{x} + \varepsilon\alpha x^3 = E(t) \tag{2-18}$$

where $E(t) = K\cos\Omega t = \varepsilon k \cos\Omega t$ is the external excitation, ε, μ, and α indicate the level of nonlinearity, damping and spring constant in the system, respectively. To start analyzing the system under primary resonance, a detuning parameter σ should be introduced, which quantitatively describes the nearness of $\Omega = \omega_o + \varepsilon\sigma$ to ω_o. In a linear undamped system, the systems response will present unbounded oscillation when being excited at the natural frequency (i.e. $\sigma = 0$) regardless of how small the excitation amplitude, K. However, in actual events the amplitude of the system response, even when excited at ω_o, will be limited by the system's implicit nonlinearities and damping. Therefore, to offer a uniformly approximation to the system, one has to make excitation amplitude, *K*, a function of system nonlinearity, ε , as $K = \varepsilon k$. Note that this arrangement is still consistent with the theories of linear lightly damped system, which indicates that under small excitation the system's response becomes unbounded as time approaches infinity [49].

Here, we assumed the sprung mass response, in (2-18), the form of following

$$x = x_0(T_0) + \varepsilon x_1(T_1) + \varepsilon^2 x_2(T_2) \tag{2-19}$$

where $T_o = t$ (i.e. normal scale) and $T_1 = \varepsilon t$ (i.e. slow scale, T_2 runs slower than T_1, which is omitted in this derivation). Substitute (2-19) into (2-18) while separating terms with ε^0 and ε^1 as follows:

$$\varepsilon^0 : D_0^2 x_0 + x_0 = 0 \tag{2-20}$$

$$\varepsilon^1 : D_0^2 x_1 + \omega_0^2 x_1 = -2D_0 D_1 x_0 - 2\mu D_0 x_0 - \alpha x_0^3 + k\cos(\omega_0 T_0 + \sigma T_1) \tag{2-21}$$

where 1st and 2nd order derivate operators are $\frac{d}{dt} = \frac{\partial}{\partial T_0} + \varepsilon \frac{\partial}{\partial T_1} + \ldots = D_0 + \varepsilon D_1 + \ldots$ and $\frac{d^2}{dt^2} = D_0^2 + 2\varepsilon D_0 D_1 + \ldots$, respectively. Also, ε, μ, and α indicate the level of nonlinearity, damping and spring constant in the system, respectively. Applying the method of multiple scales the solutions to (2-19) is expected to be in the form of $x_0 = A(T_1)e^{j\omega_0 T_0} + \overline{A}(T_1)e^{-j\omega_0 T_0}$, where $A(T_1)$ and $\overline{A}(T_1)$ are complex conjugates. Substituting it into (2-21) will result the following,

$$\begin{aligned}\varepsilon^1 : D_0^2 x_1 + \omega_0^2 x_1 = &-\left[2j\omega_o(A + \mu A') + 3\alpha A^2 \overline{A}\right]\exp(j\omega_o T_0) \\ &- \alpha A^3 \exp(j3\omega_o T_0) + \frac{1}{2}k\exp(j\omega_o T_0 + j\sigma T_1) + \ldots\end{aligned} \tag{2-22}$$

To eliminate the secular term, we set the coefficients of $\exp(j\omega_o T_0)$ to 0, which is the following,

$$-\left[2j\omega_o(A+\mu A')+3\alpha A^2\bar{A}\right]+\frac{1}{2}k\exp(j\sigma T_1)=0 \tag{2-23}$$

Assuming the solution of (2-23) in polar form with $A = 0.5ae^{j\beta}$ and grouping the real and imaginary part one will arrive in a pair of first order ordinary differential equation (ODE),

$$a' + \mu a - \frac{1}{2}\frac{k}{\omega_o}\sin(\sigma T_1 - \beta) = 0 \tag{2-24}$$

$$a\beta' - \frac{3}{8}\frac{\alpha}{\omega_o}a^3 + \frac{1}{2}\frac{k}{\omega_o}\cos(\sigma T_1 - \beta) = 0 \tag{2-25}$$

Note when the motion of the system is under steady state the time derivative of *a* and *β* (i.e. a' and β') are both zero, meaning both amplitude and phase are not changing with respect to time as indicated by in Figure 2-7.

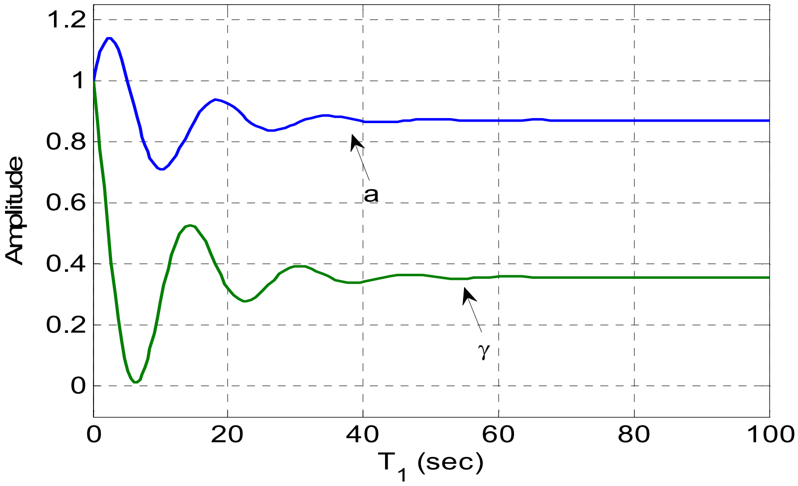

Figure 2-7: Variation of *a* and *γ* (a_o =1, γ_o=1) with T_1 for σ=0.05, f=0.5, μ=0.1

Therefore, under steady- state the following occurs

$$\mu a = \frac{1}{2}\frac{k}{\omega_o}\sin(\sigma T_1 - \beta) \tag{2-26}$$

$$\frac{3}{8}\frac{\alpha}{\omega_o}a^3 = -\frac{1}{2}\frac{k}{\omega_o}\cos(\sigma T_1 - \beta) \tag{2-27}$$

Transforming from non-autonomous to autonomous system one can assume $\gamma = \sigma T_1 - \beta$, thus, $\gamma' = \sigma_1 - \beta'$, so (2-26)-(2-27) will lead to (2-28)-(2-29), respectively, as shown in the following

$$a' = -\mu a + \frac{1}{2}\frac{k}{\omega_o}\sin(\gamma) \tag{2-28}$$

$$a\gamma' = a\sigma - \frac{3}{8}\frac{\alpha}{\omega_o}a^3 + \frac{1}{2}\frac{k}{\omega_o}\cos(\gamma) \tag{2-29}$$

The stability of the steady state motion can be analyzed by obtaining the Jacobian matrix (i.e., derivative with respect to *a* and *γ*) of (2-28)-(2-29), which results in

$$\det\begin{pmatrix} \frac{da'}{da} - \lambda = -\mu - \lambda & \frac{da'}{d\gamma} = -a(\sigma - \frac{3\alpha a^2}{8\omega_o}) \\ \frac{d\gamma'}{da} = \frac{1}{a}(\sigma - \frac{9\alpha a^2}{8\omega_o}) & \frac{d\gamma'}{d\gamma} - \lambda = -\mu - \lambda \end{pmatrix} = 0 \tag{2-30}$$

Taking the determinant of the matrix, we obtain $\lambda^2 + 2\mu\lambda + \left[\mu^2 + (\sigma - \frac{3\alpha a^2}{8\omega_o})(\sigma - \frac{9\alpha a^2}{8\omega_o})\right] = 0$, hence the steady state motion is stable when $\mu^2 + (\sigma - \frac{3\alpha a^2}{8\omega_o})(\sigma - \frac{9\alpha a^2}{8\omega_o}) > 0$. Squaring and adding (2-28) and (2-29) one will arrive in the following assuming under steady state (i.e. $a', \gamma' = 0$),

$$\left(\mu^2 + \left(\sigma - \frac{3}{8}\frac{\alpha}{\omega_o}a^2\right)^2\right)a^2 = \frac{k^2}{4\omega_o^2} \tag{2-31}$$

Rearranging above one will be able to obtain the so-called “frequency response equation” as seen in the following

$$\sigma = \frac{3}{8}\frac{\alpha}{\omega_o}a^2 \pm \left(\frac{k^2}{4\omega_o^2 a^2} - \mu^2\right)^{1/2} = A \pm \left(B\right)^{1/2} \tag{2-32}$$

From (2-32), the plots of response amplitude a vs. frequency excitation σ or response amplitude a versus amplitude of excitation k can be generated. It is seen from (2-32) that σ has two solutions for every value of a unless $B = \left(4\omega_o^2 a^2\right)^{-1} k^2 - \mu^2 = 0$, which is exactly the condition for peak amplitude to occur, $a_{peak} = \left(2\omega_o \mu\right)^{-1} k^2$. Moreover, one can construct the so-called backbone curve when B= 0, which indicates the condition of $\sigma_{backbone} = \frac{3}{8}\frac{\alpha}{\omega_o}a^2$.

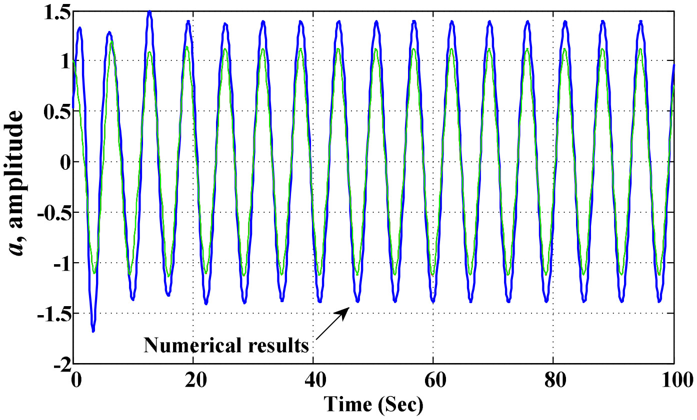

Figure 2-8: Analytical and numerical simulation of systems response (blue: numerical results)

Since we have assumed the polar form of $A = 0.5ae^{j\beta}$, thus, we know that x_o will be in the form of

$$x_0 = A(T_1)e^{j\omega_0 T_0} + \overline{A}(T_1)e^{-j\omega_0 T_0} = \frac{1}{2}ae^{j\beta}e^{j\omega_0 T_0} + \frac{1}{2}ae^{-j\beta}e^{-j\omega_0 T_0} = a\cos(\omega_0 T_0 + \beta) \tag{2-33}$$

therefore, $x = x_0(T_0) + \varepsilon x_1(T_1) + \varepsilon^2 x_2(T_2) = a\cos(\omega_0 T_0 + \beta) + \varepsilon x_1(T_1) + \varepsilon^2 x_2(T_2)$ where a, β are constants. Moreover, since $\gamma = \sigma T_1 - \beta$, we can further express the systems response to be $x = a\cos(\omega_0 T_0 + \sigma T_1 - \gamma) + ... = a\cos(\omega_0 t + \sigma\varepsilon t - \gamma) + ... = a\cos(\Omega t - \gamma) + ...$. Therefore, one can conclude from the expression of systems response that under steady-state the response is tuned to the frequency of excitation, Ω, with phase shifts γ. Lastly, to verify the correctness the systems response in Figure 2-8, the figure is generated both analytically and numerically (e.g. ODE 45). It is seen that there are consistent deviations in waveform amplitudes under steady-state with negligible phase differences. This verifies that the first order expansion of Duffing’s equation using the method of multiple scales is able to predict the systems response with some error margin.

2.1.3. Electric Generator with Shunt Resistor

Before modeling the regenerative suspension system it is imperative to observe power generation by a DC machine. Since a DC motor is essentially a mechatronic device, we shall analyze it in both mechanical and electrical domain. Referring to Figure 2-9, a load resistor is connected in parallel to the DC generator. The term $T_{suspension}$ is the input torque applied at the motor shaft and $T_e= k_t i_{in}$ is the developed torque due to i_{in} by multiplying the motor torque constant k_t. In short, when attaching a DC machine to a linearly excited MSD system the following occurs for power regeneration. As the motor shaft spins purse sinusoidally, it results to a sinusoidal EMF, which can be seen as an angular velocity controlled voltage source. According to value of R_{load}, in Figure 2-9, it leads to different values of i_{in}, and thus the electrically generated torque T_e. Subsquently, the electrically generated T_e can be fed back to the MSD system to vary the desired dynamics. This process integrates the dual purposes of R_{load}, which achieves both electrical energy harvesting and mechanical dynamic control. Traditionally, mechanical dashpots, tunable MR damper, or active-control type hydraulic actuators are not able to achieve both purposes simultaneously.

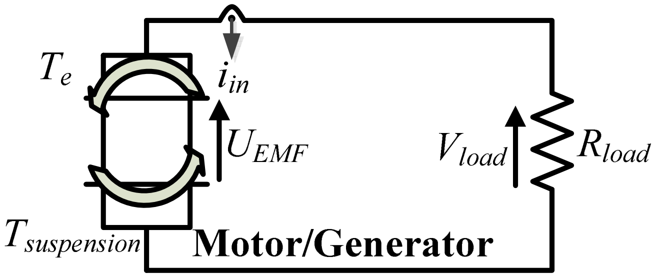

Figure 2-9: Electric generator in parallel connection to resistive load.

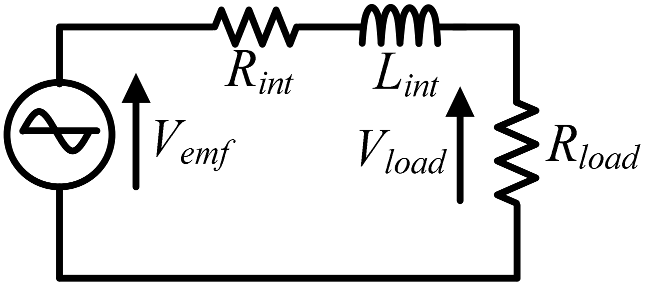

Figure 2-10: Equivalent circuit of electric generator in parallel connection to resistive load.

Applying Newton's second law of motion to the rotational shaft of DC machine will result in the following

$$T_{suspension} - T_e = J\frac{d^2\theta}{dt^2} \tag{2-34}$$

where J is the rotor inertia, θ is the rotational displacement. By replacing the DC generator with an equivalent circuit as shown in Figure 2-10 and applying Kirchhoff's voltage laws (KVL) one will have the following

$$V_{emf} = i_{in}\left(R_{load} + R_{\text{int}}\right) + L_{\text{int}}\frac{di_{in}}{dt} \tag{2-35}$$

where R_{int} and L_{int} represent the dynamics of DC motor internal impedance. The back EMF is developed by angular velocity $\dot{\theta}$ multiplying the motor velocity constant k_v as follows

$$V_{emf} = k_v\dot{\theta}\,. \tag{2-36}$$

Substituting (2-34) into (2-35), the dynamic equations of the electric generator with a resistive load can be written as the following

$$k_v\frac{d\theta}{dt} - \frac{L_{\text{int}}}{k_t}\frac{d}{dt}\left(T_{suspension} - J\frac{d^2\theta}{dt^2}\right) = \frac{\left(R_{load} + R_{\text{int}}\right)}{k_t}\left(T_{suspension} - J\frac{d^2\theta}{dt^2}\right) \tag{2-37}$$

Assuming zero initial conditions and applying Laplace transformation, we can write

$$\begin{aligned} T_{suspension} &= \left(\frac{k_t k_v s}{\left(R_{load} + R_{\text{int}}\right) + sL_{\text{int}}} + Js^2 \right)\theta \\ &= Js^2\theta + cs\theta + k\theta \end{aligned} \qquad (2\text{-}38)$$

Therefore, the equivalent rotational damping (N-sec/m) and stiffness (N/m) for an electric generator connected to a load resistor are given by ($s=j\omega$)

$$c = \frac{k_v k_t \left(R_{load} + R_{\text{int}}\right)}{\left(R_{load} + R_{\text{int}}\right)^2 + w^2 L_{\text{int}}^2} \qquad (2\text{-}39)$$

$$k = \frac{k_v k_t w^2 L_{\text{int}}}{\left(R_{load} + R_{\text{int}}\right)^2 + w^2 L_{\text{int}}^2}. \qquad (2\text{-}40)$$

It is assumed internal impedance is resistive (i.e. $\omega L_{\text{int}} << R_{\text{int}}$) due to low excitation frequency, contributed by road irregularities. With the assumption, the equivalent rotational stiffness can be approximated to zero and the rotational damping can be simplified to $k \approx 0$ and $c = k_v k_t \left(R_{load} + R_{\text{int}}\right)^{-1}$.

2.2. Regenerative Suspension Prototype Modeling

The proposed quarter-car (i.e. Q-car) regenerative suspension prototype is shown in Figure 2-11. It is modeled as a 1-DOF dynamic system attached to a ball- screw/ DC motor for energy regeneration. The operation principle of the regenerative suspension is as follows. As the base is excited, the ball nut experiences linear force with respect to the suspension relative displacement and velocity. Converting the direction of motion, the screw shaft (coupled to the DC machine) experiences a bi-directional rotation. Recalling (2-36), it results in sinusoidal EMF, which can be used for energy regeneration. The dynamics of the sprung mass system are given by

$$m_{eq}\ddot{z}+kz+c_f\dot{z}+F_b=F_{road} \tag{2-41}$$

where z is the relative displacement between base and sprung mass (i.e. $z = x - y$); m_{eq} is the equivalent sprung mass; k is the physical spring coefficient; c_f is the physical friction coefficient; F_b is the equivalent force provided by ball screw, gearbox, DC motor/ generator , and load resistor R_{load}. The sprung mass dynamic equation, including the motor dynamics, can be expressed in detail as follows

$$\begin{aligned}
&\left(m+\frac{J_m k_g^2+J_g+J_b}{d^2}\right)\ddot{z}+c_f\dot{z}+kz\\
&+\left(k_e k_t k_g^2\left(R_{\text{int}}+R_{load}\right)\right)\left(\left(R_{\text{int}}+R_{load}\right)^2+\omega^2L_{\text{int}}^2\right)^{-1}d^{-2}\dot{z}\\
&+\left(k_e k_t k_g^2\omega L_{\text{int}}\right)\left(\left(R_{\text{int}}+R_{load}\right)^2+\omega^2L_{\text{int}}^2\right)^{-1}d^{-2}z\\
&=m\omega^2Y\sin\omega t
\end{aligned} \tag{2-42}$$

where Y and $\omega= 2\pi f$ are the excitation amplitude and angular frequency; m is the sprung mass; $d=l/2\pi$ is the screw lead linear- rotational ratio for torque-force conversion and l is lead ratio of the ball- screw; J_b is the ball-screw translational mass; J_m and J_g are the motor and gearbox inertia, respectively; the back EMF and torque constants of the DC machine are indicated by k_e and $k_{t,}$ respectively; the planetary gear ratio is represented by k_g, where it is implemented for torque/ angular velocity amplification on its' input/output terminals, respectively; and the DC machine winding loss and armature inductance are represented by R_{int} and L_{int}, respectively. Assuming $\omega L_{\text{int}} \approx 0$ the equivalent force F_b is given by

$$\left(J_m k_g^2 + J_g + J_b\right) d^{-2}\ddot{z} + \left(k_e k_t k_g^2\right)\left(R_{\text{int}} + R_{load}\right)^{-1} d^{-2}\dot{z} \ . \tag{2-43}$$

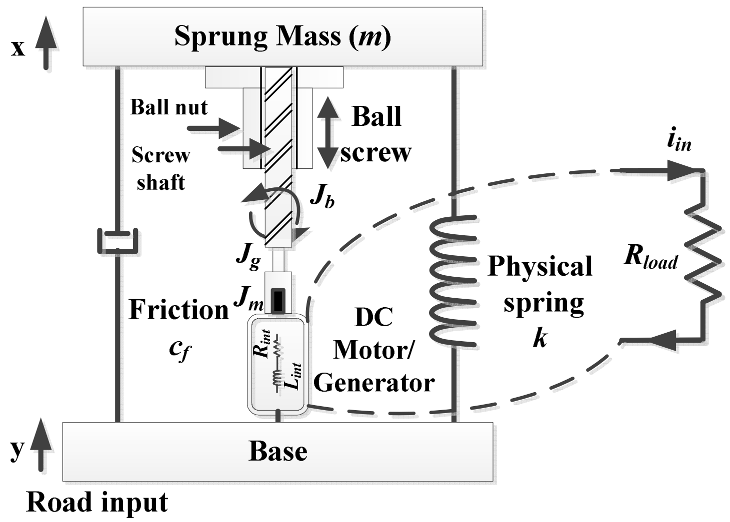

Figure 2-11: Regenerative suspension 1-DOF dynamic model.

Table 2-2: Equivalent mass, damping coefficient and excitation amplitude.

Symbol	Description
m_{eq}	$m + \dfrac{J_m k_g^2 + J_g + J_b}{d^2}$
c_{eq}	$c_f + \dfrac{k_e k_t k_g^2}{(R_{int} + R_{load})d^2}$
Y_t	$mY\omega^2$

As indicted in Figure 2-11 and Table 2-2, the load resistor R_{load}, connected to DC machine terminals, provides equivalent damping force in the electrical domain. In this work, the purpose of the proposed converter is to synthesize a variable R_{load} to achieve variable equivalent damping force by absorbing the corresponding power in the electrical domain. The equivalent mass, damping coefficient and excitation amplitude in terms of other physical parameters values are listed in Table 2-2. It is worthy to note that equivalent mass m_{eq} combines linear mass and rotational inertia, equivalent damping coefficient (i.e. $c_{eq}= c_f+ c_e$) combines both friction terms and electrical damping, synthesized by attached power electronics, which will be studied in later sections. The term Y_t represents the amplitude of sprung mass acceleration.

2.2.1. Regenerative Suspension Prototype

A 1-DOF regenerative suspension system, fabricated at the Intelligent Vehicles Lab at Simon Fraser University, is shown in Figure 2-12. The vibrational test-bed setup was developed to provide experimental verification of equivalent damping synthesis provided by the AC/DC converter, which will be presented in this Chapter. The electromagnetic-based suspension generates available AC power when placed under base excitation. As depicted, the 1-DOF quarter-car system prototype consists of a mass plate on bearings and four parallel springs. A MTS Hydraulic Actuator (Series 248) was utilized as an actuator to provide base excitation to the suspension system. A Maxon DC series motor (RE40-218011), attached to a planetary gearhead (GP52C-223083), was adopted to replace a traditional damper. A high helix lead THK ball-screw (KX-10) was connected to the DC motor for converting the vertical movement into the rotary motion. According to [50], the running efficiency of KX-10 can be assumed to be higher than 90%.

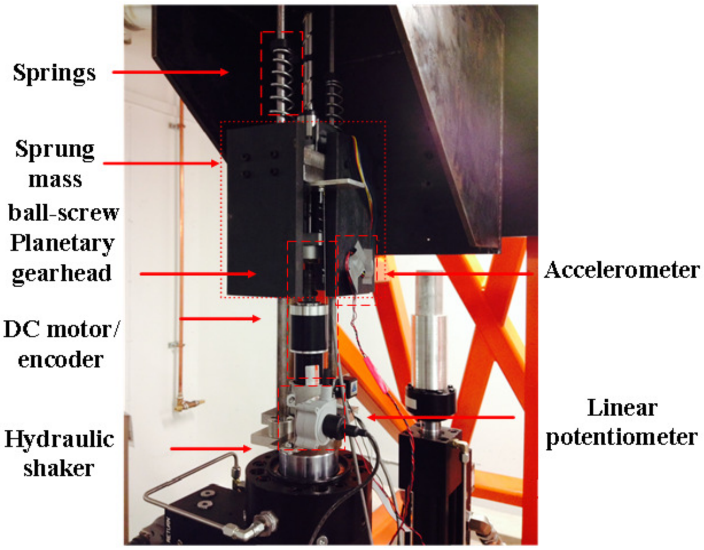

Figure 2-12: Electromagnetic suspension prototype test bed.

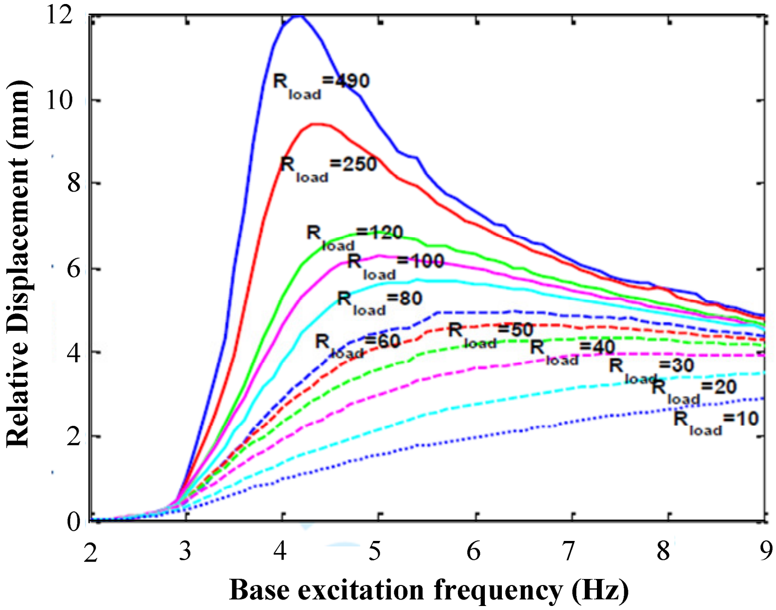

(a)

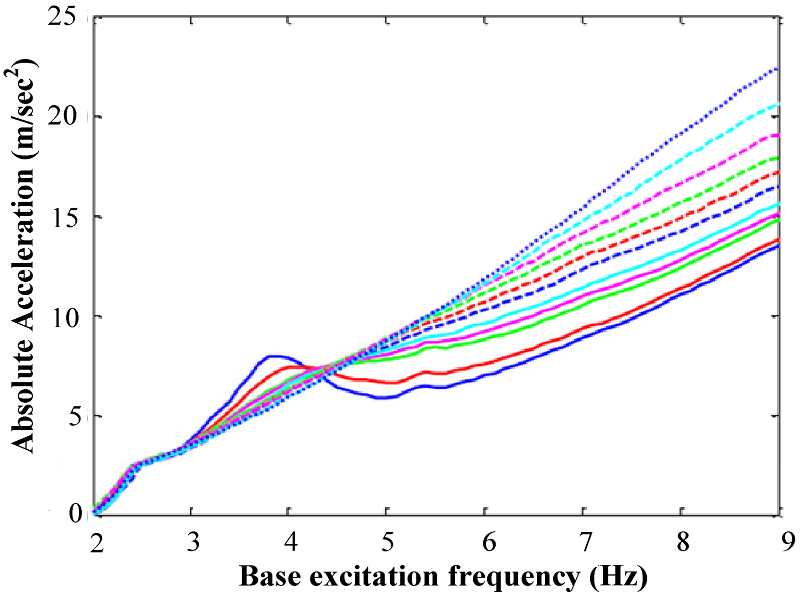

(b)

Figure 2-13: Experimental frequency response of (a) amplitude of relative displacements and (b) absolute acceleration with respect to various physical load resistors (Ω). Undamped natural frequency ≈ 6 Hz.

In addition, string potentiometers with spring loaded cable from Celesco SP212 were used for measuring the suspension relative displacement. The sprung mass acceleration was measured by 3-axis low power Analog Device ADXL- 326 accelerometers. The main parameter values of the experimental setup are tabulated in Table 2-4. Recalling Figure 2-11, various physical power resistors are attached to the terminals of DC machine for the generation of frequency responses (for excitation frequencies in the range: 2- 9 Hz) in terms of both suspension relative displacement and sprung mass absolute acceleration are shown in Figure 2-13. As indicated by Table 2-3 the selected resistance values is capable of applying equivalent damping in the electrical domain ranging from under to over- damped conditions (i.e. ξ= 0.059 to 1.46).

Table 2-3: Applied damping ratios to electromagnetic suspension prototype with respect to various load resistors.

Load resistors (Ω)	Damping ratio ξ	Load resistors (Ω)	Damping ratio ξ
10	1.46	60	0.42
20	0.98	80	0.33
30	0.73	100	0.27
40	0.59	120	0.23

50	0.49	250	0.11
		490	0.059

Table 2-4: Regenerative suspension experimental parameter values

Parameter	Value	Parameter	Value
Sprung mass	16 kg	DC motor internal resistance	10 Ω
Total spring constant	23548 N/m	Gear ratio of the gearhead	12:1
Rotor inertia of the DC motor	120 g-cm^2	Lead ratio of the ball screw *l*	60 mm/rev
DC motor torque constant	170 mNm/A	Travel length of the ball screw	300mm
Accelerometer sensitivity	≈57 mV/g	Potentiometer gain	≈3.93 V/m

2.3. Regenerative Power Electronics Topologies

Various types of energy harvesting systems have been reported in the literatures. Recently, regenerative suspension systems have become extremely popular for dual purposes of active suspension control and power regeneration. Several topologies of tubular electromagnetic based regenerative suspension mechanism incorporating permanent magnets have been proposed [52]- [55]. To harvest the ambient vibration energy, several converters have been proposed [56]-[58]. In [59], a piezoelectric-based energy harvester was presented by utilizing a buck and buck-boost converter. The method of impedance matching for maximum power transfer in a piezoelectric-based energy transducer was presented in [60]. A flyback converter with maximum power point tracking capability was presented in [61]. A MOSFET-based voltage doubler coupled with a boost converter was proposed in [62] for low voltage energy harvesting applications. In [63]-[64], the concept of energy harvesting by providing an equivalent damping was presented by utilizing a full-bridge rectifier and a DC/DC converter.

Larger scale electromagnetic type transducers have recently gained attention in the implementation of regenerative vehicular suspension systems and seismic structure dynamic suppression [52]. In this type of application, the power level (> 1W) is much higher than that of piezoelectric based converters (< 100 mW). Various types of mechatronic systems have been reported in the literatures along with electromagnetic dampers for regenerative vibration suppression and energy harvesting [66]-[69]. Permanent magnet based generators for converting linear reciprocating motion into electric energy were presented in [71]- [72]. A power converter for larger scale energy harvesters utilizes a synchronous boost rectifier capable of synthesizing constant input resistor for harvesting damped energy was proposed in [72]. The direct AC/DC converter demonstrated in [74] aims for seismic structure control and energy harvesting using tuned mass-spring-damper. The work lacks theoretical analysis in converter switch-mode operation, control, experimental verification, and requires large converter foot print. A DC/DC converter indicated in [75], for regeneration from an electromagnetic shock absorber, only included the simulation results of a buck/boost converter, however, various aspects, such as AC/DC rectification and converter experimental outcomes were not mentioned.

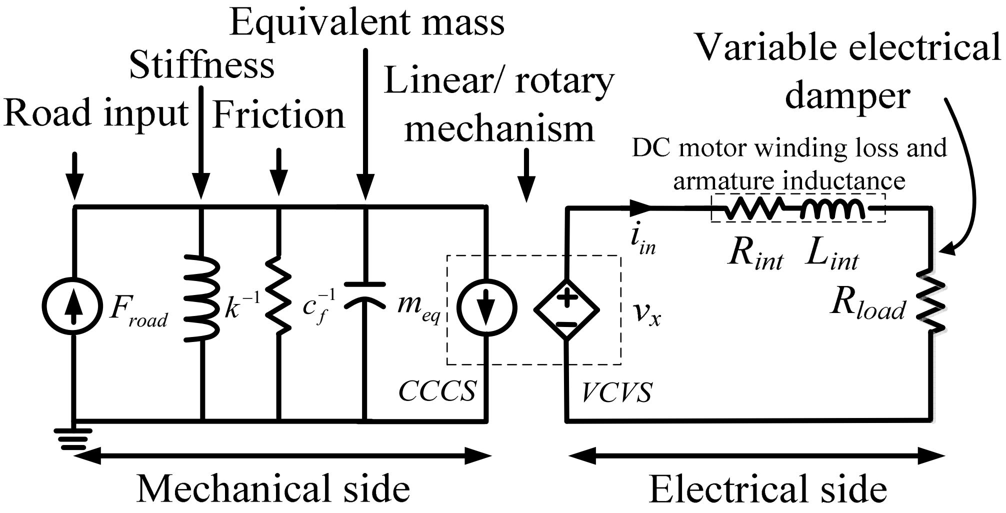

Figure 2-14: Analogous electrical model of 1-DOF regenerative suspension.

Referring to the adopted regenerative suspension system depicted in Figure 2-11, the power generated from the base vibration is distributed into mainly three parts: mechanical friction, electrical loss, and power transferred to load resistor (see Figure 2-11 (b)). To capture useful power, the amount delivered to the electrical load needs to be maximized. The total current passing through the electrical load and motor's internal resistor can be obtained as

$$i_{in} = \left(k_e k_g\right)\left(R_{\text{int}} + R_{load}\right)^{-1} d^{-1}\dot{z} \tag{2-44}$$

To analyze power regeneration by R_{load}, a mechanical-electrical analogy is adopted as shown in Figure 2-11 (b). According to [50] and considering (2-41), the road force, equivalent mass, physical stiffness, and equivalent damping are analogous to current source, capacitance, inverse inductance, and inverse resistance in the electrical domain, respectively. The DC machine provides available power to R_{load} and supplies mechanical torque proportional to the current i_{in}. Therefore, the DC machine is represented by a current controlled current sink (CCCS) and voltage controlled voltage source (VCVS) in the mechanical and electrical domains, respectively. The DC machine back- EMF v_x is given by

$$v_x = \left(k_e k_g\right) d^{-1} \dot{z}\,. \tag{2-45}$$

The instantaneous electrical power generated by the damper is a function of the relative speed of the system, which is

$$p_{inst} = \left(k_e k_g\right)^2 \left(R_{\text{int}} + R_{load}\right)^{-1} d^{-2} \dot{z}^2\,. \tag{2-46}$$

Assuming $z = A\sin\left(\omega t + \theta\right)$, the average power flow per cycle is calculated as

$$p_{avg} = 0.5\left(A\omega\right)^2 \left(k_e k_g\right)^2 \left(R_{\text{int}} + R_{load}\right)^{-1} d^{-2} \dot{z}^2\,. \tag{2-47}$$

2.4. Construction of Standardized Road Profiles

The objective of modeling standardized road profile is to obtain the dynamics of vehicle tires when placed under realistic excitations. According to ISO 8608 [76], the road profiles can be characterized by power spectral densities Φ (PSD) defined as

$$\Phi\left(\Omega\right) = \Phi\left(\Omega_o\right)\left(\frac{\Omega}{\Omega_o}\right)^{-w}\,. \tag{2-48}$$

where wavenumber Ω_o = 1 rad/m and w is defined as road waviness, which describes the reduction of vibration PSD along the angular wave numbers (rad/m). The value of w= 2 has been widely recognized [78]. Various classes of road roughness are defined by values of $\Phi(\Omega_o)$. As depicted in Figure 2-15 (a), PSD of road classes B (i.e. 4^1 μm^3/rad) to D (i.e. 4^3 μm^3/rad) have been delineated.

According to [76]- [77], the road profile X is derived by the summation of sinusoidal waveforms (with size of N), which can be written as the following

$$X = \sum_{j=1}^{L\times N_t} \sum_{i=1}^{N} A_i \sin\left(\Omega_i D_j - \psi_i\right). \tag{2-49}$$

where N and N_t indicates the number of points taken along the wavenumber axis and in one meter of road disctance, respectively. The phase Ψ_i is pseudorandom and normally distributed between [0 2π]. The vehicle traveled distance is defined by L, which the sampling rate D_j is determined by the total number of sampling point taken throughout the entire traveled distance (size: $L\times N_t$). The excitation amplitudes A_i is given by

$$A_i = \sqrt{2\Phi\left(\Omega_i\right)d\Omega} \tag{2-50}$$

where dΩ is the step size taken from the wavenumbers. Referring to PSD profiles in Figure 2-15 (a), it allows the realization of ISO standard excitation profiles by (2-48)- (2-50). In this case, the road profiles from class B to D for the distance of 100 (m) has been reconstructed in Figure 2-15 (b). The class C road profiles with nominal values of i=1, 2 and 100, 200 within 100 samples are depicted in Figure 2-16 (a) and (b), respectively.

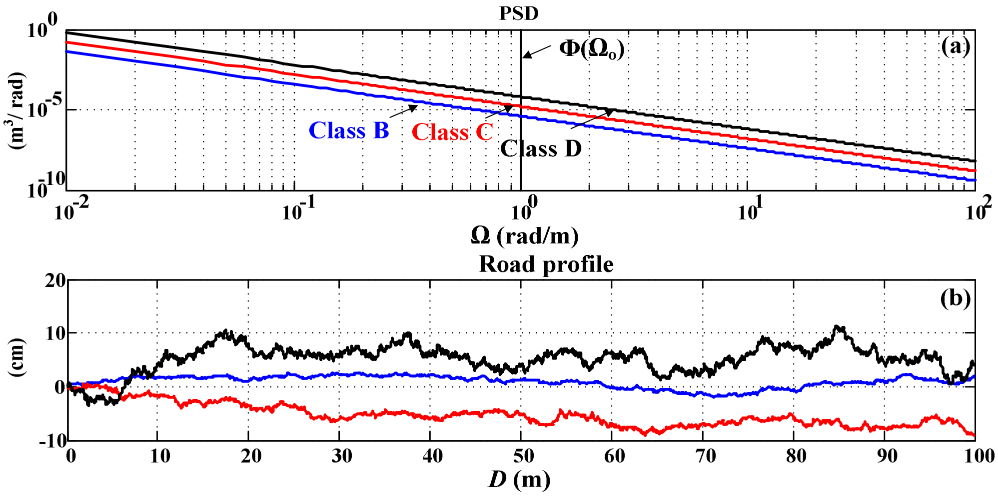

Figure 2-15: (a) PSD $\Phi(\Omega)$ and (b) road profile X (in cm) of ISO 8608 road class B to D.

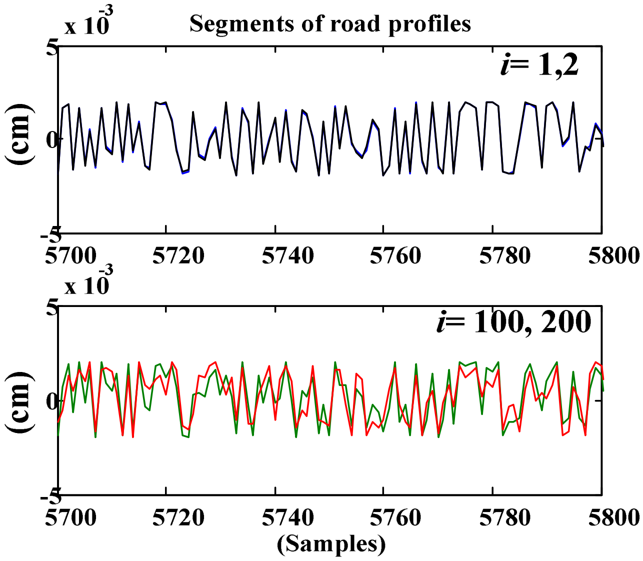

Figure 2-16: Nominal longitudinal class C road profiles with (a) *i*= 1, 2 and (b) 100, 200 within 100 samples.

Alternatively, according to [78], the road profile can also be constructed, with respect to temporal excitation frequency, by passing a unit- intensity white noise through a low pass filter (LPF) expressed as

$$G(s) = \frac{\sqrt{2\pi G_r V}}{s + w_o} \tag{2-51}$$

where $G_r = \Phi(\Omega_o)/(2\pi)^2$ is the roughness coefficient with $\Phi(\Omega_o)$ expressed in (m^3/ cycle), V is the vehicle velocity, $w = 2\pi V v$ is the temporal excitation frequency with wavenumber v in (cycle/m), and $w_o = V$ is the cut-off frequency of the LPF. The instantaneous waveform and amplitude spectra of a white noise with unit intensity are shown in Figure 2-17. As indicated by (2-51), higher road class and faster vehicle velocity amplifies the gain and extends the cut-off frequency of the white noise LPF, which means assuming fixed travel duration higher vehicle velocity and rougher roads will provide higher available energy.

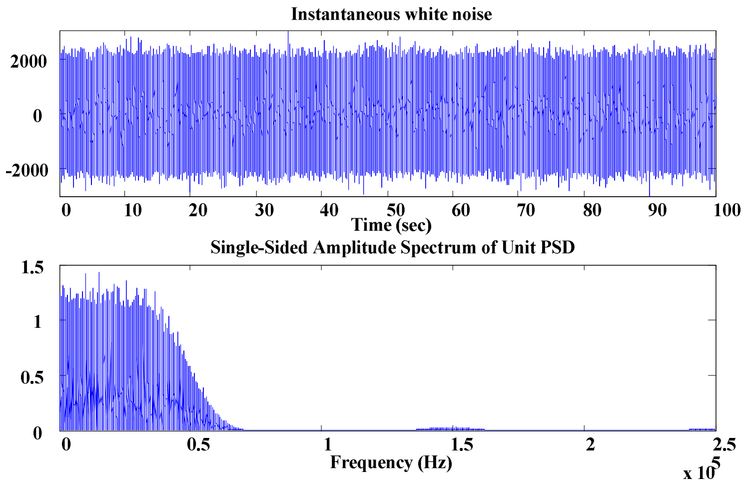

Figure 2-17: (a) Instantaneous waveform and (b) spectra amplitude of a white noise with unit intensity. Sampling frequency: 0.5 Mhz.

To illustrate the excitation frequency compositions, an instantaneous ISO8608 class C longitudal road profile with its corresponding amplitude spectrum, obtained by Fast Fourier transformation, are shown in Figure 2-18 (a) and (b), respectively. The amplitude spectrum, in terms of excitation frequency, is obtained as follows

$$\left|X(f)\right| = \sum_{i=1}^{N} x(i) e^{-j2\pi N^{-1}(i-1)(f-1)} \tag{2-52}$$

where N is the vector length. As indicated, higher excitation frequencies contribute to less composition of the instantaneous road profile. In addition, both amplitude and phase of the LPF comprised of road profile PSD (see Figure 2-15) and vehicle tire are shown in Figure 2-18 (c) and (d). In this case, the 2-nd order LPF is as follows

$$G(s) \approx \frac{1.26}{s^2 + 251.3s} \tag{2-53}$$

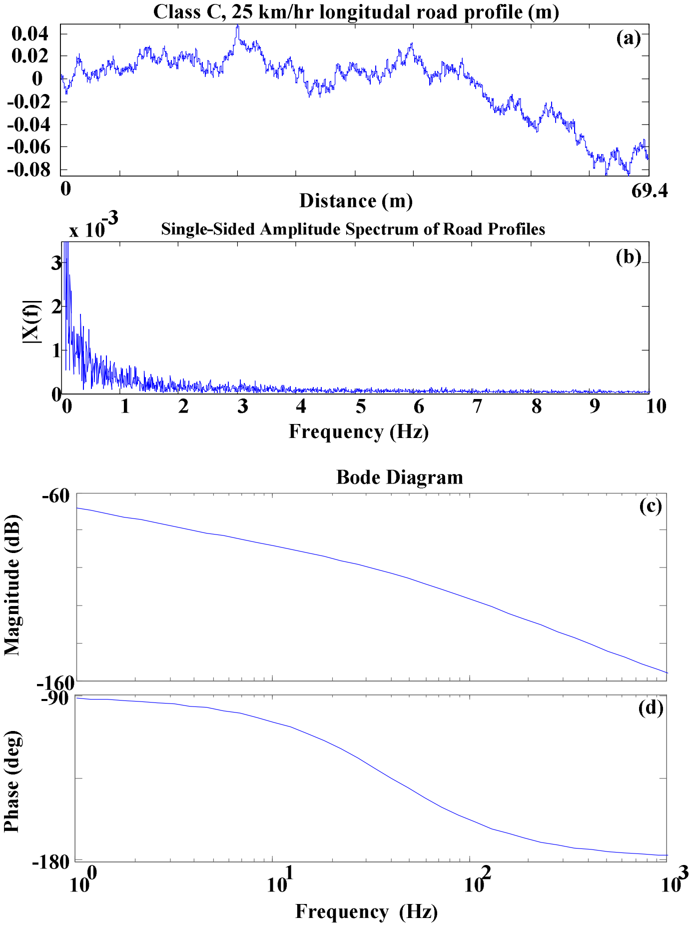

Figure 2-18: (a) Class C longitudal road profile in 69.4 (m) and its' (b) single- sided amplitude spectrum. Bode plot of combined class C PSD and vehicle tire dynamics in both (c) amplitude and (d) phase. Note: Sampling frequency= 0.5 MHz.

2.5. Full- sized Vehicle Power Regeneration Potential

Based on the experimental results of a small-scale suspension prototype (to be outlined in later chapters), one can estimate the available energy distribution and total energy regeneration under various ISO road classes for full-size vehicles. In this work, to illustrate the power regeneration potentials, both full-size electric vehicle (e.g. Tesla Model S) and 6-wheeled recreational vehicle (e.g. Autotrail Frontier Chieftain Motorhome) can serve as suitable examples.

According to Figure 2-19 (a), the boundaries "*o*-*b*" indicates energy distributions taking place in a regenerated suspension system, generally. As depicted, the available energy is comprised of kinetic/ potential, damped, and regenerated energies. The exchange between kinetic and potential provides sprung mass oscillation, which implies indefinite oscillation when the damped energy is absent. This also indicates the amount of avaialbe energy that is not harvestable. The boundary "*b*- *c*" indicates energy loss of ball-screw friction and DC motor armature coil. It is noted the calculation of the ball- screw driving efficiency (or energy loss) between "*b*- *c*" is calculated by forces between moving the ball nut and screw shaft. The boundaries "*c*- *e*" indicates energy distribution in the electrical domain, where charged energy is obtained by subtracting converter energy loss.

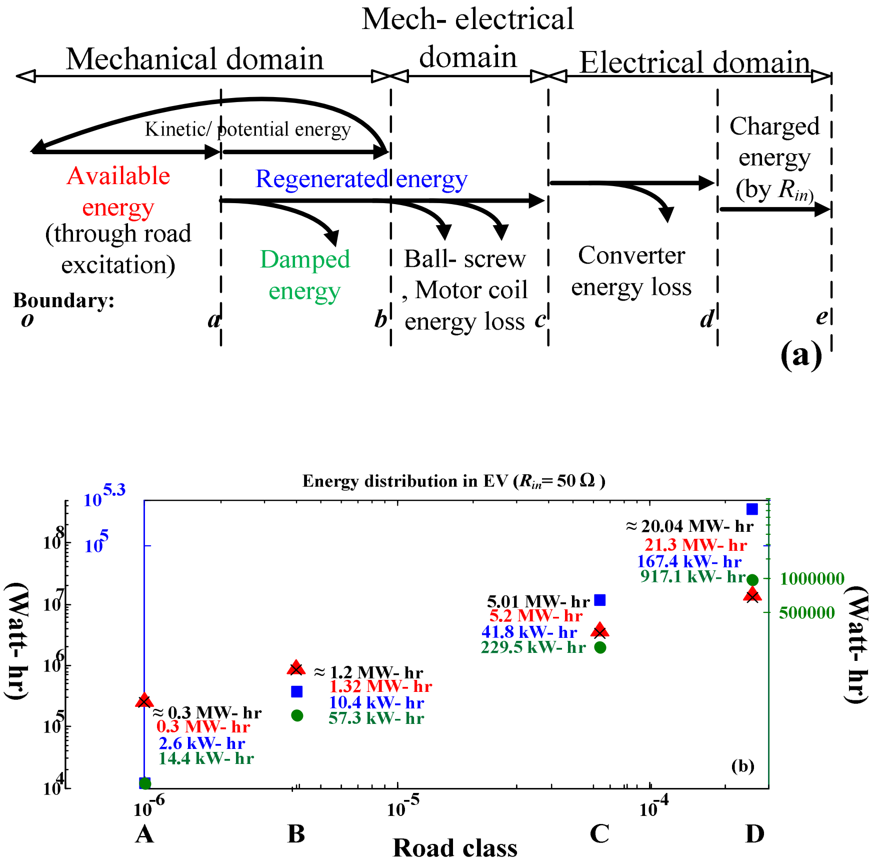

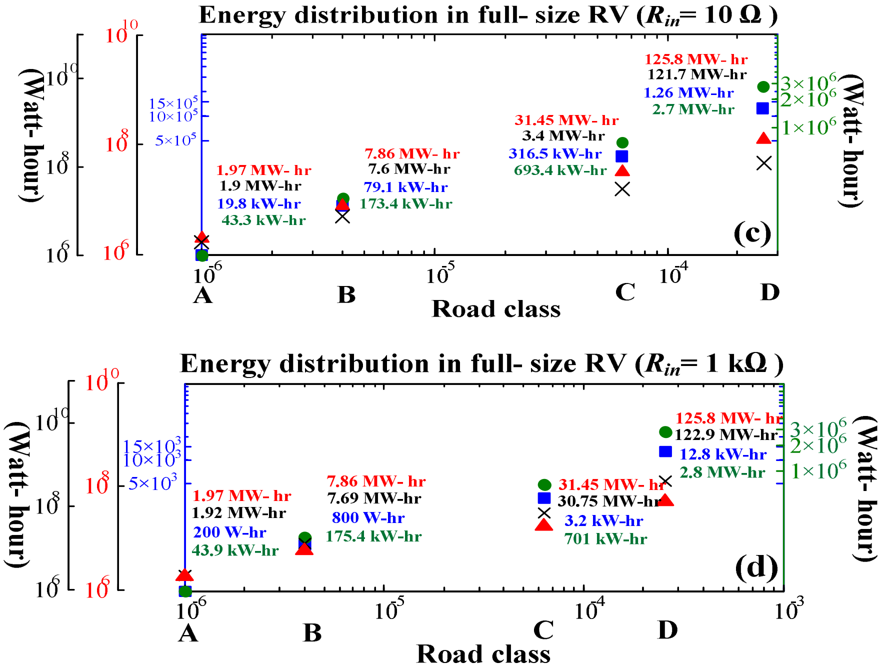

Figure 2-19: (a) Estimation of regenerated energy distribution in an electromagnetic suspension. (b) Energy distribution of a full-size EV with R_{in} = 50 Ω over 4 (hr) trip and (c) a typical RV with R_{in} = 10 and (d) 1 kΩ per hour under ISO 8608 class A to D roughness, $\Phi(\Omega_o)$. Note: Sampling rate: 1 kHz. Legends are ▲: Available energy, ×: Sum of kinetic and potential energies, ■: regenerated energy and ●: friction damped energy. Note: Sampling rate: 1 kHz. Legends are ▲: Available energy, ×: Sum of kinetic and potential energies, ■: regenerated energy and ●: friction damped energy.

As depicted in Figure 2-19 (b)-(d), various legends are delineated to represent ▲: Available energy, ×: Sum of kinetic and potential energies, ■: regenerated energy and ●: friction damped energy. In this case, assuming quarter of a full-size EV weighs approximately 0.5 ton with moderate stiffness coefficient k= 23245 N/m (i.e. 131 lbs/in) and c_f= 5 kN sec/m, it follows that synthesizing R_{in}= 50 Ω (≈ 700 N sec/m) provides the suspension damping ratio $\zeta \approx 0.8$. According to [79], the range capacity of a Tesla Model S is approximately 335-426 km while equipping 60-85 (kW-hr) rated Lithium-Ion battery packs. Assuming the battery is capable of powering the EV for travelling at constant speed of 85 km/hr for 4 hours (e.g. Ottawa, ON to Toronto, ON) before drainage, therefore, as depicted in Figure 2-19 (b) a single suspension is capable of regeneration approximately 2.6 to 167 kW-hr in 4 hours trip duration, depending on various ISO road classes. Thus, the regeneration capacity over the trip duration is comparable to that of the EV battery packs, which indicates the feasible potential of harvesting road energy for further extending the vehicle's range capacity by at least 12-15% (10.4 kW-hr/60 kW-hr assuming smooth road, ISO8608 class A, with four regenerative suspensions in 4 hours). This is equivalent to range extension of 50 to 70 km for the Tesla Model S.

In addition, the total recreational vehicle (RV) mass of roughly 12.5 ton is evenly distributed to the suspensions while V= 85 km/hr, k= 23245 N/m and c_f= 10 kN sec/m, the total of 3.2 to 316.5 (kW- hr) while driving on typical ISO 8608 class C road for one hour can be obtained by the adopted DC generator/ ball- screw mechanism. It is worthy to note, with c_f= 10 kN sec/m, synthesizing R_{in}= 10 Ω (i.e. c_e= 2.28 kNs/m by substituting in Table 2-4) to 1 kΩ (c_e= 45.6 Ns/m) represents cases of critically and under damped for the sprung mass dynamics, respectively. Therefore, according to [80], for a typical 5- hour road trip (e.g. Vancouver, BC to Osoyoos, BC), on average road condition, the available power provided by the road surface allows powering the on- board recreational appliances for at least 12 (hr).

2.6. Chapter Summary

In this chapter, models for one and two DOF dynamic systems were obtained to demonstrate the responses of sprung mass under base excitations. Moreover, the modelling of ISO 8608 road profiles, for different road roughnesses, was described. The model allows realistic estimation of road energy harvesting for full-scale vehicles (e.g., full- size sedan and recreational vehciles). In addition, the power regeneration mechanism of DC machine under road excitation was investigated. The detailed modeling of a current controlled switched-mode rectifier (SMR), synthesizing variable electrical dampers, for the purpose of energy harvesting will be presented in the next chapter.

Chapter 3.

Bi- directional Switch Mode Rectifier for Synthesizing Variable Damping and Semi- Active Control

In this chapter, the concept of using a switch-mode rectifier (SMR) for synthesizing a variable electrical damper is demonstrated. Along with hysteresis current control, it is shown that both the amplitude and phase of the converter current can be controlled, with respect to irregular and stochastic generated back-EMF voltage, which is equivalent to turning the desired synthesized resistor values. According to the derivations shown previously, this is equivalent to tuning the mechanical damping coefficient through capturing road-induced vibration energy.

3.1. Converter Modeling

The bi- directional power converter for synthesizing variable resistor is shown in Figure 3-1. The synthesizer is essentially a current controlled switch-mode rectifier (SMR) operating in the continuous conduction mode (CCM). As depicted, the power stage consists of a physical power inductor and a single phase Voltage Source Inverter (VSI) for providing the desired 3-level v_c through the corresponding PWM pulses driving the power MOSFETs. Before synthesizing variable resistors in a switch- mode converter, we consider a general variable resistor, R_{in}, shown in Figure 3-2. The value of R_{in} is determined through the amplitude/phase relationship between resistor voltage, $V(t)$, and current, $i(t)$ as seen in (3-1). Assuming both $V(t)$ and $i(t)$ are completely in-phase (i.e., high power factor), varying the ratio between both waveforms is synonymous to changing terminal resistance R across the terminal “a-b”.

$$R_{in} = V(t)\,i^{-1}(t) \tag{3-1}$$

Consider a resistive load shown in Figure 3-3 (a) which is obtained through synthesyzing a variable resistor across the terminal voltage (V_x), and current (i_{ref}). The single phase AC source along with its internal impedance (i.e., Z_s) is connected to a virtual resistor where the phase relationship between V_x, and i_t is expected to be equivalent to that of a physical resistor with the same value. Referring to Figure 3-3 (b) the variable resistor synthesizer consists of a physical inductor L_a and a controlled voltage source V_c with Z_s (i.e. *R-L* series) representing the source impedance, and V_c indicating an equivalent voltage source generated by a single phase 3-level VSI [87]- [88].

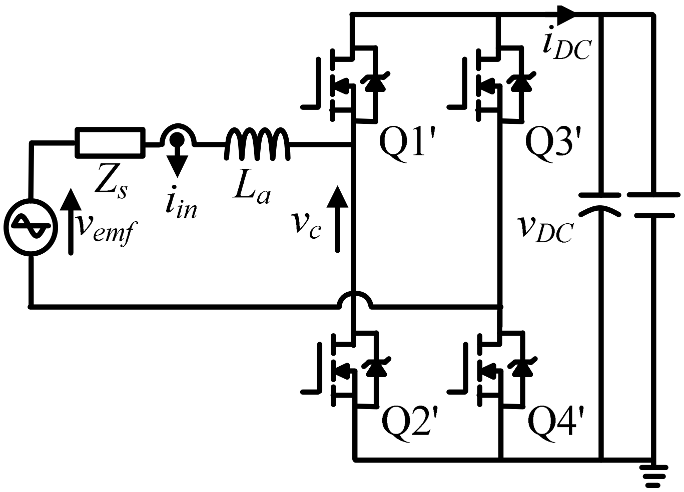

Figure 3-1: Switch- mode boost rectifier topology.

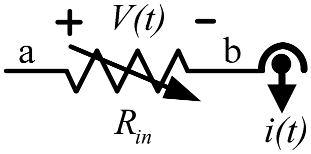

Figure 3-2: Concept of resistance synthesis

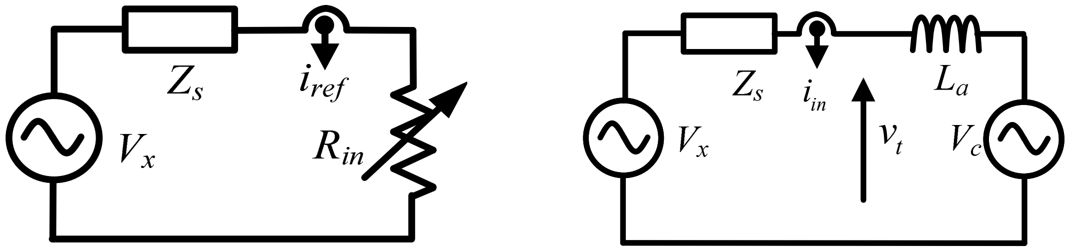

(a) (b)

Figure 3-3: Equivalent model of variable resistance synthesis (in Laplace domain variables)

If the driving point impedance at the terminal (shown by "+/-") in both Figure 3-3 (a) and (b) can be assumed resistive, the current flowing through both circuits can be equated. Defining the variables I_{in}(s) and I_{ref}(s) as Laplace domain representation of terminal current i_{in} and reference current i_{ref} one will obtain the following:

$$I_{ref}(s) = \frac{V_x(s)}{Z_s + R_{in}} \tag{3-2}$$

$$I_{in}(s) = \frac{V_x(s) - V_c(s)}{Z_s + sL_a} \tag{3-3}$$

To ensure correct resistor synthesis the expression between source voltage (V_x) and controlled voltage source (V_c) is derived next. By equating (3-2) to (3-3) the expression of V_c in both time and Laplace domains can be obtained as the following:

$$v_c = v_x - R_s i_{in} - \left(L_a + L_s\right)\frac{di_{in}}{dt} \tag{3-4}$$

$$V_c(s) = \frac{R_{in} - sL_a}{Z_s + R_{in}} V_x(s) \tag{3-5}$$

where R_s and L_s represents the motor internal impedance, R_{in} is the desired variable resistance and L_a is the line inductor. The transfer function indicates the relationship between $V_x(s)$ and $V_c(s)$, where the amplitude attenuations and phase shifts are determined by values of passive elements. Thus, by controlling $V_c(s)$ to follow the relationship in (3-5) ensures the correct synthesis of R_{in}.

3.2. Regeneration and Motoring Modes

The purpose of operating in the regenerative mode is to harvest energy from the suspension mechanism through the electric machine while providing positive damping force to the suspension system. In the regenerative (motoring) mode, during positive cycle of line voltage, positive (negative) source power contributes to storing (dissipating) of DC bus energy (i.e., battery). This condition indicates a charging (discharging) operation.

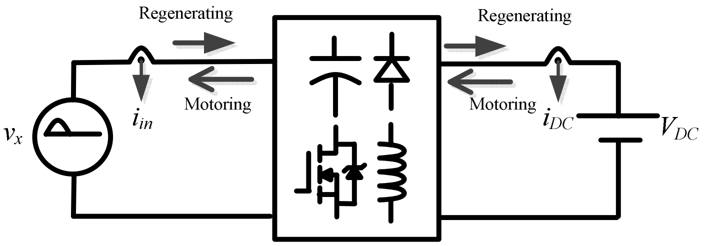

Figure 3-4: Motoring and regeneration states by direction of current.

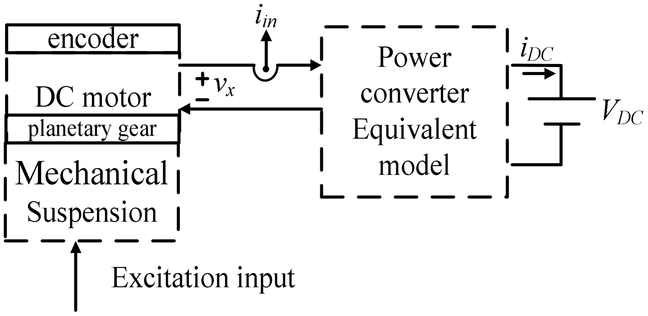

Figure 3-5: Configuration of regenerative suspension indicating the power converter providing the desired equivalent dynamics through v_x and i_{in}.

Referring to Figure 3-4 and Figure 3-5 the role of power converter is to convert the kinetic energy, induced by excitation input, to the load battery V_{DC}. Here, we defined the average harvested power as follows

$$\bar{P}_{DC} = T_s^{-1} \int_t^{t+T_s} i_{DC} v_{DC} dt \tag{3-6}$$

where T_s is EMF voltage period (i.e. line period), i_{DC} is defined as the charged current, v_{DC} is the battery voltage . According to Figure 3-3 (b), the average controlled voltage source v_c generated by a single phase VSI through the following

$$v_c = T_{sw}^{-1} \int_t^{t+T_{sw}} v_{DC} dt \tag{3-7}$$

where T_{SW} is the MOSFET switching period. Recalling (3-5), it is also noted the limitation of SMR in synthesizing variable resistors is limited by R_s. Referring to Figure 3-2 and assuming $i_{in}= i_{ref}= V_x(R_{in})^{-1}$, theorectically the converter is operating in regeneration mode when $R_{in}>R_s$, since in low operating frequency we can assume $v_c \approx v_x - R_s i_{in} \approx v_x - \frac{R_s}{R_{in}} v_x$. Having $R_{in}>R_s$ ensures both v_c and v_x have the same polarity. Since the purpose of the converter is synthesizing variable resistors (i.e. resistive behavious at the line terminal), meaning both v_c and i_{in} waveforms will be in- phase, ideally. When $R_{in}< R_s$, v_c indicates opposite polarity to that of v_x, which means both v_c and i_{in} waveforms are out of phase, thus the converter is operating in motoring mode. The maximum negative synthesized resistor (i.e. $R_{in}< 0\ \Omega$) is limited by the value of battery voltage or inverter voltage, since $v_c \approx v_x + \frac{R_s}{R_{in}} v_x$.

Having the equivalent model of the SMR we are able to model the average battery consumed/ harvested power as the following

$$\bar{P}_{DC} = T_s^{-1} \int_t^{t+T_s} v_c i_{in} dt \tag{3-8}$$

Again, since torque generated by a DC motor is directly related to its current, thus i_{in} represents the desired response synthesized in the electrical domain. Recalling (3-4) - (3-5) and assuming voltage drop between L_a and L_s is negligible (i.e. $L_a \frac{di_{in}}{dt} + L_s \frac{di_{in}}{dt} \approx 0$ V) due to low excitation frequency, thus the phase difference between v_x and v_c is negligible. The amplitude difference is correlated to the motor/ generator loss since $v_c \approx v_x - R_s i_{in}$, meaning, by adjusting the duty cycle of the VSI according to i_{in} the desired v_c can be obtained.

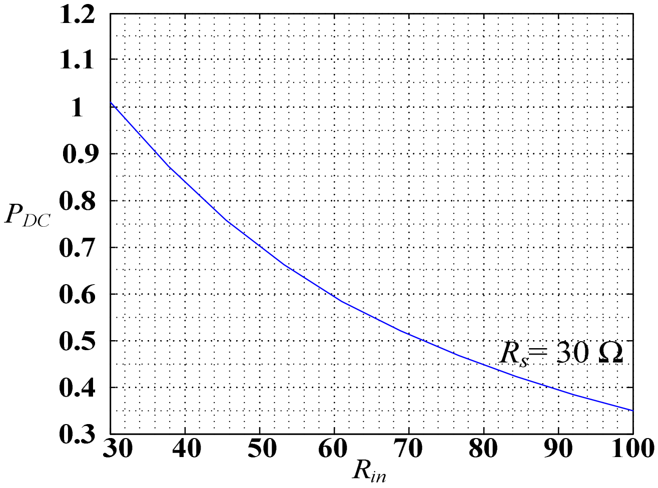

Figure 3-6: Average regenerated power $\overline{P}_{DC}$ (watts) with R_{in}= 30 to 100 Ω and v_x= 10 *sin*(20πt).

Hence, for illustration purposes and assuming R_s= 30 Ω, according to the defined direction of $\overline{P}_{DC}$ and Figure 3-6, it indicates power charging (i.e. regeneration mode) when $R_{in} \geq R_s$. It is noted as R_{in} increases the amount of average harvested power decreases, when $R_{in} \approx R_s$ leads to maximum $\overline{P}_{DC}$ with lower conversion efficiency, which will be shown in details in later sections. This is a typical trade-off for maximum power transfer. It also shows that in order to enlarge the range of synthesized R_{in} (by AC/DC converter) the selection of DC machine in terms of its equivalent resistor (R_s) coil loss is imperative.

3.3. Hysteresis Current Control

3.3.1. Double- band Three-level Hysteresis Current Control

In this work, a double-band hysteresis current controller (DB- HCC) was implemented to control i_{in}. The variable sampling frequency modulating scheme is implemented for its wide bandwidth and fast transient response, unconditional stability [81]-[86], full expandability to multi-level topologies (e.g., flying capacitor, neutral point clamp, cascaded H-bridge topologies for lower transistor electromagnetic interference EMI/ inverter total harmonic distortion THD), and accurate line resistor synthesis. The SMR with a controller consists of hysteresis comparators with two different sizes of error-bands are shown in Figure 3-7. In order to control v_c for correct R_{in} synthesis the terminal current i_{in} should be regulated to follow i_{ref}, as recalled in (3-5). The controller consists of hysteresis comparators with two different sizes of error-bands as shown in Figure 3-7 (b). With the desired gating signals for Q1-4, additional digital logic circuits were introduced for MOSFETs switching frequency (i.e. switching power loss) reduction and equalization, synonymous to carrier- based PWM modulation [87]- [88]. As a result, the average switching frequency is given by

$$f_{sw} \approx v_{DC} k \left(0.6 - 0.5k\right) \left(L_a \Delta I\right)^{-1} \tag{3-9}$$

where $k = v_{emf}/v_{DC}$ is the modulation index, ΔI is the small error band, and v_{DC} is the inverter input voltage.

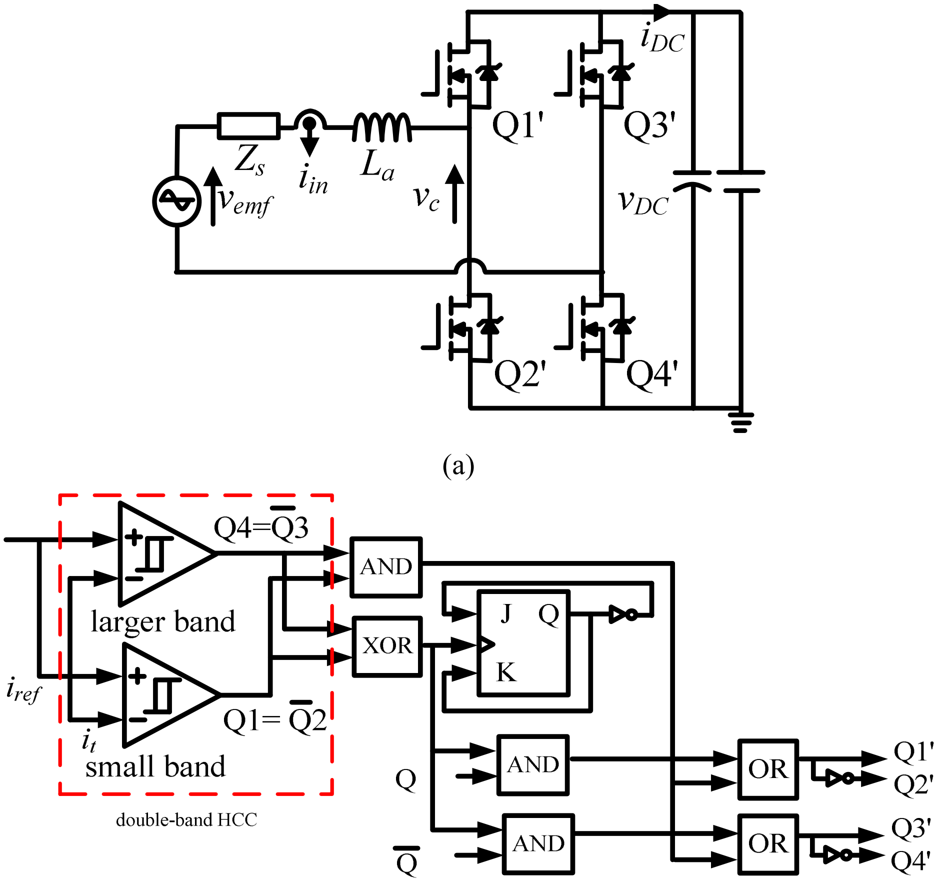

(a)

(b)

Figure 3-7: (a) SMR. (b) Double-band 3-level HCC.

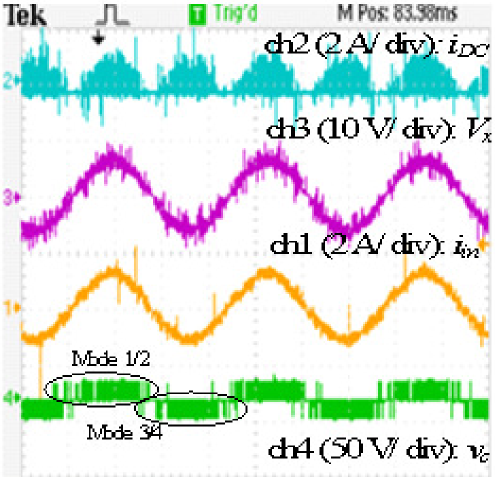

Figure 3-8: Oscilloscope waveform of $R_{in}= 5\ \Omega$ synthesis with corresponding AC source V_x, input current i_{in}, rectified current i_{DC}, and VSI voltage v_c. Note: V_x indicates independent AC source while v_{emf} represents dependent voltage source (i.e. DC machine back- emf)

The control method was implemented under MATLAB/ SIMULINK real-time workshop environment and built to the target hardware (TI TMS320F DSP). To verify synthesized R_{in}, V_x (oscillating at 5 Hz while supplied by Chroma 61501 programmable AC source) and i_{in} are captured as shown in Figure 3-8. In this experiment, a nominal $Rin= 5\ \Omega$ is emulated by the corresponding v_c (ch4), which can be verified through the amplitude ratio/minimum phase shifts (i.e. high power factor) between V_x (i.e. ch3) and i_{in} (i.e. ch1). In addition, the rectified current, i_{DC} (ch2) indicates the current charges the load battery in equivalent circuits Mode-2 (positive line cycle) and 4 (negative line cycle), as shown in Figure 3-9.

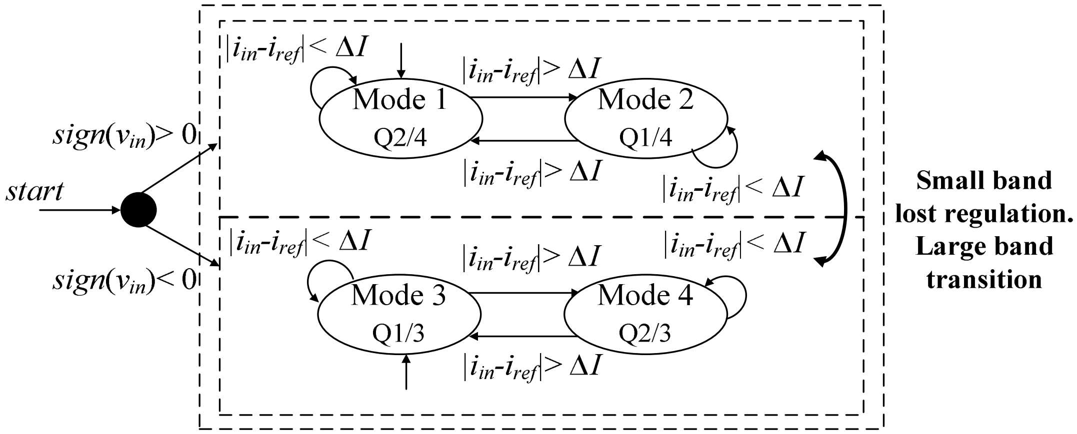

Figure 3-9: State diagram of DB- HCC.

The current ripple is primarily determined by smaller error-band hysteresis comparator while the large error-band hysteresis comparator is implemented to reverse the polarity of v_{DC}, when the smaller error-band comparator is unable to regulate the current error. Under this condition, the larger error-band comparator will activate to accomplish polarity reversal. Referring to the controller state machine shown in Figure 3-9, it is assumed the converter initially operates in the regeneration state with $sign(v_{in}) >0$. The smaller error-band comparator acts as a single-band hysteresis comparator, which switches on either Q1 or Q2 according to the error current (i.e., $\Delta I = i_{ref} - i_{in}$), defined as the difference between reference current i_{ref} and measured current i_t. When $|i_{in}-i_{ref}|< \Delta I$, Q2/4 are switched on, connecting v_{in} to L_a, which charges it at the rate of $\Delta i_t = V_x/L_a$. When $|i_{in}-i_{ref}|> \Delta I$, Q1/4 are switched on thus i_{in} into battery at the rate of $\Delta i_{in} = (v_x\text{-}V_{DC})/L_a$. Subsequently, when $sign(v_{in}) <0$, Q3 will switch on with either Q1 or 2 depending on the output of the smaller error-band comparator. The large error-band comparator switches on Q3 or 4 for v_{DC} polarity reversal, which takes place when the small error-band lost regulation (e.g. $sign(v_{in})$ reversal).

To verify the DB-HCC control law state diagram, Figure 3-10 (a) indicates i_{err} over duration of 1 (sec). In this case, the nominal small and larger bands are 5 (mA) and 1 (A), respectively. Essentially, the control method regulates i_{err} by presenting different values of v_c, generated by VSI. The detailed i_{err} shows lost regulation of small- band and transitioning of large-band are depicted in Figure 3-10 (b). The detailed switching mode transitioning clearly demonstrates through i_{err} switching waveform in Figure 3-10 (c). Referring to the transition from Mode 1 (point "a"), when $i_{err}= |i_{in}-i_{ref}|< 5$ (mA). Subsequently, to reduce i_{err}, Mode 2 activates when $i_{err}> 5$ (mA). Later, Mode 1 is activated again to increase i_{err}. Due to variation of line voltage v_{in} (point "b"), Mode 1 is no longer sufficient to regulate i_{err} within the small- band. Eventually, when $i_{err}> 10$ (mA), at point "c", small- band officially lost regulation and v_{DC} reversal takes place. In this case, Mode 4 is activated to increase i_{err}. Afterwards, to reduce i_{err}, Mode 3 activates when $i_{err}> 5$ (mA).

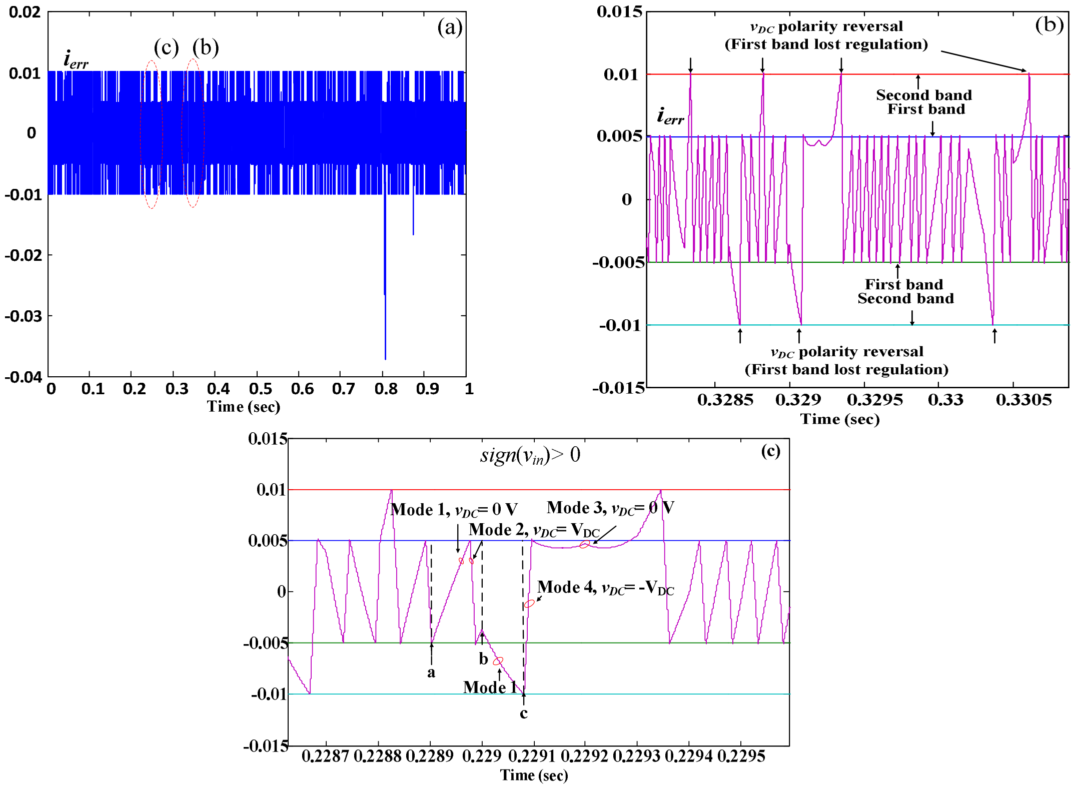

Figure 3-10: (a) Error current i_{err} over duration of 1 (sec) with small and larger error bands of 5 (mA) and 10 (mA), respectively (b) Detailed i_{err} indicating lost of first band and activation of second band. (c) Detailed i_{err} switching waveforms showing the transition between switching modes with *sign* $(v_{in})> 0$.

Variable Resistor Synthesis using Three- level HCC

The simulation of the 3-level HCC controlled SMR is performed in MATLAB/SIMULINK/ Simscape/SymPowerSystem environment. The values of SMR and DB-HCC are L_a= 1 mH (with ESR= 1 mΩ,), v_{DC} = 24 V, small and large error- band = 0.01 A and 0.02 A, respectively. The variable resistor syntheses R_{in} are swept from 100 Ω to 25 Ω in 0.8 (sec) durations. As indicated in Figure 3-11 (a), the line voltage v_x is oscillating at 10 Hz with amplitudes of 10 V for nominal duration of 0.8 (sec). The voltage v_c, depicted in Figure 3-11(b), is generated by the single- phase voltage source inverter according to the corresponding pulse-width modulated (PWM) signals generated by the 3- level HCC for synthesizing the desired R_{in}.

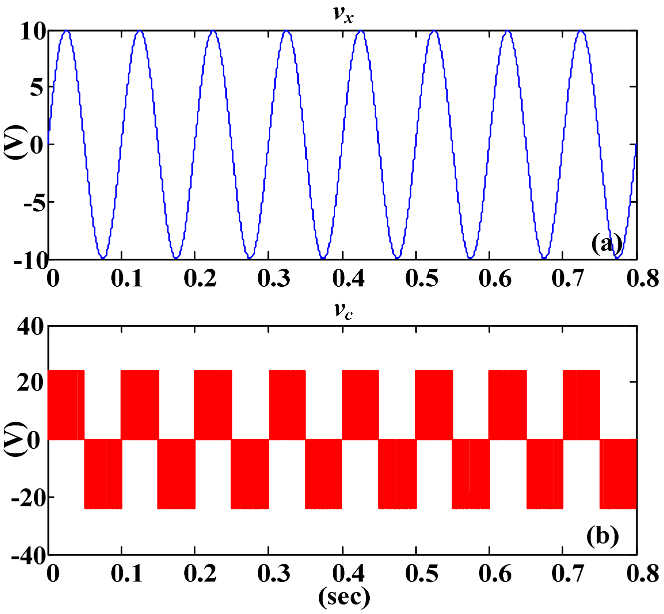

Figure 3-11: (a) Line voltage. (b) 3- level controlled inverter voltage for R_{in} sweep.

Synthesizing R_{in} is equivalent to controlling the converter current i_{in} to follow the reference current i_{ref}, which is calculated by dividing v_x by the desired R_{in}. Therefore, referring to both reference current $i_{ref}$and converter current i_{in}, in Figure 3-12, it is realized the desired R_{in} can be verified through the corresponding amplitude ratio between v_x and i_{in}. It is noted that both waveforms indicate a high power factor (PF). Also, the amplitudes of i_t increase with respect to decrease of R_{in}. In this simulation, R_{in} varies from 100 Ω to 50 Ω and 50 Ω to 10 Ω at t= 0.25 and 0.5 (sec), respectively. In order to illustrate the steady- state error of resistor synthesis by 3- level HCC, we define i_{in}= i_{ref}+Δh, where Δh is the small error- band bandwidth. Therefore, the error of resistance synthesis equals to the difference between desired synthesized and measured resistors (i.e. $\Delta R_{in} = R_{ref} - R_{in} = v_{emf} i_{ref}^{-1} - v_{emf}\left(i_{ref} + i_{err}\right)^{-1} \approx R_{ref}^{2} \Delta h v_{emf}^{-1}$). For example, when V_x= 10 V, R_{ref}= 25 Ω, Δh= $\pm 10^{-2}$ A, thus ΔR_{in}= ± 625 mΩ (i.e. ± 2.5 % steady state error of R_{ref}).

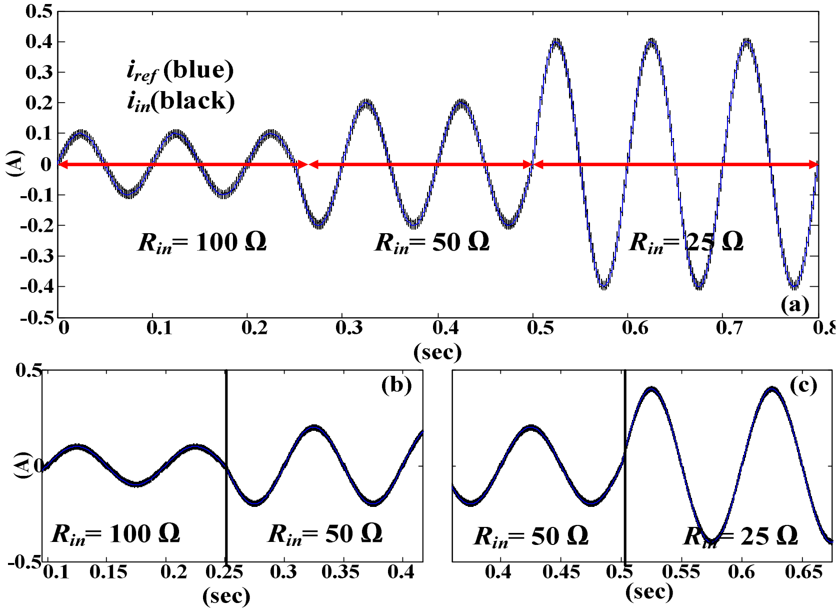

Figure 3-12: (a) Converter i_{in} (black), reference current i_{ref} (blue), (b) Detailed i_{in} and i_{ref} transients indicating 50 % set-point reduction.

Again, the purpose of the SMR is to harvest maximum real power from the line, generated by a suspension generator. In this simulation, assuming v_x is an independent power source, the lower value of R_{in} should correlate to higher power of battery storage. Hence, as indicated by Figure 3-13, the rectified battery current i_{DC} should increase as R_{in} decreases to indicate high instantaneous power charging. To evaluate the bi-directional power flow of the SMR, similar sweep of synthesized resistors is implemented. In this case, R_{in} is swept from 100 Ω to -50 Ω and -50 Ω to 25 Ω. As shown in Figure 3-14, when R_{in} = -50 Ω the direction of i_{DC} is opposite (negative) comparing to that of R_{in} = 100 Ω and 25 Ω. This indicates the converter is placed in motoring mode, meaning the instantaneous power is drawn from the DC link to AC line. This is an invaluable feature of the controlled SMR for applications in suspension regenerative semi-active control schemes, which will be outlined in Chapter 3. Moreover, from Section 2.2, in the mechanical domain, this indicates the synthesis of negative damping coefficient c_e= $0.02k_e k_t k_g^2 d^{-2}$.

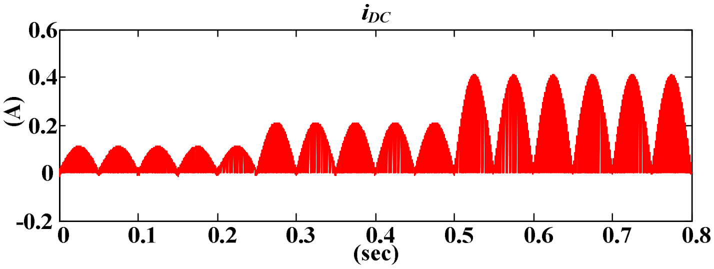

Figure 3-13: DC link charged current for R_{in} sweep.

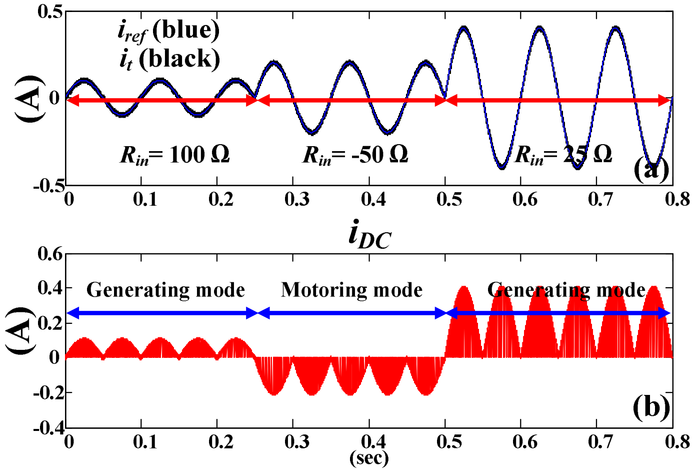

Figure 3-14: (a) Converter i_t (black), reference current i_{ref} (blue). (b) DC link current indicating transition between generating and motoring mode.

3.3.2. Multi- level Hysteresis Current Control

The aforementioned 3- level HCC can be readily expanded to multi-level modulation schemes. To demonstrate the expandability of HCC, a 5- level HCC cascaded H- bridge has been simulated in MATLAB/ SIMULINK/SymPowerSystem. It is worthy to mention that comparing to DB- HCC the benefits of this strategy, in high- power level applications, is to provide lower MOSFET switching frequency (lower switching loss), EMI, and inverter THD. The apparent drawbacks are larger conduction loss (due to addition MOSFET $R_{DS(on)}$), converter, and auxiliary circuit footprints [89]- [93]. During regular conduction modes, the conduction loss is doubled for a 5-level cascaded H- bridge SMR topology comparing to that of a 3-level SMR.

Before illustrating the control algorithm, it is important to mention that, in this work, with lower power-levels (< 5 W), the apparent drawbacks of the cascaded topology (i.e. increased conduction loss, larger converter foot- print) exceed the potential benefits (i.e. EMI, THD reductions) due to low DC bus voltages. Due to this reason, the prototype of the 5- level SMR was not fabricated.

As depicted in Figure 3-15, the 5- level SMR topology is synonymous to that of a 3- level SMR with an additional H- bridge. It is worthwhile to note the double- band type HCC control algorithm is an expansion to that of a 3- level control law (see Figure 3-9). Since, a single- bridge topology can only generate 3 voltage levels (i.e. -v_{DC}, 0, v_{DC}). As a result, the state machines of 3-level HCC have to be expanded. Referring to Figure 3-16, there are 5 states exist in a 5- level HCC state machine. With the states transitioning to the other represents the voltage change generated by the cascaded topology.

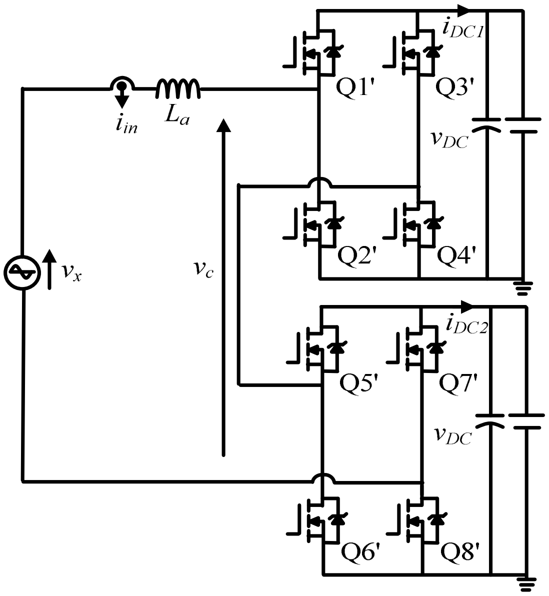

Figure 3-15: Five- level cascaded H- bridge SMR.

To illustrate the 5- level state diagram (see Figure 3-16 and Table 3-1), a nominal start point in Mode 2 (v_{DC}= 0 V) can be chosen. The transition between Mode 2 (v_{DC}= 0 V), 3 (v_{DC}= V_{DC} V), and 1 (v_{DC}= -V_{DC} V) will take place as long as the converter current i_{in} is regulated within the smaller error-band (defined by ΔI_s). Once, ΔI_s losts regulation due to external state perturbation (e.g. line voltage or desired synthesized resistor change) the state transition to Mode 0/4 takes place. The on/off states for all MOSFETs for different levels of v_{DC} are tabulated in Table 3-1. Various works have been devoted to optimize the switching sequence for minimizing the numbers of MOSFETs turning on/off to alternate between desired v_{DC} [89], [95]-[98]. Assuming due to line voltage variation or amplitude of desired converter current, applying v_{DC}= ± V_{DC} V is unable to regulate i_{in} within ΔI_s, the transition between Mode 3/4 or 0/1 will take place (i.e. v_{DC}= ± V_{DC}, ± 2V_{DC}). For illustrative purpose, the bi- directional 5- level SMR is simulated in MATLAB/SIMULINK/ SymPowerSystems with v_x= 15 $sin(20\pi t)$, L_a= 10 mH (ESR= 1Ω), and v_{DC}= 12 V, R_{in}= 10 Ω for 0.6 (sec) with 50 % change of R_{in} at ≈0.32 (sec). The error- bands selected are ΔI_s= 0.01 (A) and ΔI= 0.02 (A).

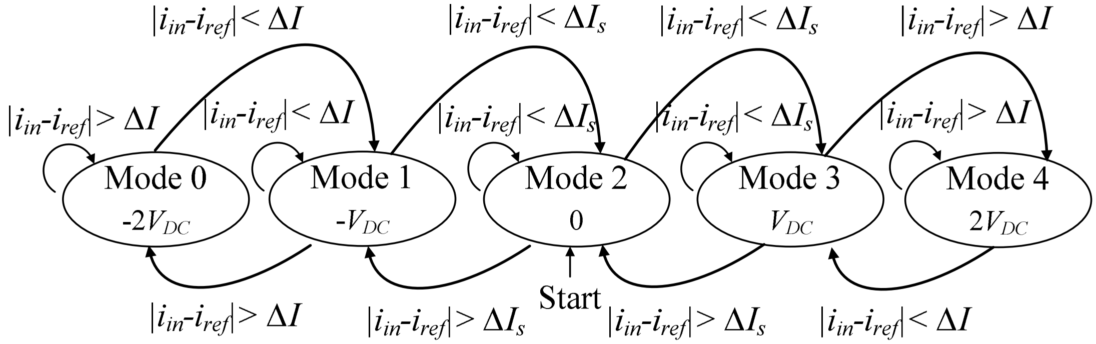

Figure 3-16: Five level HCC state diagram. The error- bands are defined by both ΔI and ΔI_s.

Table 3-1: Truth table of 5- level HCC switching combinations

Q1/ not (Q2)	Q3/ not (Q4)	Q5/ not (Q6)	Q7/ not (Q8)	v_c	Q1/ not (Q2)	Q3/ not (Q4)	Q5/ not (Q6)	Q7/ not (Q8)	v_c
0	0	0	0	0	1	0	0	0	V_{DC}
0	0	0	1	-V_{DC}	1	0	0	1	0
0	0	1	0	V_{DC}	1	0	1	0	2V_{DC}
0	0	1	1	0	1	0	1	1	V_{DC}
0	1	0	0	-V_{DC}	1	1	0	0	0
0	1	0	1	-2V_{DC}	1	1	0	1	-V_{DC}
0	1	1	0	0	1	1	1	0	V_{DC}
0	1	1	1	-V_{DC}	1	1	1	1	0

As depicted in Figure 3-17, the line voltage v_x, in Figure 3-17 (a), is assumed an independent AC voltage source. The converter current i_{in}, in Figure 3-17 (b), varies corresponding to the desired R_{in}. The error current $i_{err}= i_{ref} -i_{in}$ and controlled cascaded H- bridge voltage are shown in Figure 3-17 (c) and (d), respectively. To observe the state transition, a detailed depiction of the waveforms is placed in Figure 3-18. As shown in Figure 3-18 (d) the state transition takes place from Mode 2 to 4 due to the lost regulation of ΔI_s. According to (3-3)- (3-4), since the maximum voltage (at 100% duty cycle) can be generated by a single H- bridge is $v_c= V_{DC}$, therefore, when the voltage level is incapable of regulating the reference current i_{ref} (for synthesizing R_{in}) the transition will take place in the larger error-band. The larger error- band is defined by ΔI.

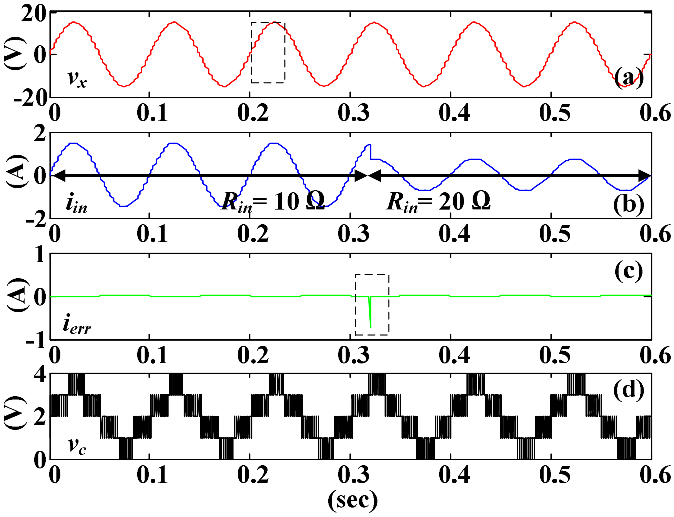

Figure 3-17: (a) Line voltage, (b) converter current, (c) error current, and (d) inverter generated voltage. v_x= 15 $sin(20\pi t)$ and v_{DC}= 12 V.

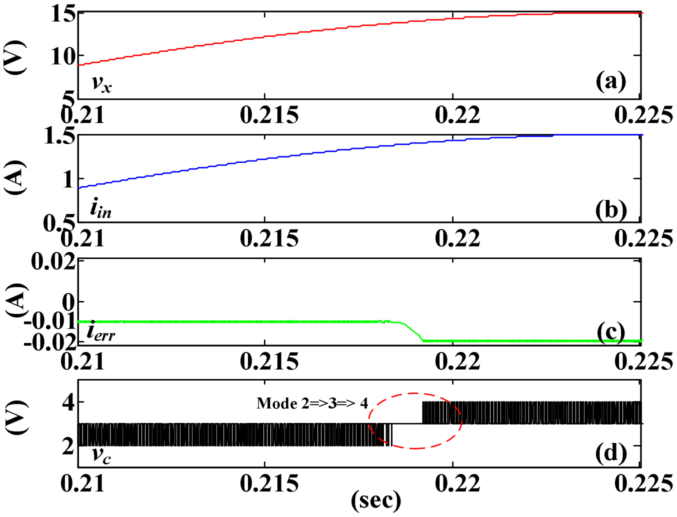

Figure 3-18: Detailed (a) line voltage, (b) converter current, (c) error current, and (d) inverter generated voltage indicating transition of modes due to smaller error-band lost of regulation.

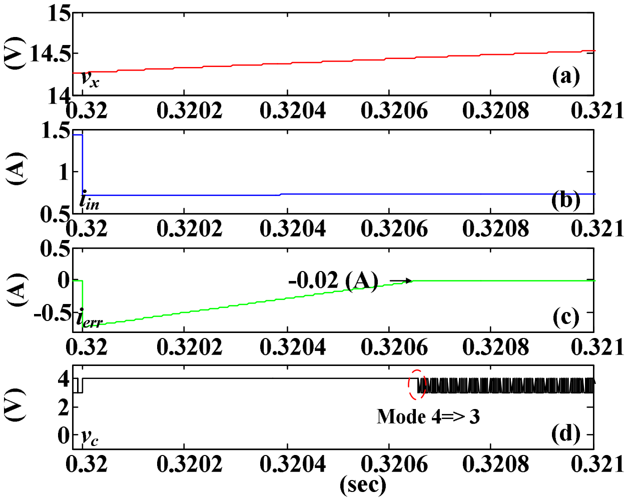

Figure 3-19: Detailed (a) line voltage, (b) converter current, (c) error current, and (d) inverter generated voltage indicating controller reducing i_{err} for 50% input change.

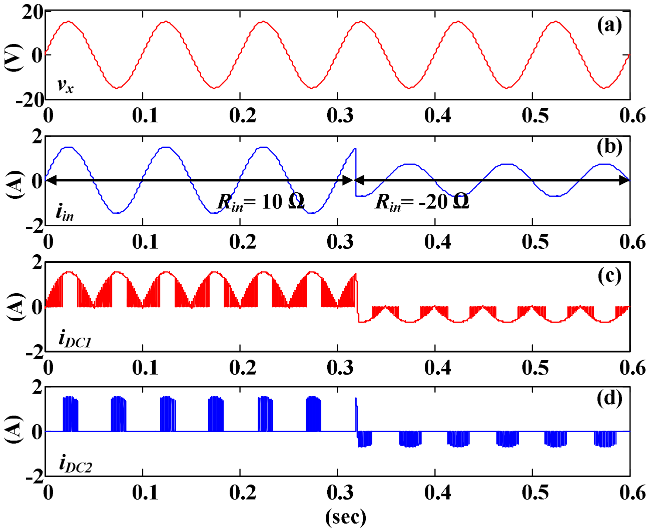

Figure 3-20: (a) Line voltage, (b) converter current, rectified current of (c) first bridge, and (d) second bridge indicating bi- directional power flow.

The transient response of the 50% R_{in} change is delineated in Figure 3-19. As indicated, during the transients, in the positive line cycle the state with the highest voltage level (i.e. Mode 4) is turned on with $\frac{di_{in}}{dt} = L_a^{-1}\left(2V_{DC} - v_{in}\right)$, in order for the DC link to rapidly reduce i_{err} to the its' previous state (i.e. Mode 3). In this simulation, the time requires transitioning back to Mode 3 is 0.6× 10^{-3} (sec). This implies that with more levels of inverter voltages this time interval can be further reduced.

To demonstrate the bi- directional power flow, a similar simulation is shown with polarity change of R_{in}. In this case, R_{in} is varied from 10 Ω to -20 Ω at 0.32 (sec). To observe the power flow the rectified current of both bridges are shown in Figure 3-20. It is demonstrated with R_{in}>0 Ω the power flows from line to DC link and when R_{in}>0 Ω the opposite flow of power will take place. In addition, from the state machine (in Figure 3-16), Figure 3-20 (c), and (d) it is realized when the transition takes place in larger error-band the bridge assigned to the smaller-error band is always turned on (by Q1'/4' or Q2'/3').

3.3.3. Proportional Integral/ State Space Feedback Control of Switch Mode Rectifier for Variable Resistor Synthesis

Other than hysteresis current control (HCC), outlined in the earlier, for controlling the SMR for resistor synthesis, another control scheme introduced for the same objective is a proportional integral (PI)/ state- space feedback typed controller. Before calculating for the PI-controller gains we analyze the expression of the terminal impedance (i.e. resistor). In the PI-based controller scheme, the possibility of synthesizing variable resistor is outlined in the following. The simplified SMR model is shown in Figure 3-21. Again, the model is essentially consisted of a fixed inductor with a single phase voltage source inverter. Based on the desired terminal impedance the state-space feedback controller minimizes the difference between reference and terminal current (i.e. i_{ref}-i_t) by generating the corresponding v_i through PWM signals. After the low pass filter (i.e. L_f and C_f), one will obtain the desired filtered voltage v_c at source frequency, since the capacitor C_f represents an AC short for the switching ripples. Therefore, the desired phase relationship between line voltage v_t and current i_t can be ensured minimizing errors between i_{ref} and i_t.

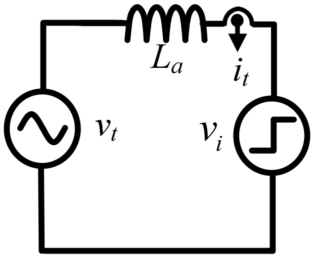

(a)

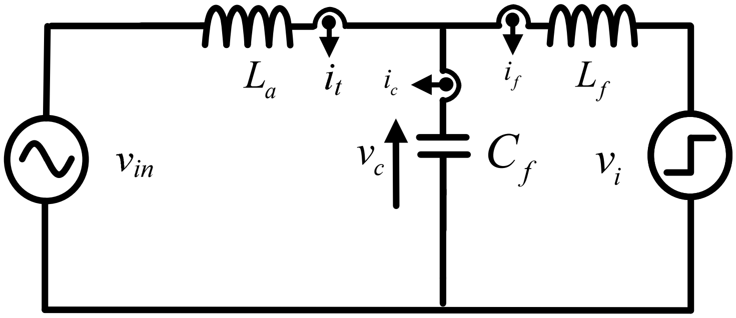

(b)

Figure 3-21: Simplified model of SMR (a) without and (b) with low pass filter driven by ideal voltage source (i.e. R_{int}= 0 Ω).

Referring to the SMR Figure 3-21 (b) and apply Kirchhoff's voltage law (KVL) to v_t one will obtain the following,

$$-v_t + \left(sL_o + R_L\right) i_t + \left(sL_f + R_f\right) i_f - v_i = 0 \tag{3-10}$$

By controlling the desired synthesized resistor R_{in}, the inverter voltage v_i which includes the controlled error current (i.e. i_{ref}- i_t), as well as the state variables (e.g. v_c) are written as follows

$$v_i = \left(i_{ref} - i_t\right)\left(K_p + s^{-1} K_i\right) + k_{if} i_f + k_{it} i_t + k_{vc} v_c \tag{3-11}$$

where $i_{ref} = v_{in} R_{in}^{-1}$. The proportional and integral gains for PI controller are indicated by K_p and K_i, respectively. The state variable gains for i_f, i_t, and v_c are k_{if}, k_{it}, and k_{vc}, respectively. The voltage generated by VSI is indicated by v_i. The voltage across C_f is denoted by v_c. To remove switching ripples appear on terminal voltage v_t and current i_t, the converter model is modified by adding a low pass filter. The value of the low pass filter can be chosen based on the following. To short circuit the high frequency components C_f is chosen at switching frequency f_{sw}, Z_c approximates low impedance and at source frequency f_s, Z_c approximates high impedance. The value of L_f is chosen that at switching frequency, Z_L approximates high impedance and at source frequency, Z_L approximates low impedance. Following Kirchhoff's current law (KCL) about the low pass filter one will obtain the following

$$i_f = i_t - i_c = i_t - sC_f v_c \tag{3-12}$$

$$v_c = \left(v_t - i_t (sL_o + R_L)\right) sC_f^{-1} \left(sC_f^{-1} + R\right)^{-1} \tag{3-13}$$

Assuming all passive elements are ideals (i.e. equivalent series resistances = 0 Ω), the control law (PI with state feedback). Substituting (3-11) - (3-13) into (3-10) will lead to the following

$$\left(-v_t+\left(sL_o+R_o\right)i_t+\left(sL_f+R_f\right)i_f\right)-\left(\frac{v_t}{R_{in}}K_p+\frac{v_t}{sR_{in}}K_i-K_p i_t-\frac{K_i}{s}i_t\right)$$
$$-k_{if}\left(i_t-sC_f\left(v_t-i_t(sL_o+R_o)\right)\right)-k_{it}i_t-k_{vc}\left(v_t-i_t(sL_o+R_o)\right)=0 \tag{3-14}$$

.

Rearrange (3-14) for v_t and i_t, the synthesized resistor R_{in} in Laplace domain is derived as

$$\frac{v_t(s)}{i_t(s)}=R_{in}\frac{\left(L_oL_fC_fs^4-k_{if}C_fL_os^3+\left(L_o+L_f+k_{vc}L_o\right)s^2+\left(K_p-k_{if}-k_{it}\right)s+K_i\right)}{s^4L_fC_f-s^3k_{if}C_f+s^2\left(k_{vc}+1\right)+\frac{K_p}{R_{in}}s+\frac{K_i}{R_{in}}} \tag{3-15}$$

Having the transfer function we can choose the gain of the state variables and the PI controller. In order to satisfy the stability requirement all the real parts of the poles/zeros have to be negative.

Terminal Transfer Function

In order to vary the desired nominal R_{in} (e.g. 10 Ω) the bode plot of transfer function in (3-15) is generated. Substituting the values of passive elements and controller gains, tabulated in Table 3-2, into (3-15) will result in the following

$$\begin{aligned}R_{in}&=\frac{v_t(s)}{i_t(s)}\\&=\frac{5\times10^{-12}\ s^4+1.95\times10^{-13}\ s^3+0.002\ s^2+3.87\times10^{5}\ s+5000}{5\times10^{-9}\ s^4+1.95\times10^{-10}\ s^3+s^2+38700\ s+500}.\end{aligned} \tag{3-16}$$

The bode-plot of (3-16) is delineated in Figure 3-22. It is noted with tuning of controller gains (trial/ error) the synthesized resistor transfer function is in agreement with that of a physical R_{in} (i.e. 10 Ω) in the frequency range of interest (i.e. 1 Hz to < 20 Hz), which demonstrated the PI/ state- space feedback controlled SMR is able to synthesize the desired R_{in} within a certain range of source frequency.

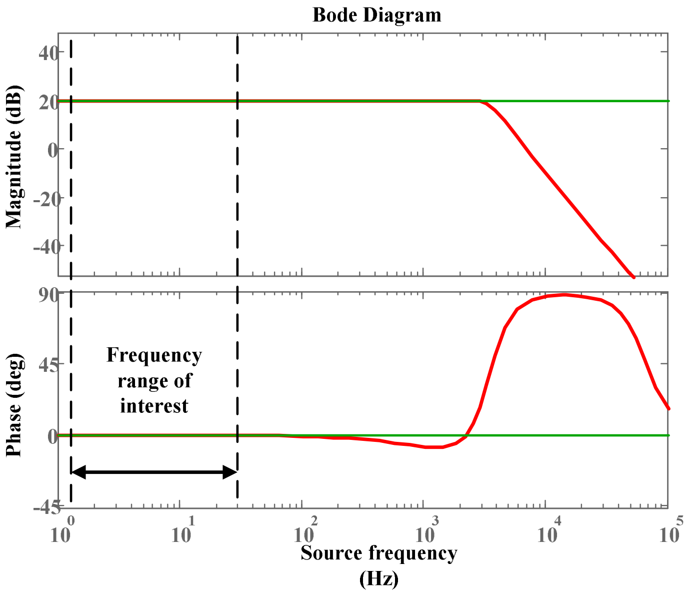

Figure 3-22: Desired synthesized resistor R_{in}= 10 Ω (green) and terminal transfer function (red).

Table 3-2: Values of ontroller gains and passive elements

Parameters	Value	Parameters	Value
L_f	1 mH	K_i	5×10^3
L_o	1 mH	K_{if}	-3.9×10^{-5}
C_f	50 uF	K_{it}	2×10^{-5}
K_p	3.87×10^5	K_{vc}	1.27×10^{-5}
R_{in}	10 Ω		

3.4. Switch Mode Rectifier Prototype

To verify resistor synthesis by the proposed converter prototype, shown in Figure 3-23 (a), a 1- DOF regenerative suspension fabricated by Intelligent Vehicles Lab at Simon Fraser University, as depicted in Figure 3-23 (b) is utilized. Recall Section 2.2.1, the vibrational test-bed setup was developed to provide experimental verification of equivalent damping synthesis provided by the bi-directional bridgeless AC/DC converter, as depicted in Figure 3-23 (c). The electromagnetic- based suspension generates available AC power when placed under base excitation. A two- layered double- sided printed circuit board prototype of the bridgeless AC/DC converter is depicted in Figure 3-23(a). The layout enables the converter to be either externally powered by a DC power supply or internally by the load connected Sealed Lead Acid battery. In addition, surface-mount ferrite beads were placed for proper grounding between power and signal. Other components adopted are tabulated in Table 3-3. To balance the tradeoff between MOSFET on- state resistance and gate charge. Considering the general figure of merit $R_{,DS(ON)} \times Q_g$, n-MOSFETS IRFZ44N by International Rectifier were selected.

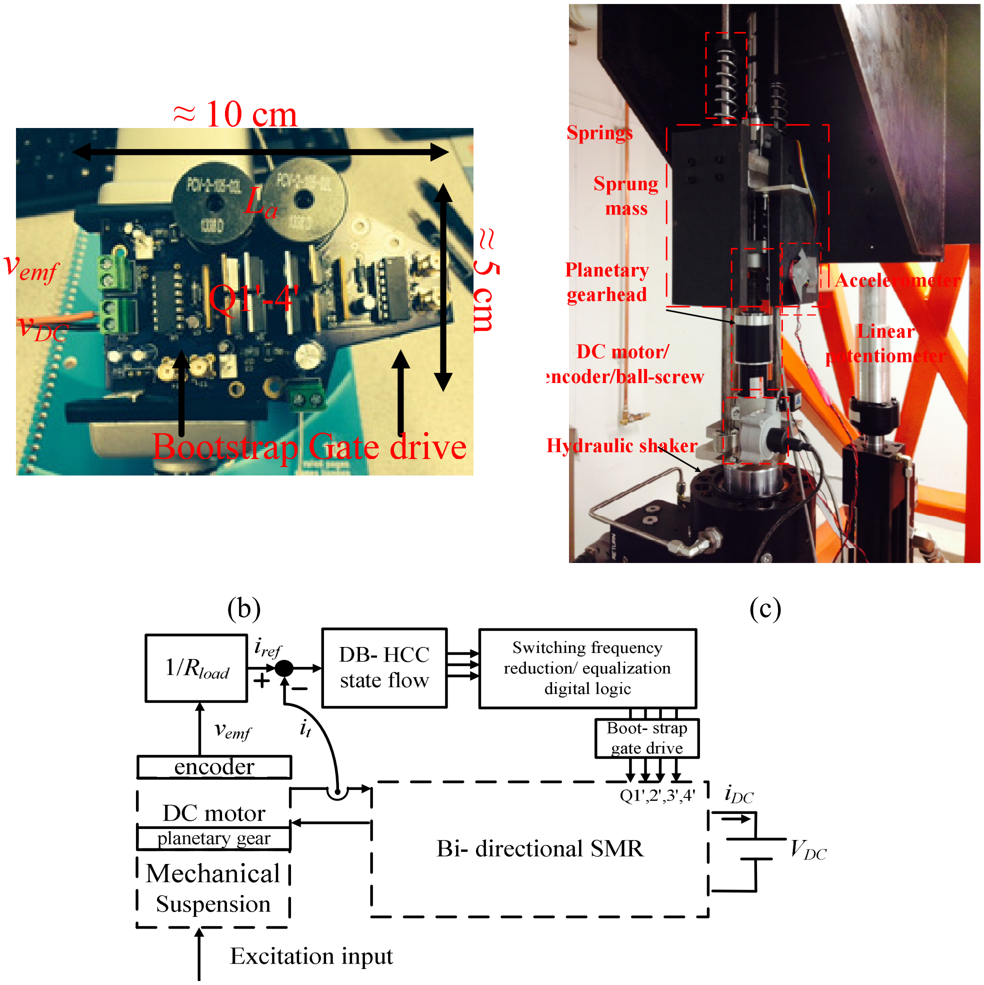

(b) (c)

(d)

Figure 3-23: (a) PCB prototyped bi-directional bridgeless AC/DC converter. (b) Regenerative automotive suspension prototype. (c) Test bed setup for variable resistor synthesis.

Table 3-3. Power components selected for switching waveform and power efficiency simulation.

Component	Manufacture	Part number
n- MOSFET	International Rectifier	IRFZ44N

Component	Manufacture	Part number
Power Inductor	Coilcraft	PCV- 2- 105- 02L
Electrolytic Capacitor	Nichicon	UVR1J682MRD
Floating Gate drive	International Rectifier	IR 2110
Seal Lead- acid Battery	Infinity Battery	I232/ IT 1.3- 12

3.5. Experimental Variable Resistor Synthesis under Suspension Harmonic Excitations

In order to demonstrate resistor synthesis, the SMR was swept from minimum to maximum resistances of R_{in}= 10 Ω to 100 Ω for a nominal of 20 (sec) duration at a fixed vibration amplitude of Y=5 mm and frequency of f= 5 Hz as shown in Figure 3-24 (a). As depicted in in Figure 3-24 (b), the regenerative mechanism (i.e. ball-screw/ DC machine) presents nonlinearity through EMF v_{emf} when over-damped with R_{in} = 10 Ω. Recalling Table 2-4, the damping coefficients are swept from 2.3 kNs/m to 420 Ns/m. The detailed instantaneous waveforms v_{emf} and i_{in}, depicted in Figure 3-24 (b) to (d), indicates not only high power factor but also the variation of desired R_{in} through their corresponding amplitude ratios. In addition, since v_{emf} is a controlled voltage source (VCVS), it means that varying values of R_{in} leads to amplitude change of v_{emf} (through relative velocity), which indicates the change of sprung mass dynamic.

To demonstrate variations of the suspension dynamic with respect to variations of R_{in} the suspension relative displacement is depicted in Figure 3-25. Again, since increasing R_{in} corresponds to reducing equivalent damping force. As a result, the suspension relative displacement increases.

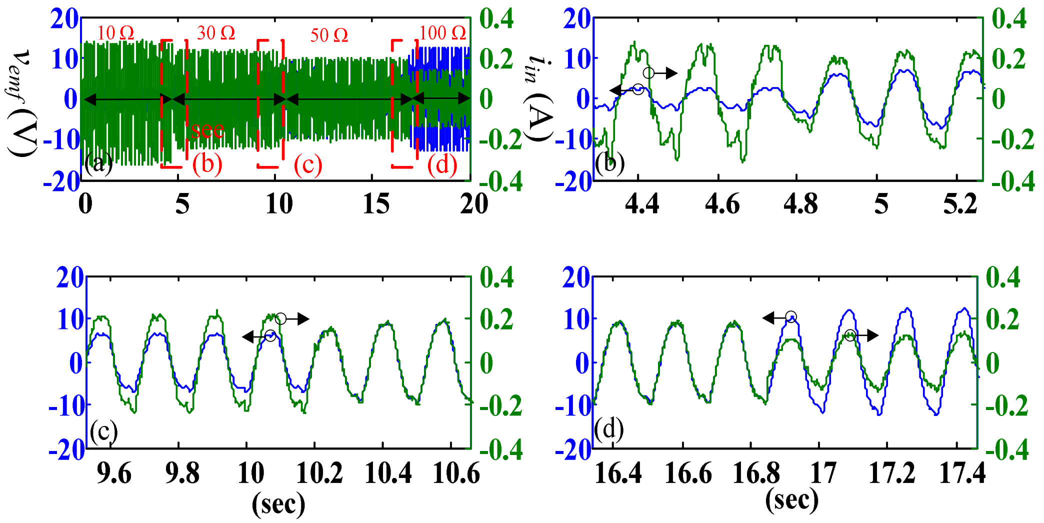

Figure 3-24: (a) Desired resistor synthesis sweep from R_{in}= 10 to 100 Ω. (b) Detailed instantaneous R_{in} variation from R_{in}= 10 to 30 Ω, (c) 30 to 50 Ω and (d) 50 to 100 Ω at fixed vibration amplitude of Y=5 mm and frequency of f= 5 Hz.

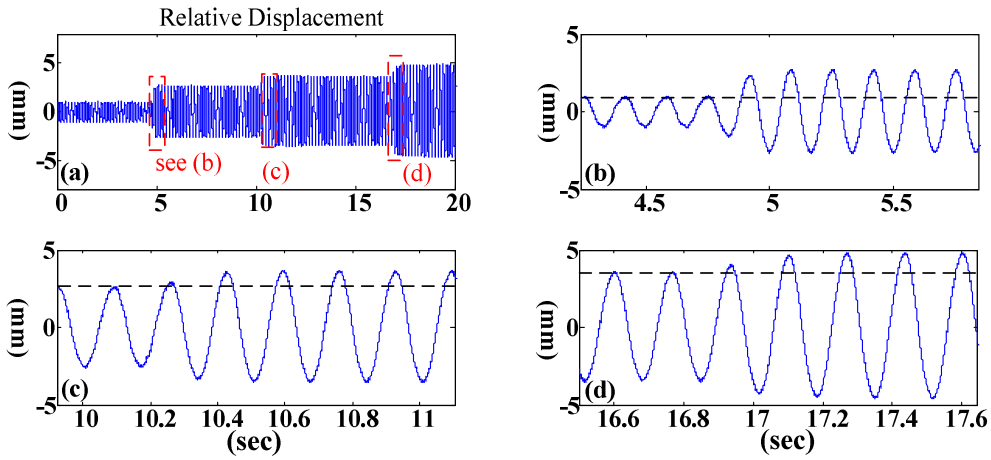

Figure 3-25: (a) Variation of suspension relative displacement as a result of desired resistor synthesis sweep. Detailed instantaneous relative displacement variation from (b) R_{in}= 10 to 30 Ω, (c) 30 to 50 Ω and (d) 50 to 100 Ω.

3.6. Vibrational Frequency Sweep with Fixed Excitation Amplitude and Synthesized Resistance

3.6.1. Regeneration Mode

In this case, the synthesized resistor R_{in} is arbitrarily chosen as 10 Ω. Referring to Figure 3-26 the suspension prototype is excited from 5 to 10 Hz incrementing at the rate of 0.1 (Hz/sec) for 50 (sec). It should be noted that the swept-sine excitation incrementally sweeps the single-tone input frequency (applied to the base excited suspension system). For this type of experiment, a nominal stop frequency, which indicates the end of single-tone sweep, has to be selected. Assuming the wavelength of an ideal sinusoidal road profile is 2.5 (m), thus the range of 5 to 10 Hz excitation frequencies corresponds to vehicle travelling at 45 to 90 km/hr.

Referring to Figure 3-26 (b) and (c), over the frequency of interest, average input current $i_{in,avg}$ is observed to be in- phase (i.e. high power factor, PF≈ 1) with v_{in} while maintaining the corresponding amplitude ratio. Thus, the converter is able to provide desired damping in the electrical domain by harvesting real power from the regenerative vehicle suspension, which is in the mechanical domain. In this experiment, the average power regenerated over f_i= 5- 10 Hz in 50 (sec) duration are calculated as 1.73 Watts.

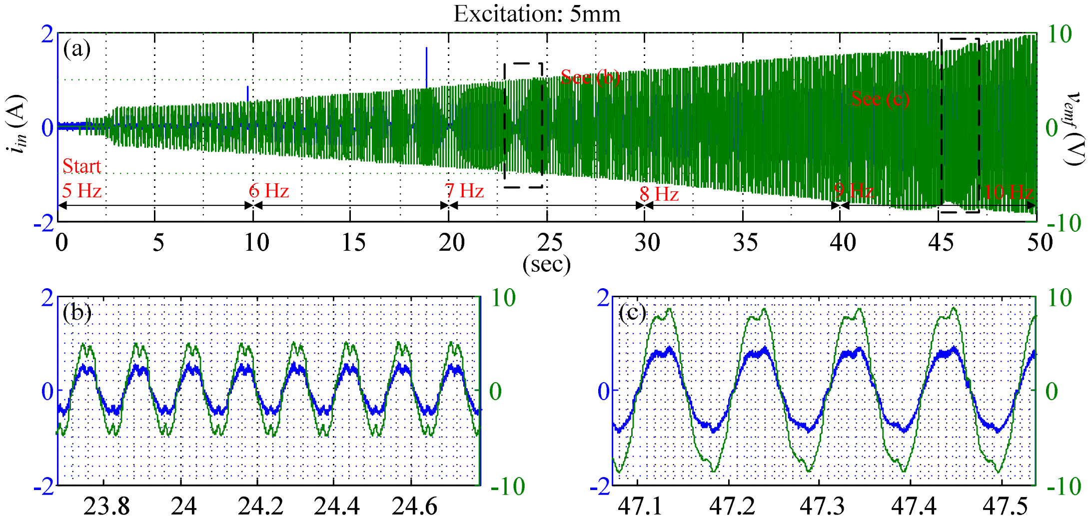

Figure 3-26: (a) Motor back EMF and current waveforms synthesizing R_{in}= 10 Ω by sweeping excitation frequencies from 5 to 10 Hz in 50 seconds (i.e. 0.1 Hz/ sec) with 5mm excitation amplitude. (b) Detailed instantaneous waveform indicating R_{in}= 10 Ω at vibration frequency ≈ 7.4 Hz and (c) ≈ 9.7 Hz.

3.6.2. Motoring Mode

While the SMR is operating in motoring mode, it synthesizes negative resistor ($R_{in} < 0$ Ω). Again, operations in motoring mode require draining of battery energy. This corresponds to the generation of negative damping in the electrical domain of the suspension system. In this case, R_{in} is arbitrarily chosen as -100 Ω. Referring to Figure 3-27 (a) to (c), over the frequency of interest, the average input current $i_{in,avg}$ is observed to be out of phase (i.e. PF≈ -1) with v_{in} while maintaining the corresponding amplitude ratio. In addition, to observe battery drainage, the battery current i_{DC} is also depicted along with EMF voltage v_{emf} and converter current i_{in}. As seen in Figure 3-28 (a) at roughly 2.5 (sec), the base initiates ground vibration at approximately 2.5 (Hz) and 5mm, the converter current is controlled to suffice R_{in}= -100 Ω with respect to EMF voltage. At this time, the negative battery current clearly starts, which indicates drainage.

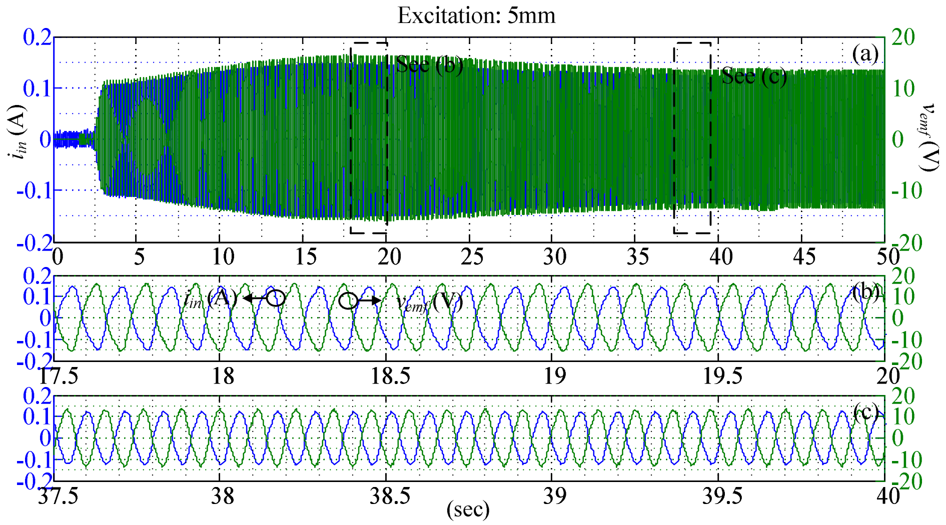

Figure 3-27: (a) Motor back EMF and current waveforms synthesizing R_{in}= -100 Ω by sweeping excitation frequencies from 5 to 10 Hz in 50 seconds (i.e. 0.1 Hz/ sec) with 5mm excitation amplitude. (b) Detailed instantaneous waveform indicating R_{in}= -100 Ω at vibration frequencies ≈ 7 Hz and (c) ≈ 9 Hz.

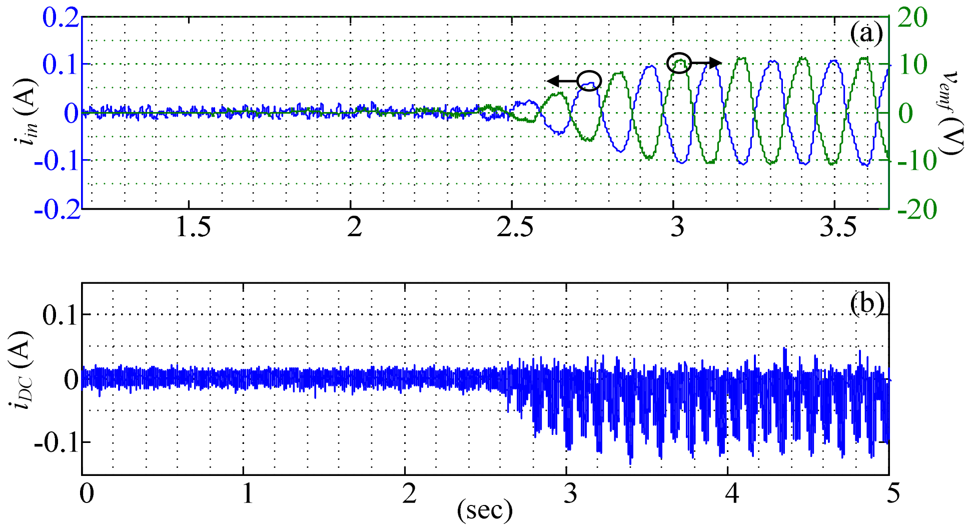

Figure 3-28: (a) Transients of Motor back EMF and current waveforms synthesizing R_{in}= -100 Ω. (b) Negative battery current indicating converter is placed in motoring mode.

3.6.3. Mechatronic System Conversion Efficiency

The power flow of the proposed mechatronic system is displayed in Figure 3-29. The analysis can be divided into mechanical (i.e. road excitation/ suspension system) and electrical domains (i.e. AC/DC converters/ battery packs). The overall efficiency of power regeneration η is defined in (3-17) as the product of mechanical effiency η_m, generator efficiency η_e, and AC/DC rectifier efficiency $\eta_{AC/DC}$

$$\eta = \eta_m \eta_e \eta_{AC/DC} \tag{3-17}$$

where η_{me} is the overall efficiency of the electro- magnetic suspension. The instantaneous power, provided by road force, supplies to the system (P_{all}) is equal to the sum of instantaneous power dissipated by physical friction (P_f), absorbed by the DC machine (P_c), and required to build up sprung-mass oscillation (P_k). This means that, only the power absorbed by the electrical damping contributes to the power regeneration; therefore, the mechanical efficiency can be defined as

$$\eta_m = \frac{P_c}{P_{all}} = \frac{P_c}{P_c + P_f + P_k} \tag{3-18}$$

The instantaneous available power provided by the DC machine represents the total power transferred to the electrical domain is defined as

$$P_c = v_{in}^2 \left(R_{\text{int}} + R_{load}\right)^{-1}. \tag{3-19}$$

The instantaneous harvestable power, which represents the power transferred to the attached power converter, can be written as

$$P_e = P_c R_{load} \left(R_{\text{int}} + R_{load}\right)^{-1}. \tag{3-20}$$

The electrical efficiency η_e degradation by the motor winding and other losses in the AC/DC converter can be derived as

$$\eta_e \approx R_{load} \left(R_{\text{int}} + R_{load}\right)^{-1}. \tag{3-21}$$

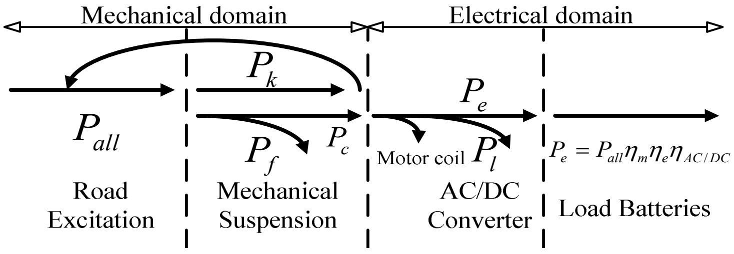

Figure 3-29: Mechatronic systems power flow.

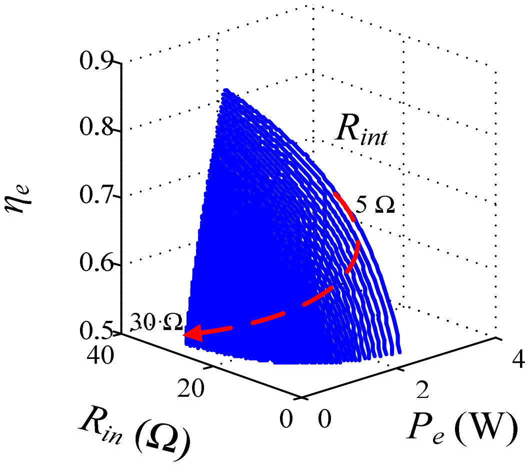

Figure 3-30: Theoretical electrical efficiency η_e and generated (harvestable) power P_e with various DC motor internal resistors R_{int} and synthesized resistors R_{in} assuming EMF voltage equals to 10 $sin(10\pi t)$. Note: The plot only depicted maximum R_{in}= 30 Ω

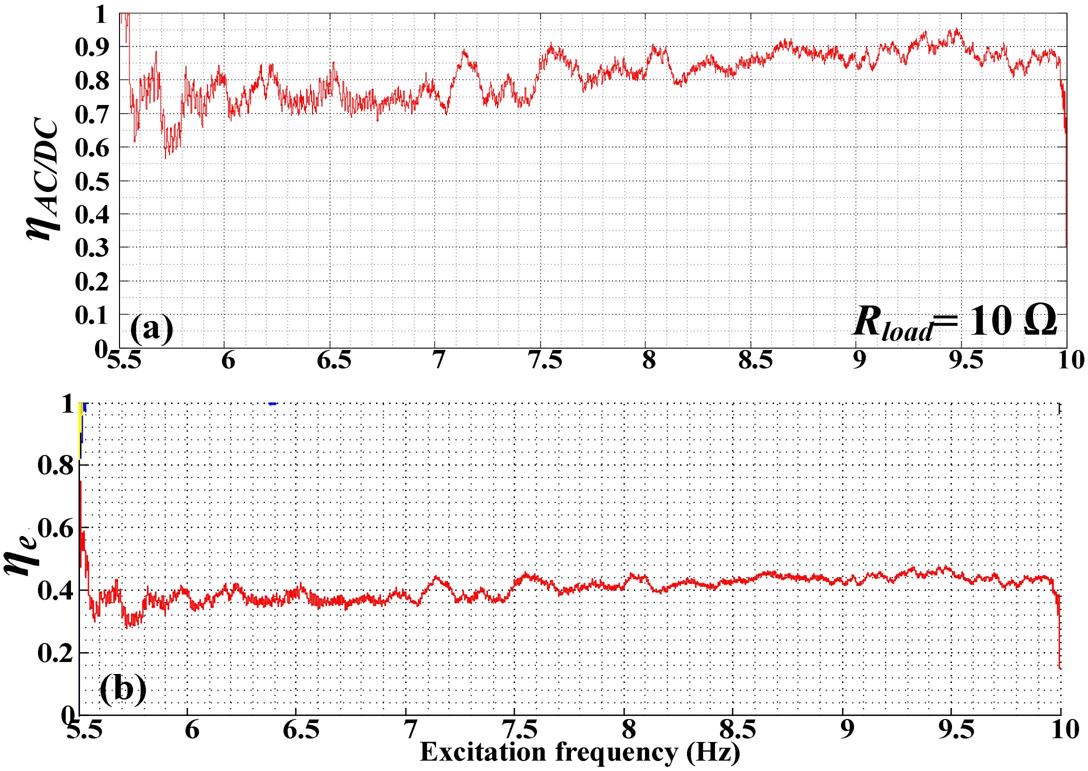

Figure 3-31: Instantaneous (a) SMR power conversion efficiency $\eta_{AC/DC}$ and (b) electrical domain efficiency η_e over the swept frequencies synthesizing R_{in}= 10 Ω.

Referring to Figure 3-30, the nominal P_e and η_e are calculated for every value of R_{int} and R_{in}. Different R_{int} represents power dissipated by different types of DC brushed machine. As indicated, motors with low winding losses (assuming motor coil losses and power losses in the AC/DC converter are lumped together) are preferred for vibrational energy harvesting and variable equivalent damping provision, since assuming equal R_{in}, lower values of R_{int} offers higher P_e and η_e. In other words, highly efficient motors with lower values of R_{int} are able to achieve the same P_e at a higher motor efficiency η_e. To exemplify, the experimental results of $\eta_{AC/DC}$ and η_e are presented. While regeneration from regenerative suspension with R_{in}= 10 Ω the SMR power conversion efficiency $\eta_{AC/DC}$, swept over an extended range of vibrational frequencies, is documented in Figure 3-31 (a). The highest efficiency $\eta_{AC/DC} \approx$ 95% is obtained. In addition, the experimental η_e, over the same range of vibrational frequencies, is shown in Figure 3-31 (b). The highest η_e obtained ≈ 45%, which is expected since the SMR is synthesizing R_{in}= 10 Ω through a DC generator (maxon 218011, Graphite Brushed DC motor and planetary gearhead GP52C 223083) with $R_{int} \approx$ 10 Ω.

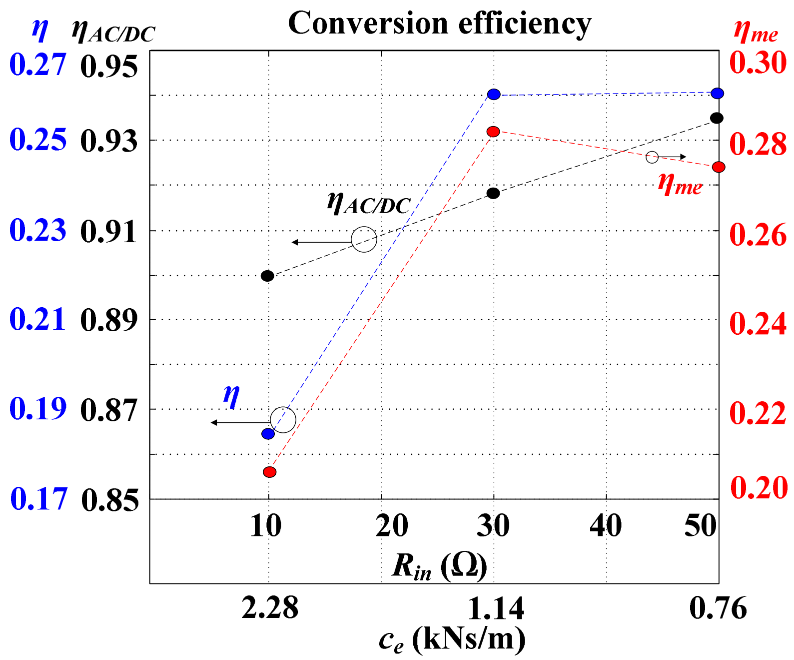

Figure 3-32: Overall experimental efficiencies η and conversion efficiencies of both power converter $\eta_{AC/DC}$ and electromagnetic suspension η_{me} with respect to various synthesized resistances R_{in} and corresponding damping coefficient c_e.

In this work, while regeneration from suspension prototype with various values of R_{in}, conversion efficiencies are obtained as displayed in Figure 3-32. Referring to (3-17) the overall experimental efficiencies obtained for R_{in}= 10, 30, and 50 Ω are $\eta \approx$ 18 %, 25 %, and 25.2 %, respectively.

3.7. Experimental Variable Resistor Synthesis under ISO Standard Excitations

To verify the performance of SMR while placed under ISO road profiles the suspension prototype is exited according to the generated ISO class C and D road profiles as shown in Figure 3-33. As expected, since higher road classes indicate higher PSD, the excitation amplitude across a nominal time range (i.e. 30 seconds) is higher. In order to enlarge the region of resistance synthesis the SMR is swept from minimum to maximum resistances of 10 Ω (damping coefficient c_e= 2.28 kNs/m) to 100 Ω (c_e= 0.41 kNs/m) in 30 (sec) using ISO standard road profile (class C) as shown in Figure 3-34 (a). The detailed instantaneous waveforms of v_x and i_{in} depicted in Figure 3-34 (b) to (e) demonstrate high power factor with the variations of desired R_{in} through corresponding amplitude ratios. For detailed instantaneous performance of the SMR, a video was posted to demonstrate the experimental sweep of the resistor synthesis on dSPACE ControlDesk [85]. Similarly, the resistance sweep is also performed for class D road class as shown in Figure 3-35. Compared to class C the EMF voltage is higher due to larger excitation amplitude (and higher frequency components), which leads to higher converter current (for the same value of synthesized resistor).

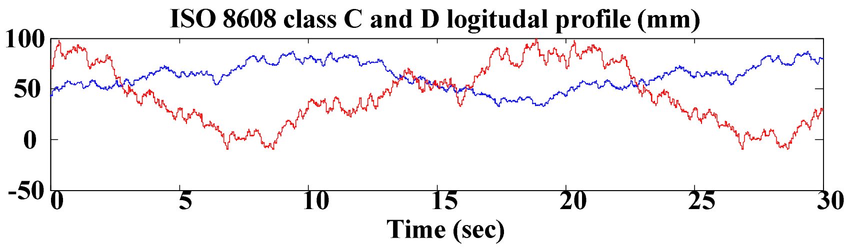

Figure 3-33: ISO 8608 class C (blue) and D (red) excitation profile travelling at 25 km/hr.

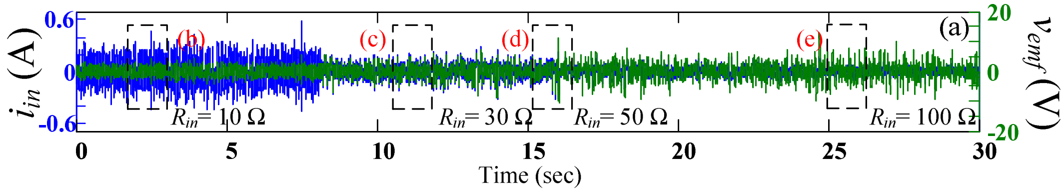

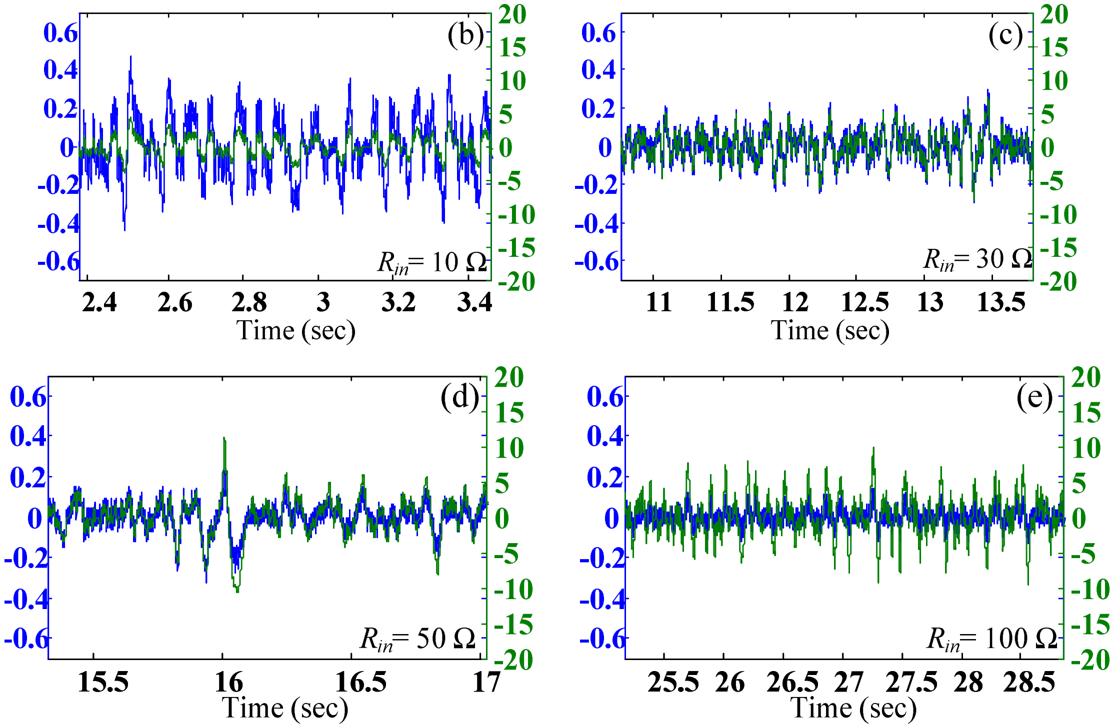

Figure 3-34: (a) Variable resistance sweep from 10 to 100 Ω. (b) Detailed corresponding line current i_{in} and voltage v_{emf} for synthesizing R_{in}= 10 Ω, (c) R_{in}= 30 Ω, (d) R_{in}= 50 Ω, and (e) R_{in}= 100Ω with class C road roughness and vehicle speed = 25 km/hr.

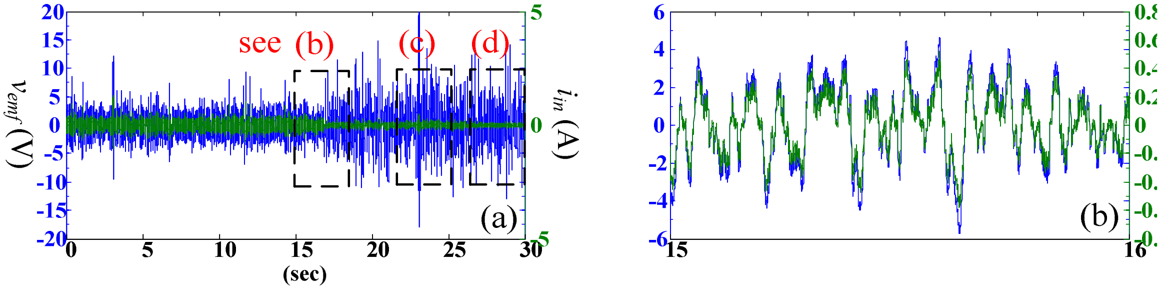

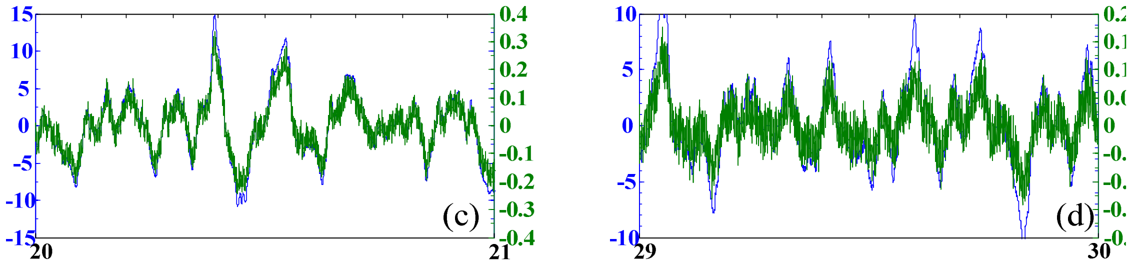

Figure 3-35(a) Variable resistance sweep from 10 to 100 Ω. Detailed corresponding line current i_{in} and voltage vemf for synthesizing (b) R_{in}= 10 Ω, (c) R_{in} = 50 Ω, (d) R_{in} = 100 Ω with class D road roughness and vehicle speed = 25 km/hr.

By referring to Figure 3-36 the detailed inverter voltage v_c and rectified current i_{DC} with respect to EMF voltage and reference converter current is observed. In this case, a nominal R_{in}= 20 Ω is synthesized. As indicated in both Figure 3-9 and Figure 3-16, the switching modes vary from Mode 1- 3 depending on the location of error current i_{err} within the pre-defined error- band.

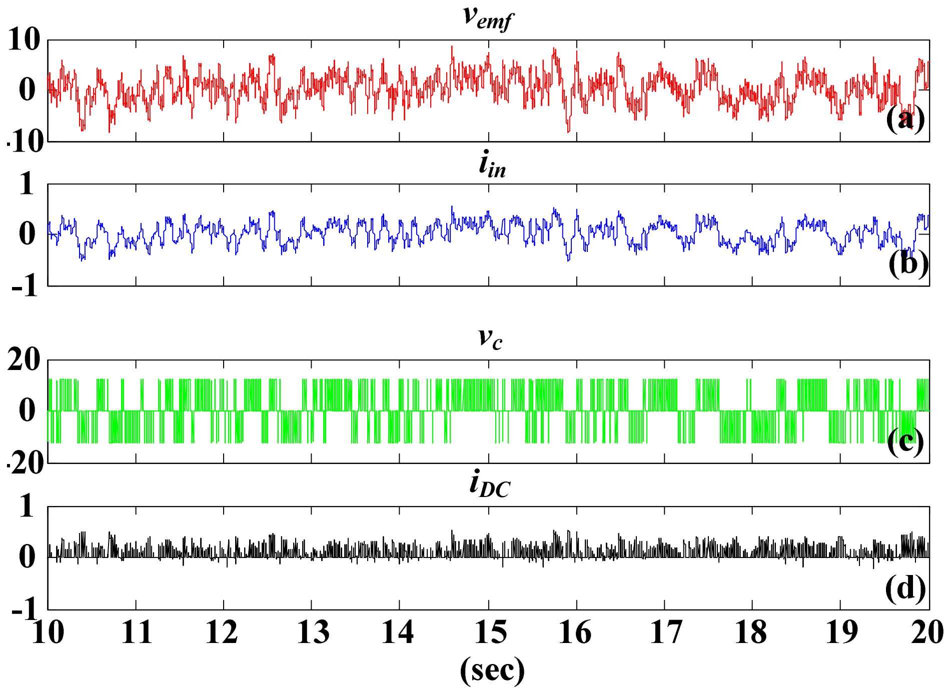

Figure 3-36: (a) Back EMF, (b) converter current for synthesizing R_{in}= 20 Ω, (c) controlled inverter voltage, and (d) harvested current with class D road roughness at vehicle speed = 50 km/hr.

In addition, the SMR also operates in bi- directional power flow. This can be verified by observing inverter voltage v_{DC}, v_{emf}, i_{in}, and rectified current i_{DC} in Figure 3-37. In this work, the transition from regeneration mode to motoring mode takes places at nominal t= 7 (sec) synthesizing R_{in}= 50 Ω to -50 Ω. Referring to both amplitude and phase relationships of v_x and i_{in} the bi- directional power flow of the SMR is verified. This is also confirmed by direction of i_{DC}.

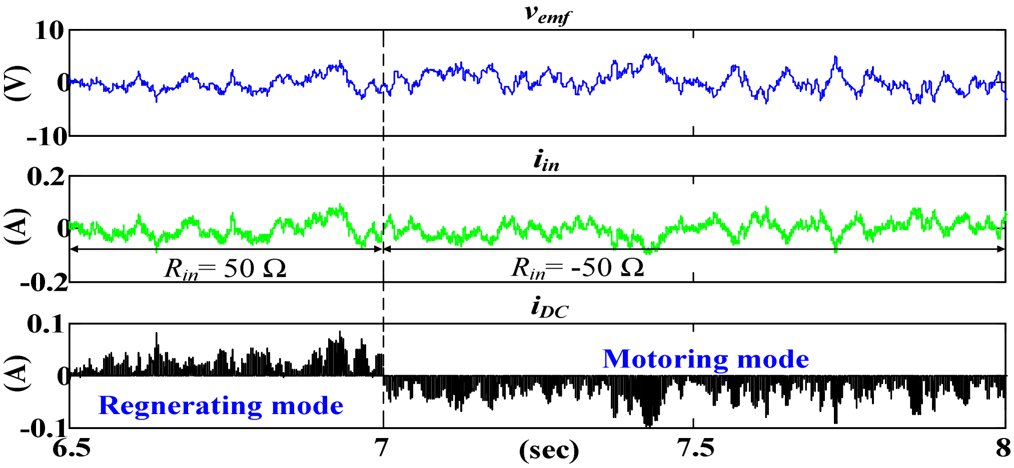

Figure 3-37: Transitioning of bi- directional SMR from regeneration to motoring mode by observing (a) line voltage (b) input current, and (c) rectified current. Note: the nominal start time of 6.5 (sec) is the timestamp of initial real-time data acquisition.

3.7.1. Average Harvested Power/ Energy

To indicate average harvested power similar procedure is utilized, as depicted in Figure 3-38, with R_{in}= 10 Ω, 30 Ω, 50 Ω, and 100 Ω for both cases of ISO 8608 road roughness class C and D (i.e. G_r= 16 and 64 μm^3/ cycle). The instantaneous harvested power P_{in} (z-axis) synthesizing various R_{in} (x axis), captured for 30 (sec) durations (y axis), for both road classes are depicted in Figure 3-38. In order to observe maximum power transfer the averaged P_{in} and total harvested energy (in an hour) are tabulated in Table 3-4 and Table 3-5, respectively. In this case, averaged harvested power $\overline{P}_{in}$ indicates maximum power transfer takes place at R_{in}= 10 Ω, which is approximately the equivalent resistor of the adopted DC machine coil. It is noted, there are tradeoffs between power regeneration and conversion efficiency for various R_{in} under a fixed R_{int}.

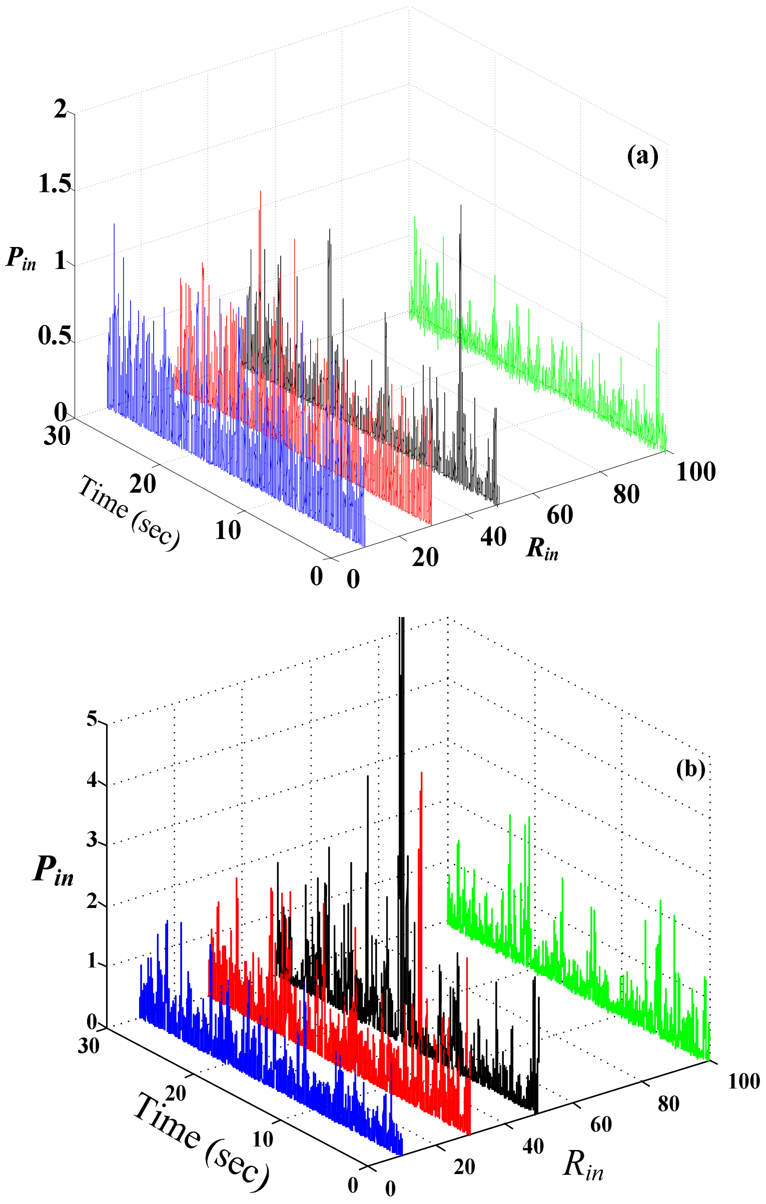

Figure 3-38 Instantaneous power (watts) harvested by actuating Q- car suspension with road roughness of (a) class C and (b) D.

Table 3-4: Average harvested power (mW) various R_{in} under class C and D roughness.

	R_{in}			
Class	10 Ω	30 Ω	50 Ω	100 Ω
C	150	130	65	43
D	400	320	250	147

Table 3-5: Total estimated energy harvested (in Watt- hour) with R_{in} = 10 and 50 Ω under ISO class C and D roughness.

	R_{in}	
Class	10 Ω	50 Ω
C	18	5.1
D	48	30

3.8. Regenerative Semi-Active Control using SMR

In this work, we proposed a mechatronic suspension system with capabilities of energy regeneration and sky-hook (SK) control incorporated into the mechanism [100]. The system overcomes the tradeoffs between energy consumption and ride handling/comfort in an active (semi-active) suspension system. Central to the concept is development of a coupled switched-mode rectifier (SMR) capable of providing either a positive or negative damping ratio by alternating between regenerative and motoring modes. Using the implemented circuit, an active sky-hook control strategy is utilized to offer continuous variable damping force that improves the vibration isolation significantly. Simulation results demonstrated the directions of power flow in both regeneration and motoring modes, through a current controller, to verify performance of the SMR. Experimental results demonstrated both time and frequency response of the regenerative suspension prototype in terms of power regeneration, sprung mass absolute acceleration, and relative displacement. In addition, both theoretical and experimental power conversion efficiencies in various segments of the mechatronic suspension are analyzed and reported.

To this end, various works have proposed semi-active control scheme that can maintain the reliability of passive control using an acceptable amount of energy [101]- [107]. Semi-active control strategies utilizing innovative magnetorheological (MR) fluid damper designs have been proposed by several researchers (see e.g. [101]- [107]). In addition, the R-S control method implemented to minimize the damping force when the spring force and damping force have the same direction is proposed in [108]. The experimental results of three semi-active control methods, (i.e. limited relative displacement, modified R-S, and modified sky-hook) verified in terms of tradeoffs between vehicle handling and passenger comfort, are reported in [109]. Although the "on-off" semi-active methods are efficient in suspension control, they result in uncomfortable jumps when switching between on and off modes. Hence, there would be a sacrifice in the control performance when compared with the continuously variable type. In [110]- [111], a modified Skyhook fuzzy controller in the design of a semi-active suspension system for a Cadillac SRX 2005 is demonstrated with road tests results. Their real-time experiments confirmed that the use of this design method reduces the required time and effort in real industrial problems.

In addition to various approaches of suspension control, power regeneration from vehicle suspension, through an electromagnetic device, has become extremely popular (e.g. [112]-[114]). The common drawbacks of the mechatronic systems discussed previously is the consumption of electrical power (DC current required for MR damper) while generating corresponding forces for purposes of better handling/ comfort. For example, the approach taken in semi- active control implementation in [109] supplied various level of DC current to the MR damper for achieving variable levels of damping forces. On the contrary, the proposed method is capable of selectively apply variable damping forces while regenerate the damped power according to the adopted semi-active control algorithm.

The damping force, with respect to relative velocity $\dot{z}$, for a 1-DOF system with a Skyhook damper can be written as

$$F_{sky} = c_{sky}\dot{z}\,. \tag{3-22}$$

Using a semi-active damper, the Skyhook damping force must be realized in terms of the relative velocity $\dot{z}$. Therefore, the conventional semi-active Skyhook control algorithm is given by [109]-[110]

$$F_{sky} = \begin{cases} c_{sky}\dot{z} \,\middle|\, \dot{x}\dot{z} \geq 0 \\ 0 \,\middle|\, \dot{x}\dot{z} < 0 \end{cases} \tag{3-23}$$

where the presence (on)/ absence (off) of damping force F_{sky} is required according to the signed product of relative and absolute velocity. As for the proposed active Skyhook control strategy, the damper can supply a negative force from a negative damping ratio $-c_{sky}$. In this case, the active Skyhook control algorithm can be written as

$$F_{sky} = \begin{cases} c_{sky}\dot{z} | \dot{x}\dot{z} \geq 0 \\ -c_{sky}\dot{z} | \dot{x}\dot{z} < 0 \end{cases}. \tag{3-24}$$

Recalling (3-24), in order to implement the control algorithm in the electrical- domain, by the SMR, the converter current should be controlled to the following reference current

$$i_{ref} = \left(k_e k_g\right)\left(R_{\text{int}} + R_{load}\right)^{-1} d^{-1}\dot{z} | \dot{x}\dot{z} \geq 0 \tag{3-25}$$

$$i_{ref} = -\left(k_e k_g\right)\left(R_{\text{int}} + R_{load}\right)^{-1} d^{-1}\dot{z} | \dot{x}\dot{z} < 0 . \tag{3-26}$$

$$i_{ref} = 0 | \dot{x}\dot{z} < 0 . \tag{3-27}$$

When $\dot{x}\dot{z} < 0$, i_{ref} is determined by (3-26)- (3-27) for either better vehicle control or power harvesting, respectively. This is due to negative direction of current results in power consumption of the load batteries, by recalling section 3.2. The detailed analysis of the current controller is presented in the following sections.

3.8.1. Simulation Results

The simulation of the regenerative suspension system, connected to SMR, is performed in MATLAB/SIMULINK/Simscape/SymPowerSystem environment. The values of the main parameters for the quarter-car suspension prototype and DC motor (based on maxon 218011, Graphite Brushed DC motor and planetary gearhead GP52C 223083) are the following. m= 5.4 kg, m_a= 0.257 kg, k= 7.3 kN/m, c_f= 100 N- sec/ m, k_e=k_t= 0.1 (V- sec/rad, N- m/A), k_g= 10, J_m= 101e^{-7} kg- m^2, J_a= 1.2e^{-4} kg- m^2 J_g= 9.1e^{-7} kg- m^2, d=l/2π= 0.0095 mm/rev (based on THK ball-screw KX-10), R_s= 10Ω, and L_s= 2.62mH. The values of SMR and DB- HCC are R_a= 1mΩ, L_a= 1mH, V_{DC} = 20 V, small error- band = 0.2 A, and large error- band = 0.3 A.

The simulated waveforms, in Figure 3-39 (a), indicate the behavior of line (EMF) voltage v_{in}, i_{in} and i_{ref} assuming the regenerative suspension is under single-tone harmonic excitation. According to the sky-hook detection outcome, shown in Figure 3-39 (c), SMR presents positive or negative damping according to the polarity of $sign(v_{in}i_{in})$. Moreover, as observed, i_{in} is regulated within the error-band to i_{ref} , which is determined by v_{in} and its polarity varies with respect to the sky-hook detection outcome. Figure 3-39 (b) indicates more detailed current waveforms of i_{in} and i_{ref}. It is observed that before entering the motoring mode, the small-band state loses regulation and returns to the large-band state. Once entered in the motoring mode (i.e. $sign(v_{in}i_{in}) < 0$), both waveforms are out-of-phase with v_{in}. On the contrary, when placed in the regeneration mode, both waveforms are in-phase with v_{in}.

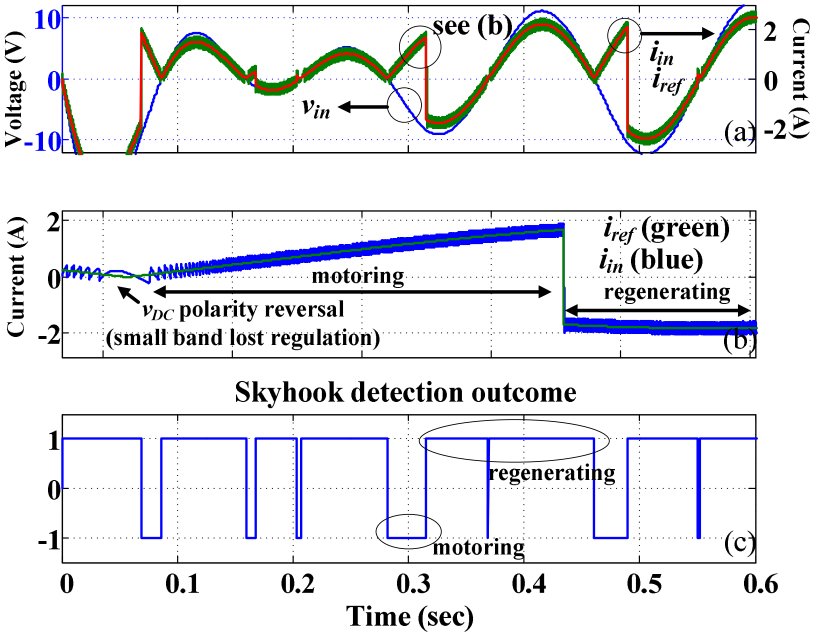

Figure 3-39: (a) Line (EMF) voltage v_{in}, current i_{in}, and reference current i_{ref}. (b) Detailed depiction of i_{in} and i_{ref} indicating motoring and regeneration modes operation, by (c) Sky- hook detection outcome.

To verify the DB-HCC control law state diagram, Figure 3-40 (a) simulates the behavior of i_t and rectified current, which stores energy into the battery. The detailed switching waveforms are shown in Figure 3-40 (b), where the SMR enters the motoring mode from regeneration mode. In this case while operating in regeneration mode, both $sign(v_{in}) > 0$ and $sign(v_{in}i_{in}) > 0$, therefore, SMR alternates between Mode 1 and 2 as shown previously in Figure 3-9. After entering the

Motoring mode, where $sign(v_{in}) < 0$ and $sign(v_{in}i_{in}) < 0$, the alternation between Mode 3 and 4 takes place.

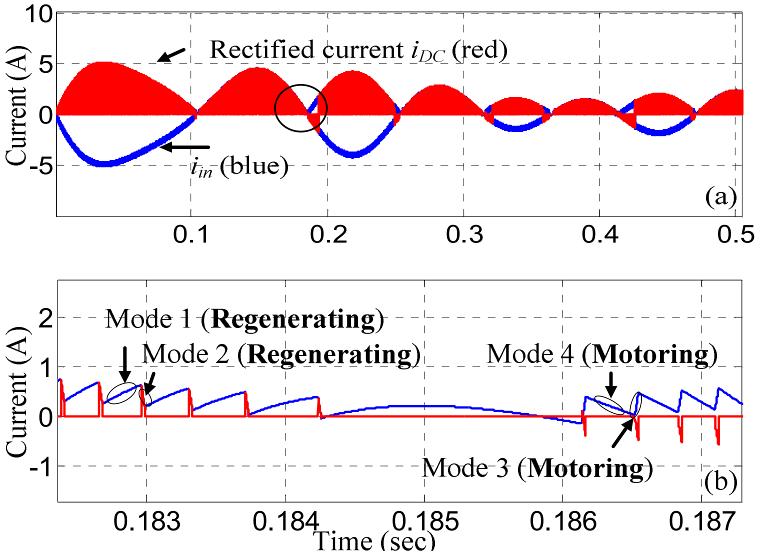

Figure 3-40: (a) Rectified current i_{DC} and line current i_{in} in both motoring and regeneration modes. (b) Corresponding detailed switching waveforms.

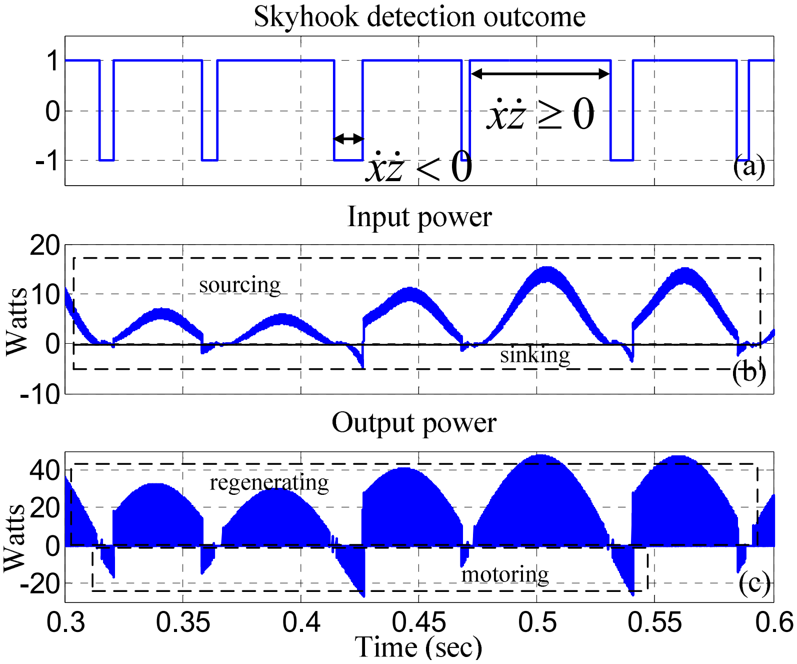

Figure 3-41: (a) Sky-hook detection outcome. (b) Instantaneous input power. (c) Instantaneous output power in motoring and regeneration modes.

According to the sky-hook detection outcome in Figure 3-41 (a), both input and output power shown in Figure 3-41 (b) and Figure 3-41 (c), respectively, indicate regeneration and motoring modes taking place according to their instantaneous polarities. Again, synthesizing negative damping, implies transferring negative source power. Therefore, in the motoring mode the power is transferred from battery to source. Thus, energy harvesting is achieved in regeneration mode, while the stored energy is used to supply the power required in the motoring mode.

3.8.2. Experimental Skyhook Detection

According to the experimental configuration of the mechatronic system, shown in Figure 3-42, the converter prototype is coupled to the 1-DOF base excited regenerative suspension system fabricated by Intelligent Vehicles Lab at Simon Fraser University. As depicted, the source and load of a bi- directional SMR, controlled by double band hysteresis current control (DB-HCC), is coupled to terminals of DC generator/ motor, Graphite Brushed DC motor and planetary gearhead and a rechargeable battery. As previously described in (3-23)- (3-25), since the SK control method requires either presence or absence of damping forces according to the product of absolute and relative sprung mass velocity. Identically, to realize such performance in the electrical domain the connected power converter is required to present constant R_{in}, $-R_{in}$ or “open circuit” (i.e. i_{ref}= 0 A) to the motor terminal. In this work, to maximize power regeneration, the SMR is we designated to only remain in regeneration mode. Meaning, the reference current i_{ref}, derived from motor EMF v_{emf}, switches between i_{ref}= 0 A and $i_{ref}= v_{emf}/(R_{int}+R_{in})$. When $\dot{x}\dot{z} < 0$ (i.e. i_{ref}= 0 A) the power generated by DC generator/ motor is equivalently disconnected to the electrical domain. When $\dot{x}\dot{z} \geq 0$ (i.e. $i_{ref} = v_{emf}/(R_{int}+R_{in})$, since the SMR synthesizes a variable resistor, real power generated by the DC generator/ motor is then harvested into a load battery.

To verify the efficacy of the regenerative Skyhook algorithm, the electromagnetic suspension, shown in Figure 3-43 (a), is placed under swept sine excitation, by a MTS 248 hydraulic actuator, over an extended range of vibrational frequencies. In this work, the suspension is excited from 2- 9 Hz by fixed amplitude of 5mm at the rate of 0.2 (Hz/ sec) for 35 (sec), as depicted in Figure 3-43 (a). The resulting harvested power, sprung mass absolute velocity, and relative velocity for R_{in}= 10 Ω are demonstrated in Figure 3-43 (b) and (c), respectively.

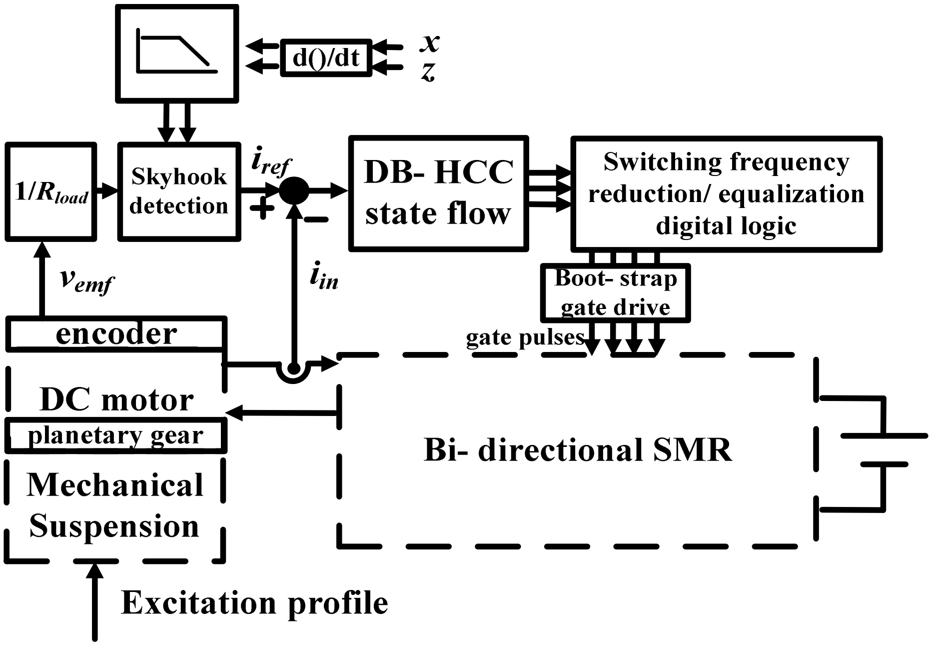

Figure 3-42: Experimental setup of regenerative suspension with active Skyhook control.

The SK detection is determined by both relative $\dot{z}$ and absolute velocity $\dot{x}$, filtered by 2nd order low- pass filter with cut- off frequencies of 2 kHz. To closely exam the Skyhook detection outcome a portion of waveforms in Figure 3-43 have been enlarged and placed in Figure 3-44. As expected, both (in Figure 3-44 (a)) and (in Figure 3-44 (b)) oscillate at excitation frequency (*f*). As a result, taking the product of both waveforms (in Figure 3-44 (c)) the Sky-hook detection outcome (in Figure 3-44 (d)) switches at roughly 2*f*, which is much lower than f_{sw}. According to active Skyhook control strategy described above, reference current i_{ref} commands the SMR for the presence/ absence of mechanical damping. When presence of damping is demanded the SMR synthesizes load resistor R_{in} = 10 Ω. On the contrary, when absence of damping is required the SMR synthesizes "open -circuit" between generator terminal, which reduces i_{in} to 0 (A). Again, the resulting gating signals are generated by DB- HCC, which regulates the error current signal within the pre- determined bands.

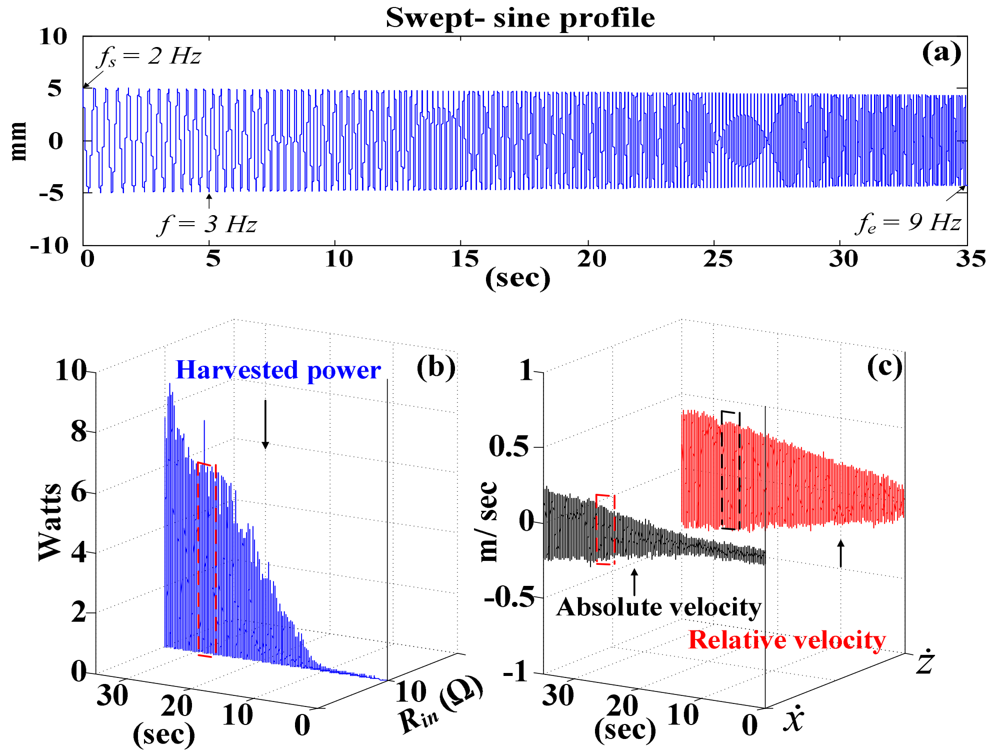

Figure 3-43: (a) Swept- sine excitation profile from 2- 9 Hz (at 0.2 Hz/ sec) in 35 (sec) with *Y*= 5mm. (b) Instantaneous harvested power, (c) absolute velocity, and relative velocity as a result of active SK with R_{in}= 10 Ω synthesis. Note: Signals inside the dashed boxes are enlarged in the next figure.

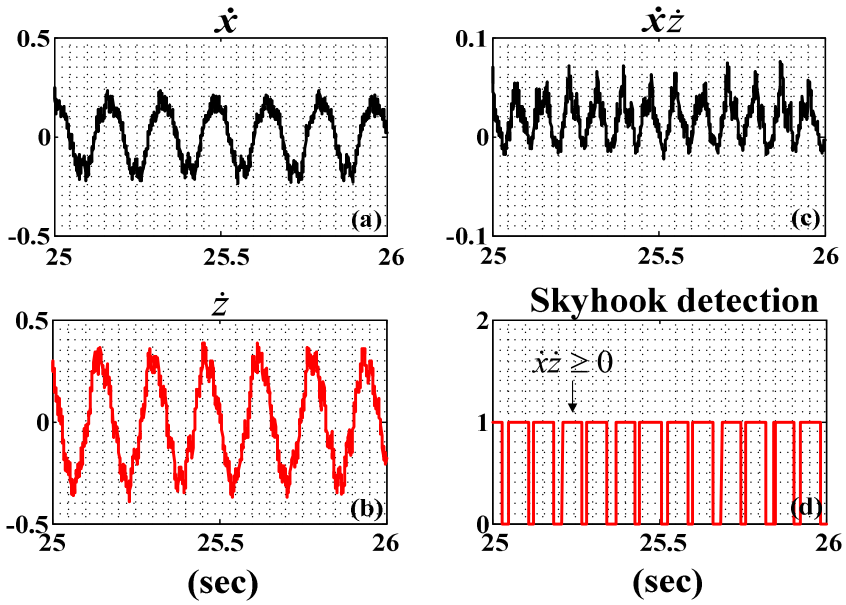

Figure 3-44: (a) Detailed absolute velocity, (b) relative velocity, (c) the corresponding product, and (d) its' SK detection outcome at $f \approx 7$ Hz.

3.8.3. Instantaneous Regenerative Semi-active Control

With the SK detection outcome, the error current (i.e. $\Delta I = |i_{in} - i_{ref}|$) is passed to the controller for generating desired gating signals. As a result, referring to instantaneous i_{in} and v_{emf} during a nominal duration in Figure 3-45 (a) and (b), it is observed the terminal current i_{in} can be controlled to synthesize either constant resistor (e.g. R_{in} = 50 Ω) or “open - circuit” as required by the detection outcome. This means that, an equivalent continuous variable damping force is provided by controlling the SMR. Furthermore, instantaneous harvested power is also demonstrated in Figure 3-46. As observed, the electromagnetic suspension regenerates power when the SK detection outcome demands presence of damping force. Thus, power regeneration is achieved while simultaneously apply the adopted control method. In addition, the comparison of transient responses (see base excitation transients in Figure 3-47(a)), between constant damping and Skyhook-type damping for R_{in}= 50 Ω, with respect to suspension relative displacement and sprung mass acceleration are also depicted in Figure 3-47 (b) - (c). Similar to Figure 3-43, the transients are captured before the arrival of steady-state response. The constant damping approach is achieved by continuously applying R_{in}= 50 Ω to the suspension system by the SMR. The Skyhook type damping follows the same principle while integrating the detection outcome, by (3-23). As observed, both acceleration and relative displacement amplitudes are smaller in Skyhook type damping approach.

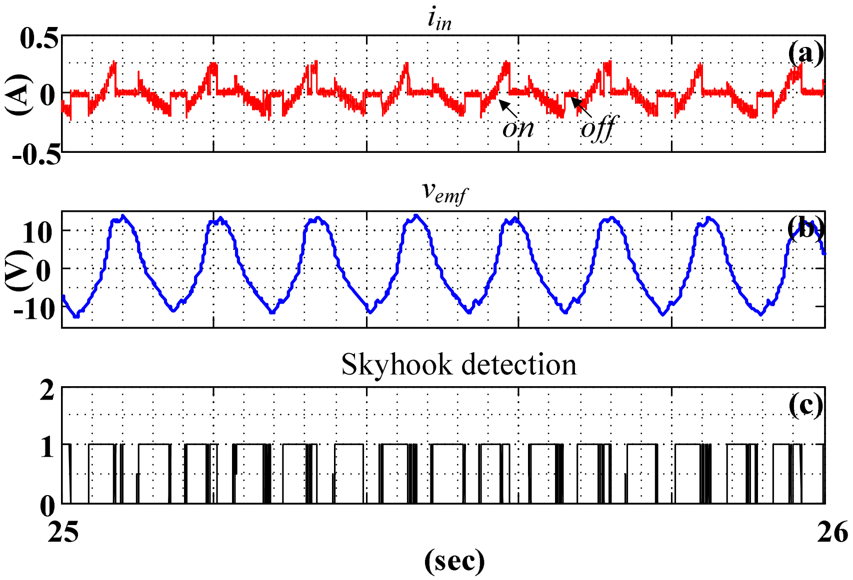

Figure 3-45: (a) Converter current i_{in} (b) and EMF voltage for R_{in}= 50 Ω synthesis according to SK detection outcome at $f \approx$ 7 Hz. Note: Examples of presence and absence of damping are indicated by “on” and “off”.

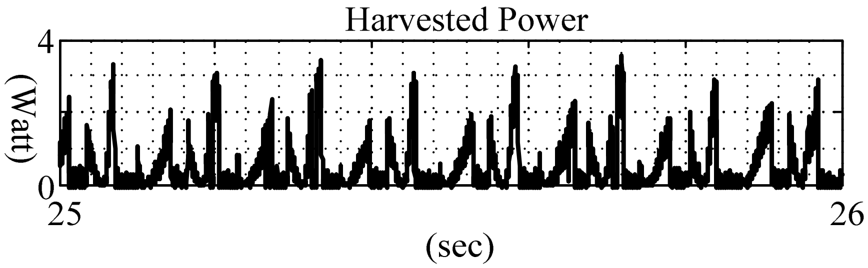

Figure 3-46: Instantaneous harvested power for R_{in}= 50 Ω synthesis according to SK detection outcome.

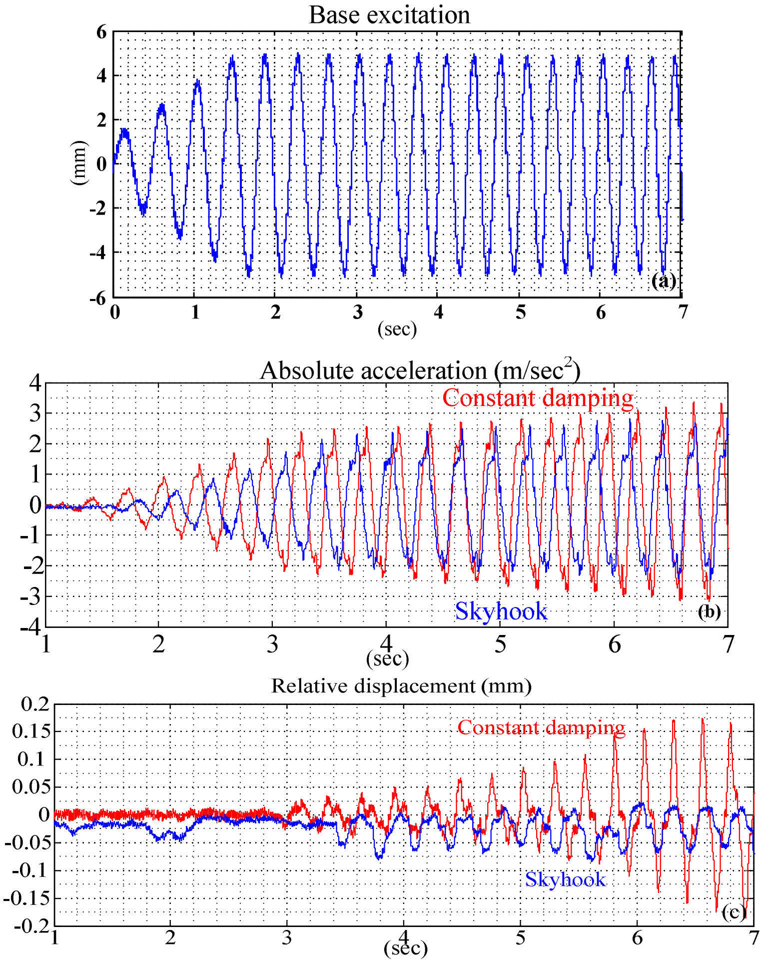

Figure 3-47: (a) Transients of base excitation profile. Comparison of (b) absolute acceleration and (c) relative displacement transients between synthesized Skyhook control and constant damping.

3.8.4. Experimental Frequency Response with Regenerative Automotive Suspension

To assess suspension dynamic performance in terms of vehicle handling and passenger comfort and harvested power, various values of R_{in} are chosen for active SK control. Again, the electromagnetic suspension is excited by profiles shown in Figure 3-43 (a). The results obtained by SMR synthesizing R_{in}= 10, 50, 100 Ω are presented as well as $R_{in}= \infty$ and 0 Ω for minimum and maximum equivalent damping are included for comparisons. In this work, $R_{in}= \infty$ and 0 Ω are realized by opening and shorting the motor terminals during the entire experiment, therefore, no power harvesting can take place.

$$\lambda_{rms} = \sqrt{\left(f_e - f_s\right)^{-1} \int_{f_s}^{f_e} \lambda^2 df} \tag{3-28}$$

$$\eta_{rms} = \sqrt{\left(f_e - f_s\right)^{-1} \int_{f_s}^{f_e} \eta^2 df} \tag{3-29}$$

$$\overline{P}_L = \left(f_e - f_s\right)^{-1} \int_{f_s}^{f_e} P_L df \tag{3-30}$$

As indicated in (3-28) and (3-29), the vehicle handling (or suspension workspace limit) and passenger comfort are measured by the RMS of suspension relative displacement transmissibility η_{rms} and sprung mass acceleration λ_{rms} over the excited spectrum (i.e. $f= f_s$ to f_e), respectively. In addition, according to (3-30), the average harvested power P_L is also assed for maximum power charging. Referring to frequency responses in Figure 3-48 and normalized RMS values tabulated in Table 3-6 it is realized R_{in} = 0 Ω offers the best vehicle handling with worst passenger comfort while $R_{in} = \infty$ Ω indicates the opposite outcome; when coupling SMR to the regenerative suspension prototype R_{in} = 100 Ω delivers the best overall handling/ comfort while R_{in} = 10 Ω scavenges the maximum amount of vibrational power.

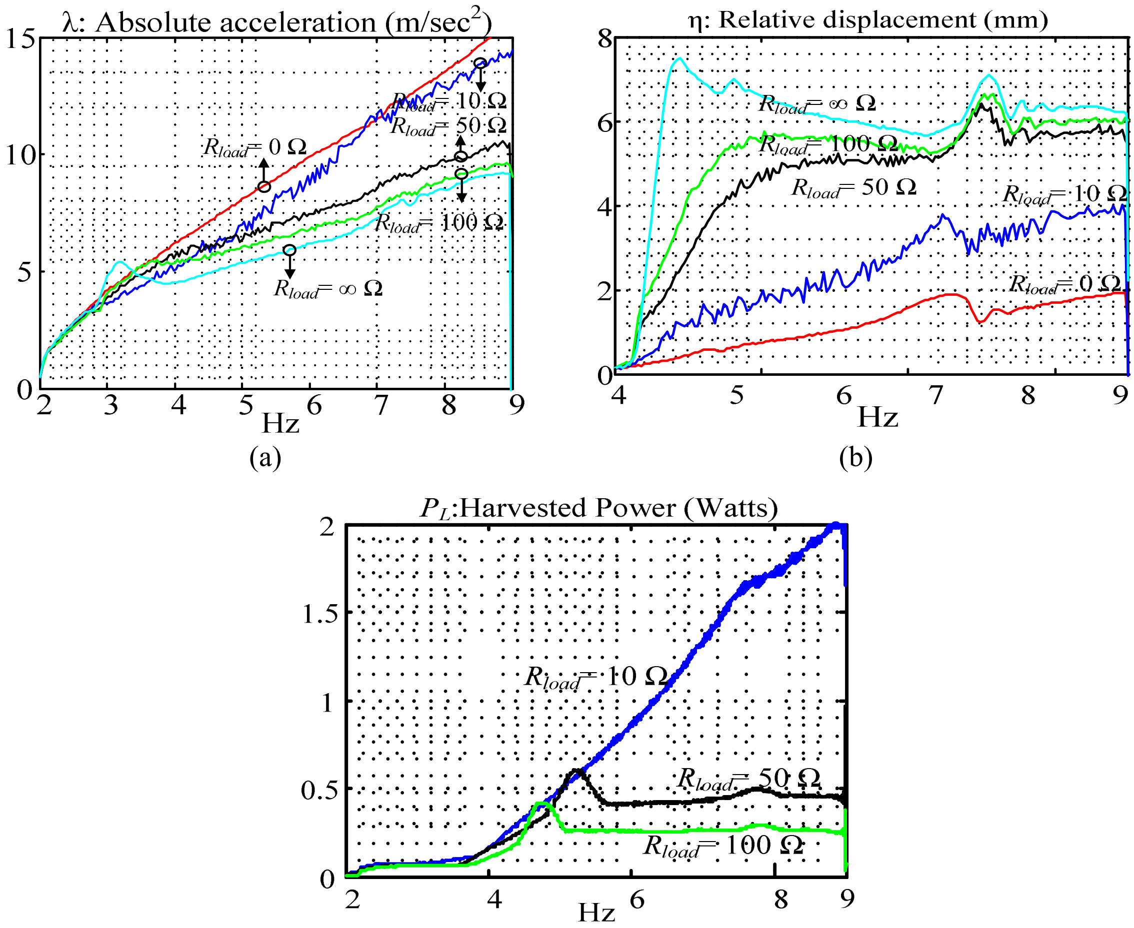

(a)

(b)

(c)

Figure 3-48: Frequency response of absolute acceleration λ (c) relative displacement transmissibility η and (d) harvested power P_L of regenerative Skyhook control algorithm for various values of synthesized R_{in}

Table 3-6 Normalized RMS of acceleration and relative displacement and average harvested power obtained with different values of R_{in}

R_{in} (Ω)	η_{rms}/η_{max}	$\lambda_{rms}/\lambda_{max}$	$\bar{P}_L/P_{L,max}$
0	0.24	1	n/a
10	0.47	0.90	1
50	0.79	0.68	0.39
100	0.86	0.63	0.25
∞	1	0.59	n/a

3.9. Chapter Summary

In this chapter, the concept of using a bi-directional switched-mode rectifier (SMR) for synthesizing variable electrical damping is demonstrated in both simulations and experimental environments. To exemplify energy harvesting capabilities, the SMR is placed under both swept-sine and ISO standard road profiles for demonstrating the current controller regulating the SMR current according to both sinusoidal and stochastic DC machine EMF, respectively. It is noted, the hysteresis current controller is able to accurately synthesize desired resistors (i.e. regulating converter current) according to line voltage (both amplitudes and frequencies) that is unknown a-priori. In addition, the integration of semi- active control and energy harvesting is denoted. It is demonstrated, through both time and frequency responses, double- band hysteresis current controller (DB- HCC) is able to selectively synthesize positive (i.e. regenerating mode), negative (i.e. motoring mode), or zero (i.e. equvilent open circuit) equivalent dampings according to the Skyhook detection outcome, which shows that the SMR, controlled by HCC, can indeed attain suspension semi- active control and road energy harvesting simulatanoeusly.

Chapter 4.

Bridgeless AC/DC Converter for Synthesizing Variable Damping

In this Chapter, a new switched-mode bridgeless AC/DC converter, operating in the discontinuous conduction mode (DCM), is presented. The converter topology consists of common source MOSFETs allows for direct AC/DC conversion, minimum auxiliary circuits and simple gating patterns, when compared to other AC/DC converters proposed in the literature. The circuit operation is analyzed and shown that the converter-battery topology can operate as a synthesized variable resistor with a regenerative functionality. The converter is integrated with a small-scaled proof-of-concept automotive suspension prototype for regeneration vibrational energy into battery charge. Experimental results of the proposed converter operation when connected to a regenerative suspension prototype for variable damping synthesis and energy harvesting are demonstrated. Moreover, power conversion efficiency of the entire mechatronic is also included.

The proposed converter can function as a sensorless (i.e. as in open-loop) variable synthesized resistor for battery charging, which can be connected to an irregular line voltage induced in a seismic environment. Furthermore, the circuit is capable of powering a DC load with a fixed voltage rating through voltage mode control (VMC). Due to nature of sensorless based, the proposed converter is able to synthesize variable resistor even at low step-up ratio (between line and load voltage) in DCM operation comparing to [115], which leads to smaller (lower power consumption assuming same power level applications) auxiliary circuit foot-print.

The circuit is designed for applications in low-power energy harvesting; for example, it regenerates energy from a vibrational power source by providing variable electrical damping. Synthesizing electrical damping is similar to achieving unity power factor between the line voltage and current (e.g., [115]-[118]) for maximum available power transfer. The proposed topology is a modified buck-boost AC/DC converter without line diodes in a full-bridge configuration. Avoiding line diodes and having simple gating pattern would enable it to operate with lower standby power loss and simpler control method compared to conventional synchronous and two-stage AC/DC topologies [56]-[59], designed for similar power level operations. Moreover, due to its simple control method, the requirement of auxiliary components is minimized resulting in a more compact converter layout, making it ideal to integrate/ retrofit with a vehicles suspension.

4.1. Comparison of Energy Harvesting Circuit Topologies

Recalling Section 2.3, the aforementioned works have contributed to the development of power converters for energy harvesting applications with certain drawbacks specifically for two-stage AC/DC converter configurations. The forward voltage drops in the full- wave rectifying diodes result in conduction power losses and efficiency degradation. To alleviate this problem, either a low conduction loss bridge rectifier or a synchronous rectifier type topology can be utilized. However, there are certain drawbacks in using these alternatives. For example, integrated bridge rectifiers are also limited by the magnitude of forward voltage drop and the continuous current conduction level. For example, HD04-T from Diodes Incorporated operates below maximum continuous current of 0.8 A, which is insufficient for large- scale harvesting. Furthermore, the power dissipation of the high-side gate driver IC for driving the n-MOSFETs in a back-end DC/DC converter (e.g. buck or buck- boost) severely reduces the power conversion efficiency [56]-[58], [59]. Alternatively, synchronous topologies can be adopted, however, it requires complex gating pattern with extra auxiliary circuitry for floating type gate drivers, which also results in extra power consumption.

The qualitative comparisons of the proposed converter with that of previously proposed topologies are indicated in Table 4-1. Numerous merits, including efficiency, power part counts, gate drives design, sensed signals, are tabulated. The two- stage topologies, implemented for pizeo-based application [56]-[58], [59], generally bears low efficiency due to its low available power level and rectification conduction loss in the AC/DC segment. The two-switch synchronous boost topologies [72] appeared with the lowest part counts and conduction loss due to absence of rectifying diode. The conversion efficiency is claimed in the vicinities of 92%, however, the power consumption and design of gate driver was not documented. A direct AC/DC topologies implemented in [74] possess high part count due to additional load battery with similar conduction loss to the proposed topology in this work. However, the switching modes and analysis of the converter operation were not clearly illustrated. Instead, the application of the converter, which is applying damping in a tuned- mass-spring- damper environment, is carried out experimentally.

Table 4-1: Energy harvesting topologies comparisons

Converter Type	Conversion efficiency	Converter part counts	Driver design	Operation modes	Sensed signals
Two-stage [56]-[58], [59] (piezoelectric)	< 50%	High	High side	DCM	Sensor-less
Synchronous boost rectifier [73] (electromagnetic)	≈ 92%	Low	n/a	DCM	Line voltage
Direct AC/DC [74] (electromagnetic)	n/a	High	n/a	DCM	n/a
Switch- mode rectifier (electromagnetic)	90- 93.5%	Low	High and low side	CCM	Line current
Proposed topology (electromagnetic)	87- 94%	Medium	Low side	DCM	Sensor-less

Similar to SMR, the proposed direct rectification topology also provides variable damping (positive) to the connected dynamic system. In addition, it provides flexibility in gate drive design, according to available power level of the seismic source, which the conventional SMR topology does not offer. Moreover, the proposed topology allows simpler transition between different switch- modes when connected to more realistic irregular voltage source. On the contrary, SMR provides bi- directional power flow, meaning it is able to provide bipolar electrical damping, while the proposed direct AC/DC converter is only capable of supplying positive electrical damping. To illustrate the operation and benefit of the proposed converter the comparisons, in terms of the various operating modes and input power, between direct AC/DC and synchronous boost rectifier [72] are demonstrated.

4.2. Proposed Bridgeless Converter Topology

The proposed converter is shown in Figure 4-1 (a), which is a single stage direct AC/DC buck-boost converter operating in DCM. The configuration is inspired by battery charging circuits, where back-to-back MOSFETs are utilized for over-charge and over-discharge protection [119]-[120]. In this converter, the common source configuration provides bi-directional current conduction and blocking capabilities. The configuration is utilized to ensure line voltage v_{in} is disconnected from inductor L during its discharging period in the entire line cycle. The back-to-back configuration is placed intentionally to prevent undesired conduction via the undesired path. For example, if SW_{MOS} only consisted of a single MOSFET with its drain connected to v_{in}, during negative line cycle, even if SW_{MOS} is turned off, the body diode will still be forward biased if v_{in} is higher than body diode forward voltage V_F.

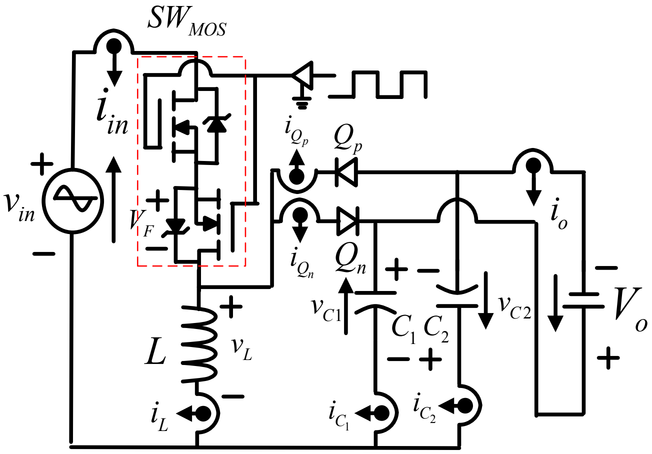

(a)

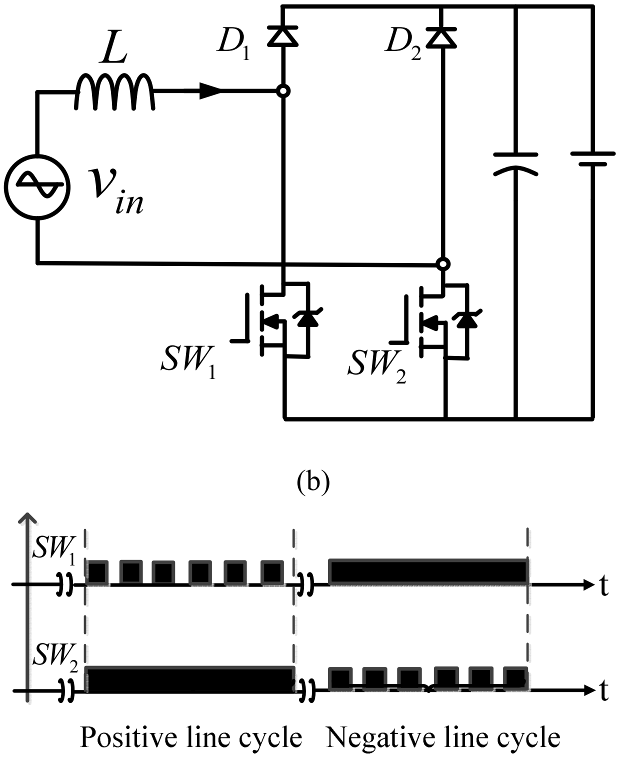

(b)

(c)

Figure 4-1: (a) Proposed bi- directional bridgeless AC/DC converter. (b) Two- switch type synchronous rectifier and (c) its' gating pattern for DCM operation.

Compared to a synchronous boost converter operating in DCM, in Figure 4-1 (b), the main advantages are as follows [72]. The conduction loss in power stage is the primary contributor of power efficiency degradation in DCM operation. Thus the proposed converter avoids additional conduction losses contributed by $R_{DS,on}$ of either SW_1 or SW_2 in synchronous boost converter (see Figure 4-1(b)) during the inductor discharging period. Moreover, the synthesized input resistance by the proposed converter is a function of time-independent variables (shown later). In addition, the gating pattern of the proposed topology is extremely straightforward, where both n-MOSFETs are gated simultaneously. On the contrary, either SW_1 or SW_2 is required to switch on for the entire half line cycle, which leads to more a complex gating pattern with line polarity detection (see Figure 4-1(c)) needed to realize such operation. In addition, the gate drive output is required to remain logic high in order for SW_2 to form a closed-loop system. Therefore, during the charging of *L,* the power dissipation/conduction losses are higher due to $R_{DS,ON}$ of SW_2. The gating pattern also leads to unequalled duty cycles and stress between both n-MOSFETs and potentially limits choosing the modulation carrier frequency and MOSFET's safe operating area (SOA).

4.3. Converter Analysis and Modelling

In this section, the switching waveforms of the proposed converter are assumed to be ideal, including MOSFET switching dynamics, zero forward voltage drops across the diodes, and zero series resistances for passive elements. Note that other than opposite current flow, in order to facilitate simple gating pattern, the operation of the proposed topology is independent of line polarity, meaning Modes 1 and 3, and Modes 2 and 4 are identical with opposite direction current flows. The circuit has four modes of operation as described in the following.

4.3.1. Modes 1 and 3

The equivalent circuit with the current flow for Mode 1 and 3 is shown in Figure 4-2. To illustrate the switching waveforms in different switching modes, line current i_{in}, average line current $i_{in,avg}$, average output current $i_{o,avg}$, diode current, inductor current i_L, inductor voltage v_L, line voltage v_{in}, capacitor current, and duty cycle of SW_{MOS} are shown in Figure 4-3. In Mode 1, SW_{MOS} is switched on, with the top n- MOSFET operating in the forward conduction mode and the bottom MOSFET in the reverse conduction mode. The charging of L will take place in Mode 1 since $V_{L,boost} = v_{in} > 0$. Since both Q_p and Q_n are reverse biased, current does not flow into the load. The same operation takes place in Mode 3, since negative line cycle imposes negative v_L across L, therefore, inducing reverse direction of i_{in} and i_L.

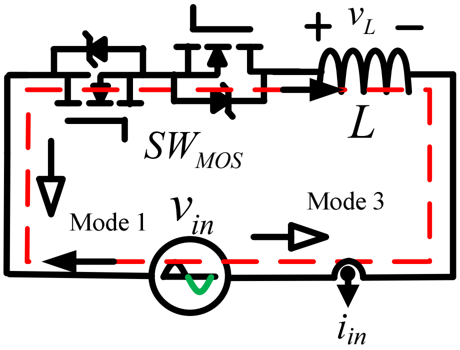

Figure 4-2: Mode 1/3 equivalent circuit.

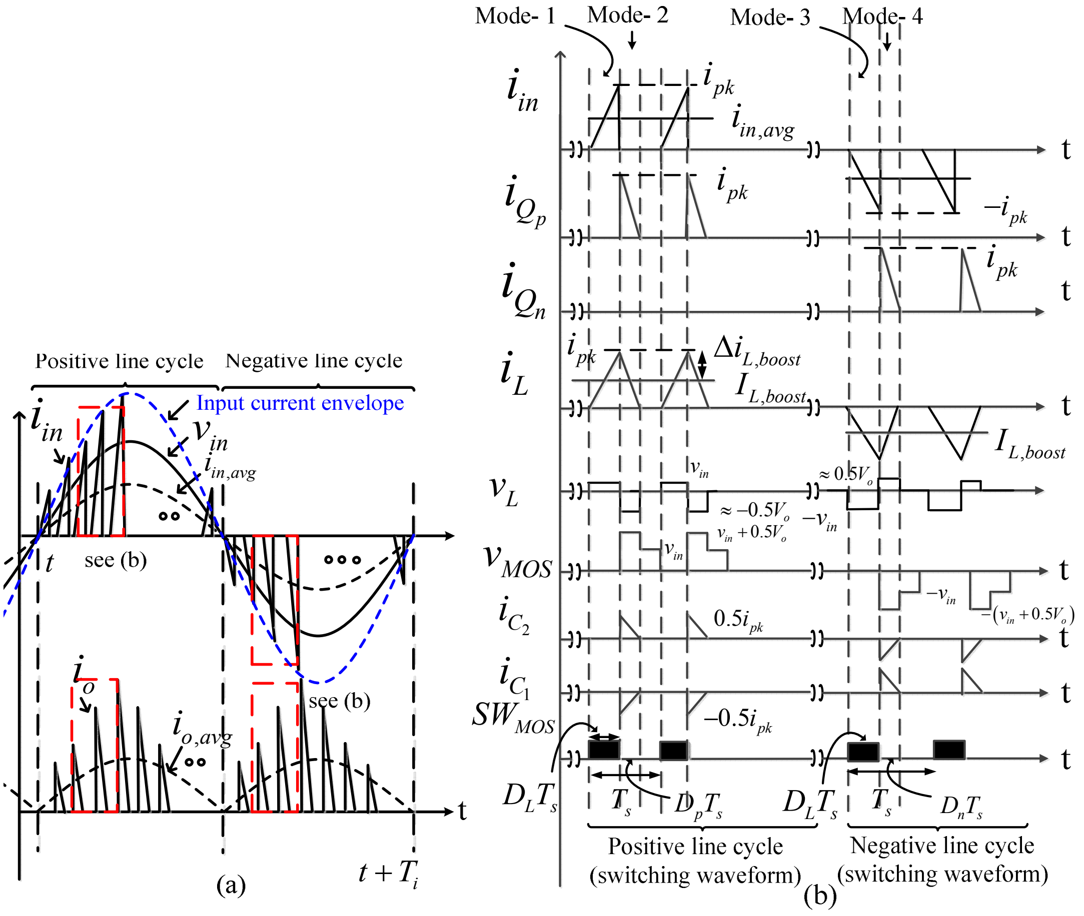

Figure 4-3: (a) Ideal theoretical switching waveforms in single line cycle and (b) switching periods.

4.3.2. Modes 2 and 4

In Mode 2, n-MOSFETs SW_{MOS} are switched off to allow the energy stored in L to discharge into the load, as depicted in Figure 4-4 (a). Since the total voltage across C_1 and C_2 is V_o, the current charges both C_2 and the battery, C_1 is discharged. In this mode, $V_L = v_{in} - V_o < 0$; hence, the rectifying diode Q_p is forward biased for the duration D_pT_s in order to charge the load and ensure validity of volt-sec balance principle. After i_L reaches zero, $V_L = 0$ and the entire converter is essentially switched off. The identical operation with reverse inductor current flow takes place in Mode 4 as shown in Figure 4-4 (b).

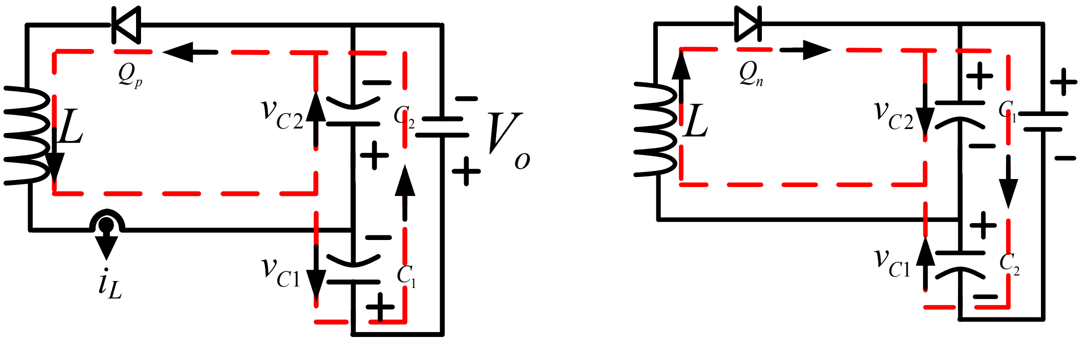

(a) (b)

Figure 4-4: (a) Mode 2 and (b) Mode 4 equivalent circuits of bridgeless AC/DC converter.

4.3.3. Converter Synthesized Resistor

As mentioned previously, synthesizing variable resistors is equivalent to providing mechanical damping in the electrical domain. In this case, the equivalent variable input resistance are defined in terms of line voltage to both envelope and average input current as envelope input resistance and average input resistance, respectively. Before deriving the expressions for input resistances seen from the line terminal the average input power of the proposed converter is derived as the following

$$P_{in} = \frac{2}{T_i}\int_{0}^{\frac{T_i}{2}} \frac{E_{in}}{T_s}\,dt = 0.25 D_L^2 T_s V_{in}^2 L^{-1} \tag{4-1}$$

where D_L is the duty cycle, V_{in} is line voltage amplitude, E_{in} is converter input energy, T_i is line voltage period, and T_s is switching period. According to (4-1) the input power of the proposed converter varies solely as a function of input voltage (assuming other parameters remain constant); thus making it ideal for resistor synthesis.

Similarly, average input power of the synchronous boost converter, operating in DCM, is derived as

$$P_{in,SB}=\int_0^{\pi}\left(\frac{D_L^2T_s}{2L\pi}\right)\frac{\left(V_{in}\sin\theta\right)^2}{1-\dfrac{V_{in}}{V_o}\sin\theta}d\theta\approx 0.25V_{in}^2D_L^2T_sL^{-1} \tag{4-2}$$

where V_o is load voltage and $\theta{=}2\pi T_i^{-1}t$. Note that the input power in (4-2) can only be approximated, since the instantaneous term, $A=\int_0^{\pi}\sin(\theta)^2\left(1-V_{in}V_o^{-1}\sin\theta\right)^{-1}d\theta\approx 0.5\pi$ when $V_{in}{<<}V_o$ is assumed as shown in Figure 4-5.

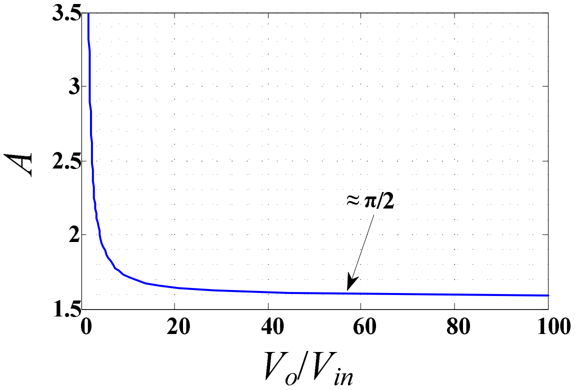

Figure 4-5: Approximation of input power instantaneous term with respect to step-up ratio.

The comparisons of input powers for both converters in terms of squared duty ratios are depicted in Figure 4-6. The values adopted are L= 1 mH, V_{in}= 3 (V), T_s= 1 msec, V_o= 24 (V). Comparing (4-1) and (4-2), the input power of the proposed converter is solely a function of input voltage (assuming other parameters remain constant); thus making it synonymous to that of physical resistor and ideal for resistor synthesis. On the contrary, input power of the synchronous boost converter is a function of V_{in} and V_o, making the synthesized resistor nonlinear (when duty cycles not properly tuned).

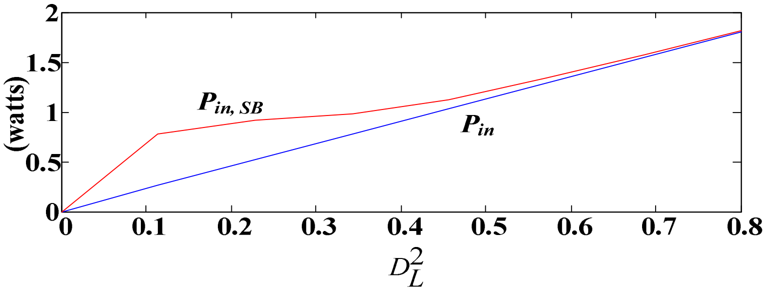

Figure 4-6: Input power comparison of proposed AC/DC converter P_{in} and switch mode rectifier $P_{in,SB}$.

The average line current $i_{in,avg}$ and rectified current $i_{o,avg}$, shown in Figure 4-3(a), are obtained as follows

$$i_{in,avg} = 0.5 v_{in} D_L^2 T_s L^{-1} \tag{4-3}$$

$$i_{o,avg} = v_{in}^2 D_L^2 T_s L^{-1} V_o^{-1} . \tag{4-4}$$

From (4-3)-(4-4), it is observed that $i_{in,avg}$ oscillates with respect to T_i while $i_{o,avg}$ is summation of both DC and second harmonics $(2T_i)^{-1}$ terms. In addition, to ensure DCM operation, the maximum duty cycle of gating pulses is also derived as

$$D_{L,max} < V_{in} V_o \left(V_{in} V_o + 2V_{in}^2 \right)^{-1} . \tag{4-5}$$

Combining (4-1)-(4-4), the average line resistance of the proposed converter (i.e., R_{in}) is defined as follows

$$R_{in} = \frac{v_{in}}{i_{in,avg}} = \frac{2L}{D_L^2 T_s} . \tag{4-6}$$

Referring to (4-6) , it is noted that R_{in} is solely a function of constant parameters. The envelope input resistance is defined as the input voltage over the input current envelope. Since the converter is operating in DCM, after $D_L T_s$, the peak value of inductor current is given by

$$i_{pk} = v_{in} D_L T_s L^{-1} . \tag{4-7}$$

Therefore, the envelope input resistance can be written as

$$R_{in\_ev} = \frac{L}{D_L T_s} . \tag{4-8}$$

From (4-8), it is noted that $R_{in} = 2D_L^{-1} R_{in\_ev}$, which is larger than the envelope input resistance by more than a factor of two. This is expected since the converter operates in DCM.

4.4. Simulation Results with Single Tone AC Source

4.4.1. Line Voltage, Line Current, and Filtered Line Current

Before demonstrating the experimental results the simulation studies to verify the analytical results and performance of the proposed bridgeless converter were performed using MATLAB SIMULINK/ SimPowerSystem toolbox and *PSIM*. The parameters, for DCM operation, were chosen as follows: fixed inductor L= 1 mH, inductor r_{ESR}= 370 mΩ, vibrational frequency f_i= 10 Hz, switching frequency f_{sw} = 1 *k*Hz>> f_i, line voltage amplitude V_{in}= 5 V, and battery voltage V_o = 15 V. Substituting into (4-5), $D_{L,max}$= 0.6 is obtained for ensuring DCM operation. Moreover, the physical components, shown in Table 3-3, were selected for switching waveform and power efficiency simulations.

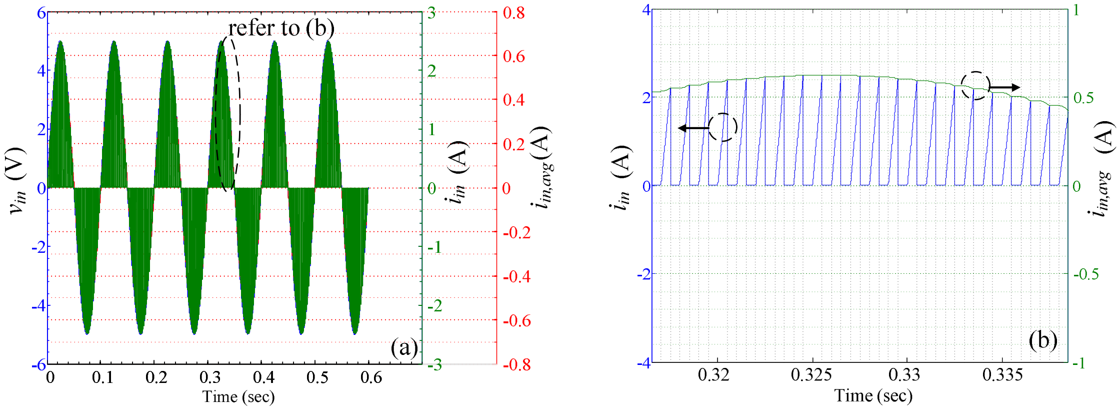

Figure 4-7: (a) Simulated switching waveform of line voltage v_{in} (left x- axis), line current i_{in} (right inner x- axis), and average line current $i_{in\ avg}$ (right outer x- axis), (b) Detailed switching waveform of i_{in} (left x- axis) and $i_{in,avg}$ (right x- axis) during positive cycle with duty cycle D_L = 50%.

Substituting values of L, D_L, and f_{sw} into (4-6) and (4-8), the average line resistance and envelope resistance are obtained as R_{in}= 8 Ω and R_{in_ev} = 2 Ω, respectively. The values can be verified by taking the amplitude ratios between v_{in}, i_{in} and $i_{in,\ avg}$ as indicated in Figure 4-7. Note $i_{in,\ avg}$ is obtained by averaging i_{in} every switching interval.

4.4.2. Inductor and Rectifying Diode Current

According to the equivalent circuit in both Modes 1/4 and 2/3, the inductor L acts as a current source by charging from line and discharging to load. Incorporating various conduction losses during charging period (i.e. Modes 1/4) and discharging period (i.e. Mode 2/3), the input and output voltages with respect to i_{in} and i_L are approximated as follows

$$v_{in} \approx L\frac{di_{in}}{dt} + i_{in}\left(r_{DS,on} + r_{ESR}\right) \tag{4-9}$$

$$V_o \approx 2\left(L\frac{di_L}{dt} + i_L r_{ESR} + V_F\right) \tag{4-10}$$

where $r_{DS,on}$= 0.7 Ω, r_{ESR} = 0.37 Ω, V_F= 0.39 V are MOSFET on-time resistance, inductor equivalent series resistance, and diode forward voltage drop. Substituting the adopted parameters one would obtain $i_{pk} \approx 2.5$ A with D_L = 50 %, f_{sw} = 1 *k*Hz, L= 1 mH, V_{in}= 5 V, which matches with the simulated waveforms in Figure 4-8 (a). To verify i_L in Figure 4-3 the detailed switching waveforms from Mode 1 to 4 in both positive and negative line cycles are shown in Figure 4-8 (b) and (c). Subsequently, the load current flowing through rectifying diodes Q_p, load capacitors C_1, C_2, and battery are simulated as shown in Figure 4-9. As illustrated, during positive line cycle, $i_{Qp}= |i_{C1}|+|i_{C2}|$, $i_{C1}+i_{C2}$= 0A, and the battery current is given by $i_o= i_{C2}$. The voltage across C_1 and C_2, shown in Figure 4-10, are charged/ discharged alternatively with respect to line cycle polarities. The voltage across C_1 (i.e. v_{C1}) and C_2 (i.e. v_{C2}) sums up to V_o, which is due to opposite current flow during both discharging periods taking place in Mode- 2 and 4 as shown previously

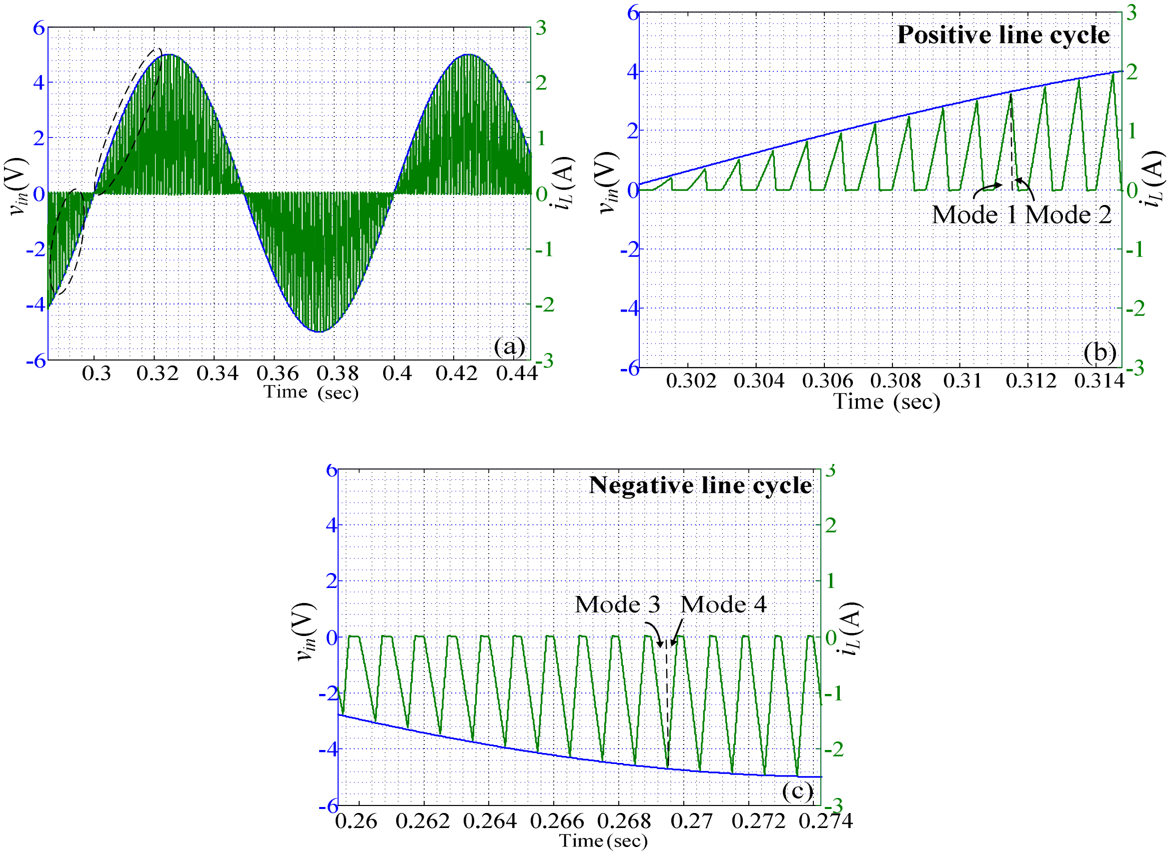

Figure 4-8: (a) Simulated switching waveform of line voltage v_{in}, inductor current i_L. (b) Detailed switching waveform during positive and (c) negative line cycle.

Rectifying diodes *Qp*
Load capacitors *C1*, *C2,* and Battery current

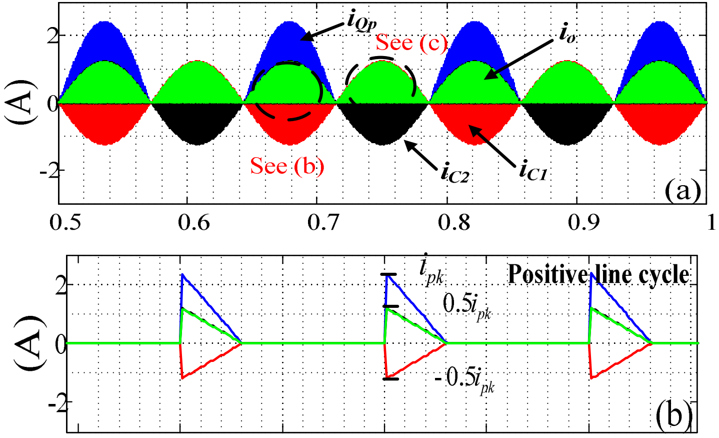

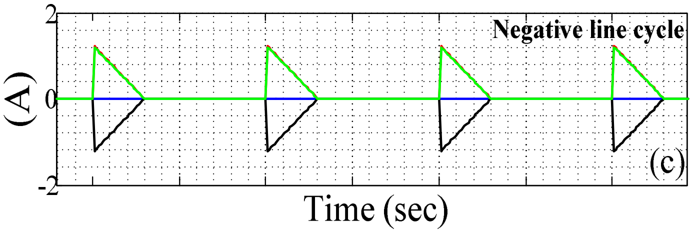

Figure 4-9: (a) Simulated switching current waveform of Q_p, C_1, C_2, and battery current i_o. (b) Detailed switching waveform during positive and (c) negative line cycle.

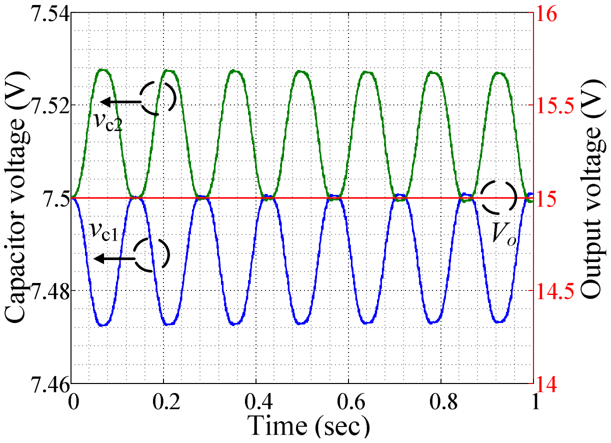

Figure 4-10: Capacitors voltage ripples.

4.4.3. Power Efficiency

Converter power efficiency can be calculated by measuring converter's input and output power. Detailed estimation of power efficiency is performed by calculating the power losses of main converter components. The conduction/switching power losses of semiconductors and other passive elements are estimated using *PSIM* as depicted by the schematic in Figure 4-11. The thermal module allows including MOSFETs main parameters under various testing conditions such as maximum drain–source voltage V_{DS_MAX}, maximum drain current I_{D_MAX}, and switching frequency. Pre-dominant parameters such as maximum reverse recovery voltage V_{RRM_MAX}, maximum continuous forward current I_{F_MAX}, and forward voltage V_F can be included for diode switching and conduction loss calculations. The power loss of passive elements can be approximated by ESR. In addition, more detailed estimation can be performed by measuring the junction thermal resistance $R_{th(j\text{-}c)}$ and $R_{th(c\text{-}s)}$, heat sink thermal resistance, and ambient temperatures.

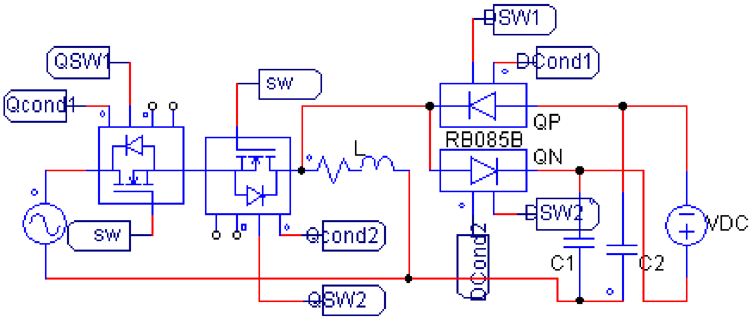

Figure 4-11: Component power loss simulation in *PSIM* using thermal module.

The power efficiency is generally defined as follows:

$$\eta = \frac{P_{out}}{P_{in}} = 1 - \frac{P_{loss}}{P_{in}} \tag{4-11}$$

where P_{out}, P_{in}, and P_{loss} are the output power, input power, and power losses contributed by physical components of the power converter.

The simulated power efficiency, shown in Figure 4-12, is obtained by both methods indicated in (4-11). The primary contributor of total power loss comes from rectifying diode conduction loss [59]. The results, obtained in *PSIM*, are plotted with respect to synthesized resistance. As depicted, both methods demonstrate highly correlated results. The highest conversion efficiency of ≈ 93% at $R_{in} \approx 22\ \Omega$ is obtained in simulation. In addition, the experimental power efficiencies (shown in dashed line) with $R_{in} = 10, 30, 50\ \Omega$ are arbitrarily selected for experimental result presentation. The details are outlined in the following section.

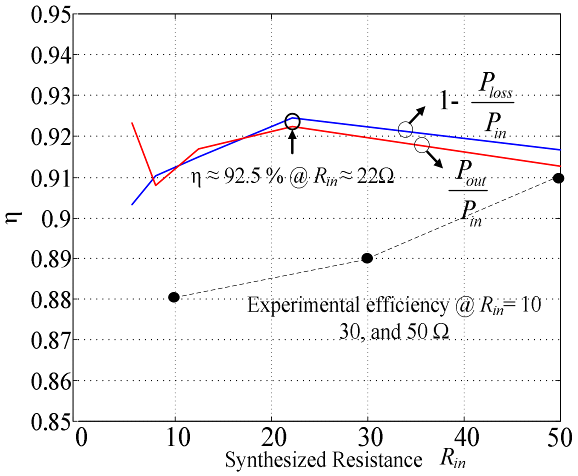

Figure 4-12: Simulated and experimental power efficiency with respect to various synthesized resistances. Note: The experimental work (black dashed line) is outlined in later sections.

4.5. Experimental Results with Single Tone AC Source

In this experiment, a programmable AC source (61501 of Chroma Systems Solutions) was utilized as a single-phase floating AC power source. Other components adopted are tabulated in Table 4-2. To balance the tradeoff between MOSFET on-state resistance and gate charge, considering the general figure of merit $R_{,DS(ON)} \times Q_g$, n-MOSFET array FDC 8602 by Fairchild Semiconductor was selected. In general, higher $R_{,DS(ON)}$ leads to higher conduction power loss, while larger Q_g leads to larger switching loss due to longer turn- on and off times.

Table 4-2: Power components selected for switching waveform and power efficiency simulation.

Component	Manufacture	Part number
n- MOSFET	Fairchild Semiconductor	FDC 8602
Power Inductor	Coilcraft	PCV- 2- 105- 02L
Electrolytic Capacitor	Nichicon	UVR1J682MRD
Schottky Diode	Fairchild Semiconductor	MBR0520
Seal Lead- acid Battery	Infinity Battery	I232/ IT 1.3- 12

The oscilloscope waveforms of MOS gating signals, battery voltage V_o, line voltage v_{in}, and inductor currents i_L are depicted in Figure 4-13. The waveforms were captured using MATLAB Instrument Control Toolbox interfaced with Tektronix TPS oscilloscope with GPIB communications. The record length for each scope channel is 2500 samples.

4.5.1. Current switching waveforms and Variable Resistor Synthesis

In this experiment, the following numerical values were measured/ adopted: $L \approx 1\ mH$, $f_{sw} \approx 2\ kHz$, $v_{in} = 2.5\ sin\ (20\pi t)$, and $V_o = 12$ (V). The PWM signal has a switching frequency of $f_{sw} \approx 2\ kHz$ with $D_L = 0.2$ as depicted in Figure 4-13 (a). The 12 (V) lead- acid battery voltages is indicated in Figure 4-13 (b). The line voltage, fed by the programmable AC power source, is shown in Figure 4-13 (c). Figure 4-13 (d) indicates the voltage reading, by Linear Technology LT 1999-20 current transducer (CT), of the inductor current. Rearranging (4-8) and considering the voltage gain of the current sensor (i.e. $G \approx 2$ A/V), inductor current is given by

$$i_{L,CT} = v_t \left(\frac{L}{D_L T_s} \right)^{-1} \left(G \right)^{-1} \tag{4-12}$$

In this case, since the n-MOSFETS were gated with $D_L = 0.2$ at $f_{sw} \approx 2\ kHz$ then $i_{pk} \approx 0.25$ A, which corresponds to 0.125 (V).

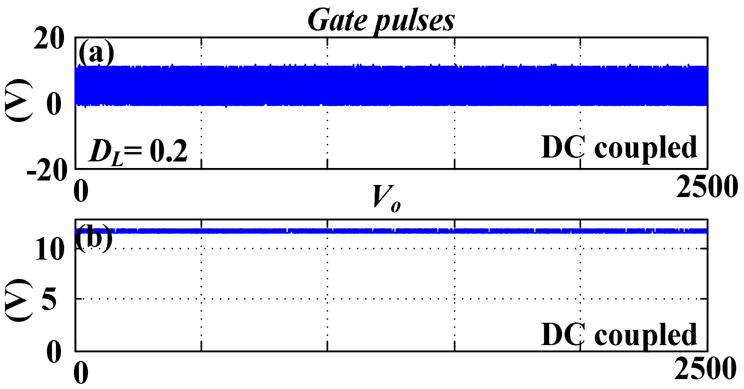

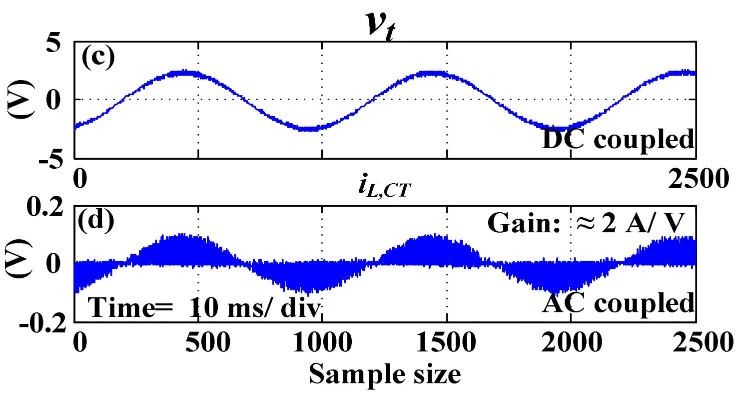

Figure 4-13: (a) Gating pulses with $D_{L=}$ 0.2 at f_{sw} = 2 *kHz* (b) load battery voltage (c) line voltage (d) inductor current. Record Length: 2500 (points).

The detailed switching waveforms of inductor current with corresponding gating pulses and line cycles are shown in Figure 4-14. According to (4-12), with $f_{sw} \approx 2$ *kHz*, D_L= 0.2, $|V_{in}| \approx 2$ (V), we should obtain peak value of inductor current $\hat{i}_{L,CT}$ = + 0.1 (V) and -0.1 (V) in both positive and negative line cycles. As indicated, the switching waveform of $i_{L,CT}$ ramps up/ down for charging/ discharging in both positive and negative line cycles. The non- idealities of ramp slope can be shown by taking the KVL of the converter during on/ off durations of the MOSFETs as follows

$$v_{in} \approx L\frac{di_{in}}{dt} + i_{in}\left(R_{DS,on} + r_{ESR}\right) \tag{4-13}$$

$$V_o \approx 2\left(L\frac{di_L}{dt} + i_L r_{ESR} + V_F\right) \tag{4-14}$$

where $R_{DS,\mathrm{on}}$ is the n- MOSFET on- time resistor, inductor ESR is represented by r_{ESR}, the diode forward voltage drop is shown as V_F.

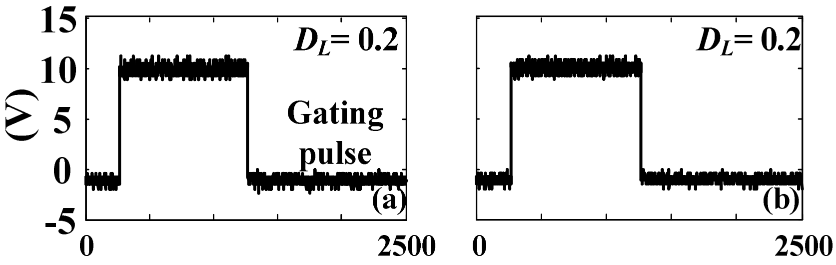

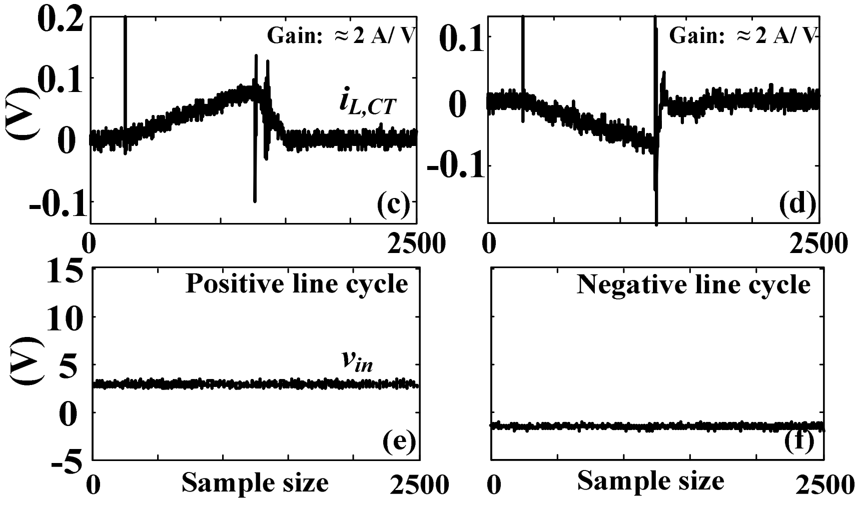

Figure 4-14: Switching waveform of (a)- (b) detailed gating signal with corresponding inductor current $i_{L,CT}$ (c)- (d) in both (e) positive and (f) negative line cycle with $|V_{in}| \approx 2$ (V).

4.5.2. Variable Resistor Synthesis

Different values of the synthesized resistor R_{in} can be obtained by varying D_L using (4-6). In this experiment, the switching waveforms of input current i_{in} (i.e., inductor current during on-time of n- MOSFETs), with D_L= 0.2, 0.4, and 0.6, is shown in Figure 4-15. Again, referring to (4-12) the voltage readings by CT should roughly correspond to 0.125 (V), 0.25 (V) and 0.375 (V), respectively.

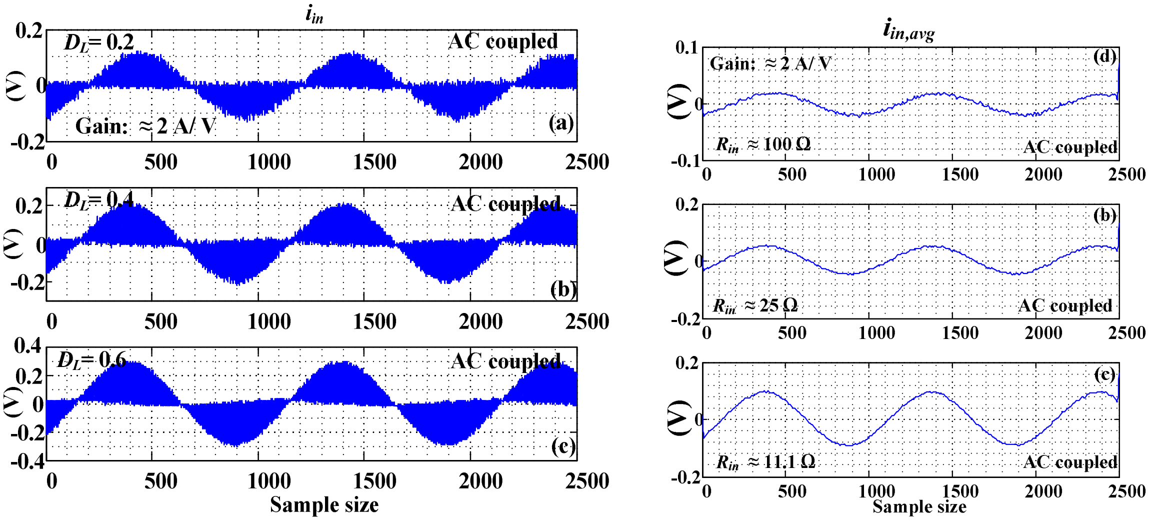

Figure 4-15: Oscilloscope waveforms of i_{in} for (a) D_L= 0.2 (b) D_L= 0.4, and (c) D_L= 0.6. Filtered waveforms of i_{in} for (d) D_L= 0.2 (e) D_L= 0.4, and (f) D_L= 0.6.

To verify the synthesized resistor R_{in}, i_{in} is filtered (denoted by $i_{in,avg}$) using with a second-order low pass filter at a cutoff frequency of 500 Hz, shown in Figure 4-15 (d)- (f). Synthesized R_{in} can be calculated by taking the amplitude ratio between v_{in} and $i_{in,\ avg}$. In this experiment, we nominally synthesize $R_{in} \approx 100\ \Omega$ (Figure 4-15 (d)), 25 Ω (Figure 4-15 (e)), and 11 Ω (Figure 4-15 (f)), which can be verified by substituting into (4-6), with D_L= 0.2, 0.4, and 0.6, respectively.

4.5.3. Load Capacitor Voltage

As illustrated by equivalent circuits in Figure 4-4, the voltage across C_1 (i.e. v_{c1}) and C_2 (i.e. v_{c2}) add up to V_o, which is contributed by opposite current flow during both discharging periods taking place in Mode 2 and 4, respectively. This implies that the capacitor voltage ripples are 180 (deg) out of phase. The sum of instantaneous voltages across capacitors C_1 (i.e. v_{c1}) and C_2 (i.e. v_{c2}) roughly equals to 12 (V), which is the rated voltage of the load battery.

The experimental voltages across capacitors C_1 and C_2 along with its detailed ripples $v_{r,c1}$ and $v_{r,c2}$, are shown in Figure 4-16 (a) and 10 (b), respectively. Considering the direction of inductor current i_L in Figure 4-4, it is observed that when C_2 charges, C_1 will discharge and vice versa. The amount of capacitor voltage ripples for both C_2 and C_1 can be approximated as follows

$$v_{r,c1} \approx 0.5 T_s C_1^{-1} i_{C1} \tag{4-15}$$

$$v_{r,c2} \approx 0.5 T_s C_2^{-1} i_{C2} \,. \tag{4-16}$$

Due to mismatches in capacitor values and other non-idealities we can approximate $v_{r,c1} \approx v_{r,c2}$.

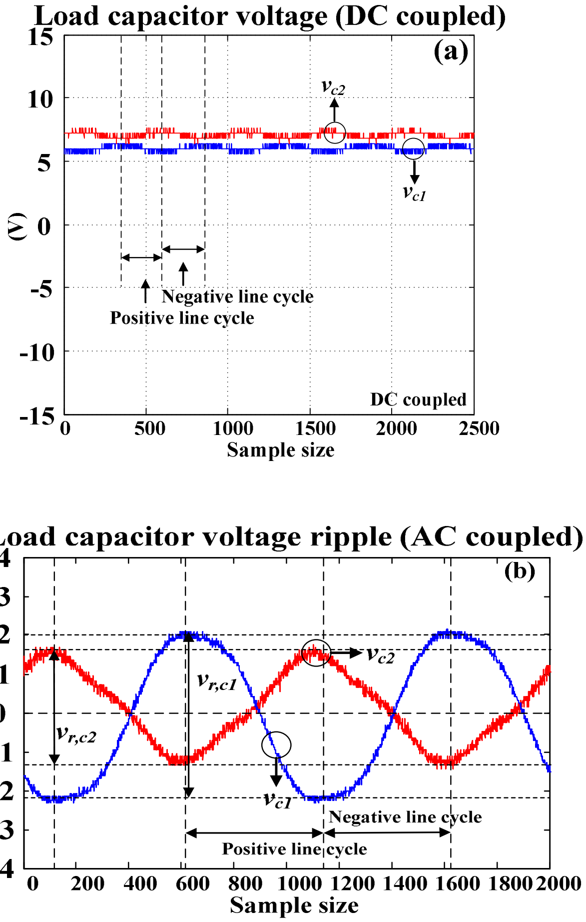

Figure 4-16: (a) Load capacitor voltages and (b) corresponding ripple voltages.

4.6. Variable Synthesized Resistor with Fixed Excitation Frequency

In this experiment, the suspension is excited by vibrational frequency of f_i= 5 Hz with amplitude of Y= 5 mm. The sampling frequency of PWM is the same as aforementioned experiments. The signal processing was implemented under MATLAB/SIMULINK RTW environment and built to the target hardware. To accurately verify R_{in}, input current i_{in} is averaged instantaneously in every switching period (denoted by $i_{in,avg}$), in real-time on the dSPACE controller board. The synthesized R_{in} is swept from 10 to 50 Ω with increments of 20 Ω.The resulting converter current for the entire sweeping is depicted in Figure 4-17 (a). The detailed depiction of current waveform for R_{in} = 10 Ω is demonstrated in Figure 4-17 (b). Referring to Figure 4-18 (a) both v_{in} (left y-axis) and $i_{in,avg}$ (right y-axis), by exciting the regenerative suspension for 15 sec, are documented for synthesizing R_{in}= 10, 30, 50 Ω with $D_L \approx$ 45%, 26%, 20%, respectively. Both v_{in} and $i_{in,avg}$ are filtered by a general 2nd- order low pass filter with a cut-off frequency of 500 Hz.

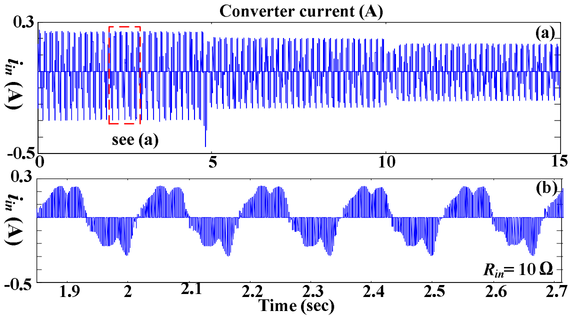

Figure 4-17: Converter current i_{in} from sweeping of synthesized R_{in}.

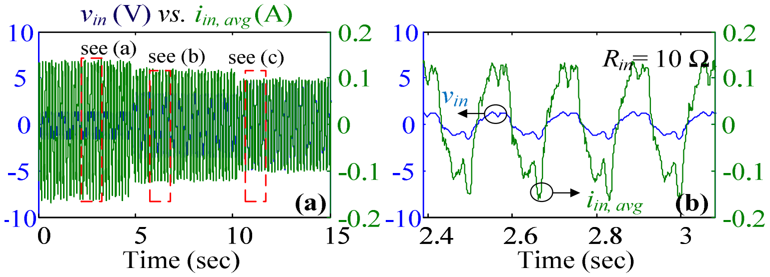

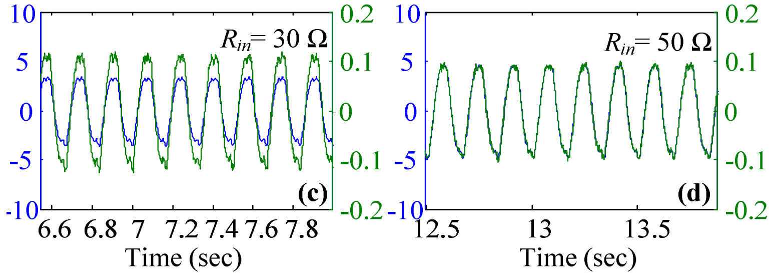

Figure 4-18: (a) Sweeping of synthesized R_{in} with detailed instantaneous waveform of v_{in} vs. $i_{in,avg}$ indicating (b) R_{in} = 10 Ω, (c) 30 Ω, and (d) 50 Ω.

As depicted in Figure 4-18 (b), (c) and (d), the average input current $i_{in,avg}$ is observed to be in-phase (i.e., high power factor) with v_{in} while maintaining the corresponding amplitude ratio. Thus the converter can provide the desired electrical damping by harvesting real power from the regenerative vehicle suspension. The power conversion efficiency for different values of R_{in} are displayed in Figure 4-19. Referring to (3-17) the overall experimental efficiencies for R_{in}= 10, 30, 50 Ω are $\eta \approx$ 88 %, 89 %, and 91 %, respectively.

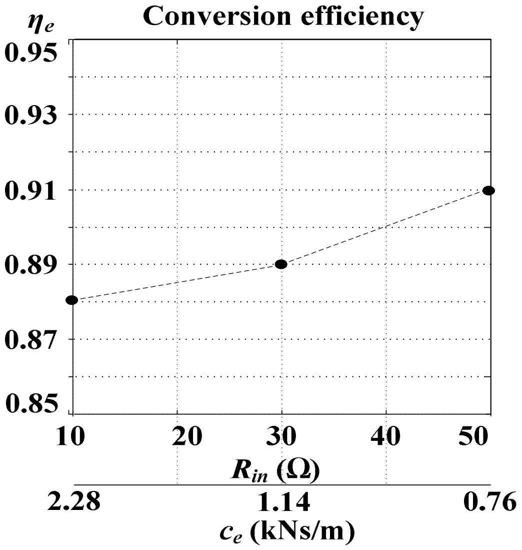

Figure 4-19: Conversion efficiencies of power converter η_e with respect to various synthesized resistances R_{in} and corresponding damping coefficient c_e . Recall Figure 4-12.

4.7. Variable Excitation Frequency with Fixed Synthesized Resistor

The suspension prototype was excited by the MTS hydraulic actuator from f_i= 5 to 10 Hz incrementing at 0.1 (Hz/ sec) for 50 (sec). The excitation profile driving the hydraulic actuator is shown in Figure 4-20. Similar to the experimental setup for the SMR the direct AC/DC converter harvests the available power generated by the seismic DC machine. To verify variable resistor synthesis by the proposed converter prototype, which is shown in Figure 4-21 (a)-(b), the line of the converter is connected to a 1-DOF regenerative suspension system with the arrangement shown in Figure 4-21 (c). The load is connected to rechargeable battery packs, which are connected in series through the spade terminals are shown in Figure 4-21 (d).

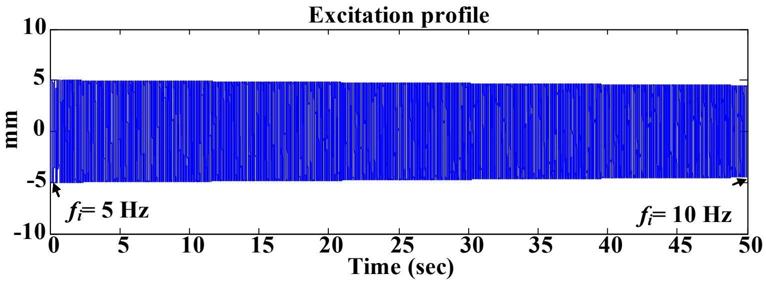

Figure 4-20: Experimental hydraulic shaker excitation profile.

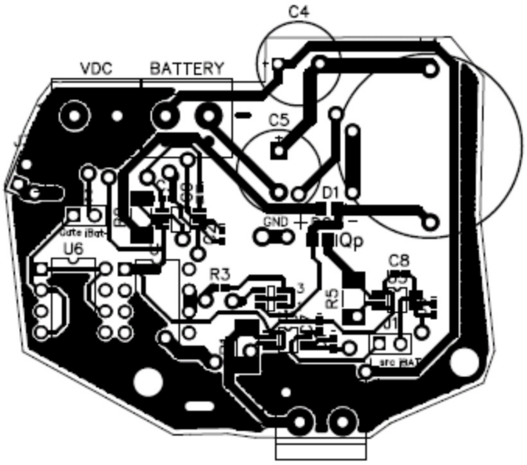

(a)

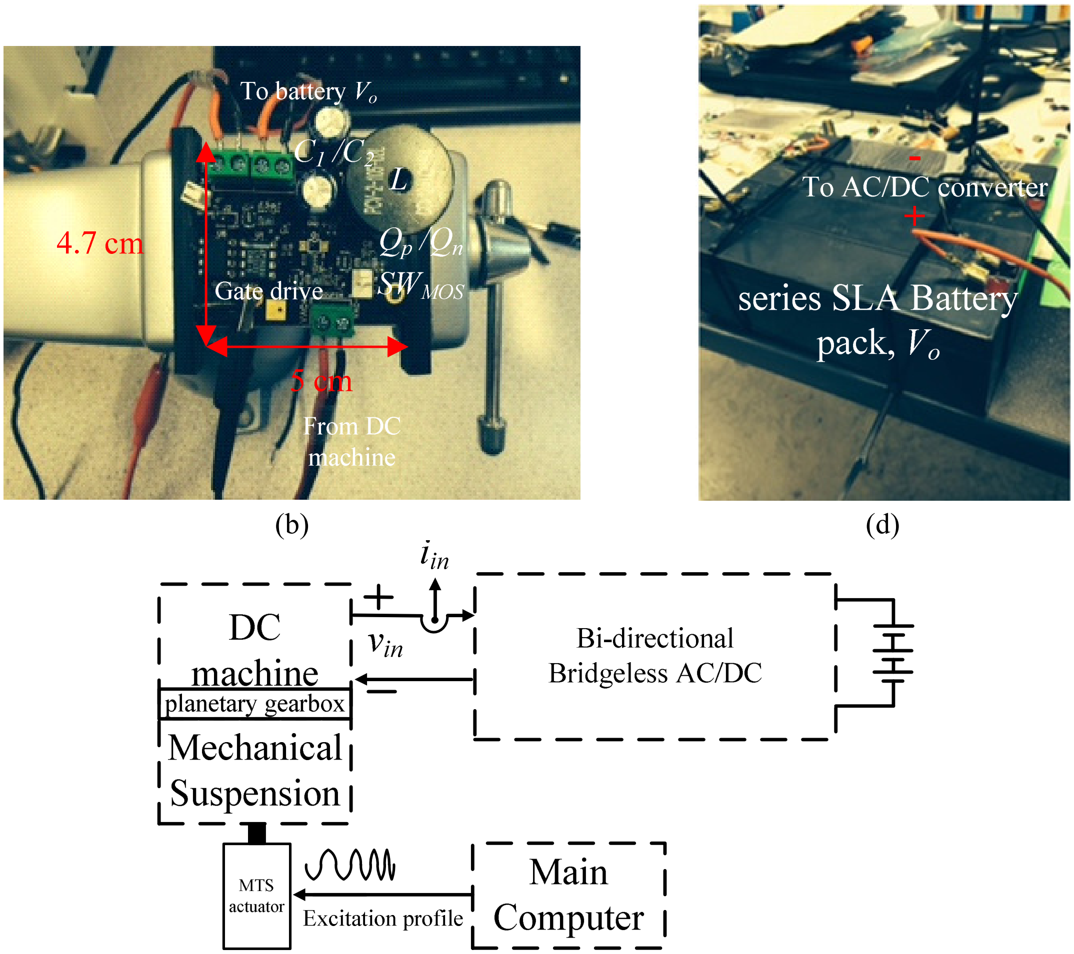

(b) (d)

(c)

Figure 4-21: (a) PCB components drawing of the bi-directional bridgeless AC/DC converter and (b) its' coreesponding prototype. (c) Experimental setup of the mechatronic system. (d) Series SLA battery packs.

The waveforms of v_{in} and $i_{in,avg}$, obtained through the excitation profile in Figure 4-20, are depicted in Figure 4-22. In this experiment, the synthesized resistor R_{in} was arbitrarily chosen as 10 Ω. Referring to Figure 4-22 (b) and (c), over the excited frequencies, average input current $i_{in,avg}$ is observed to be in-phase (i.e., high power factor) with v_{in} while maintaining the corresponding amplitude ratio, Thus the converter can provide the desired damping in the electrical domain by harvesting real power from the regenerative vehicle suspension. In this experiment, the average power regenerated over f_i= 5-10 Hz in 50 (sec) duration is approximately 1.73 W. Again, both v_{in} and $i_{in,avg}$ are filtered by a passive 2nd- order low pass filter with a cut- off frequency of 500 Hz.

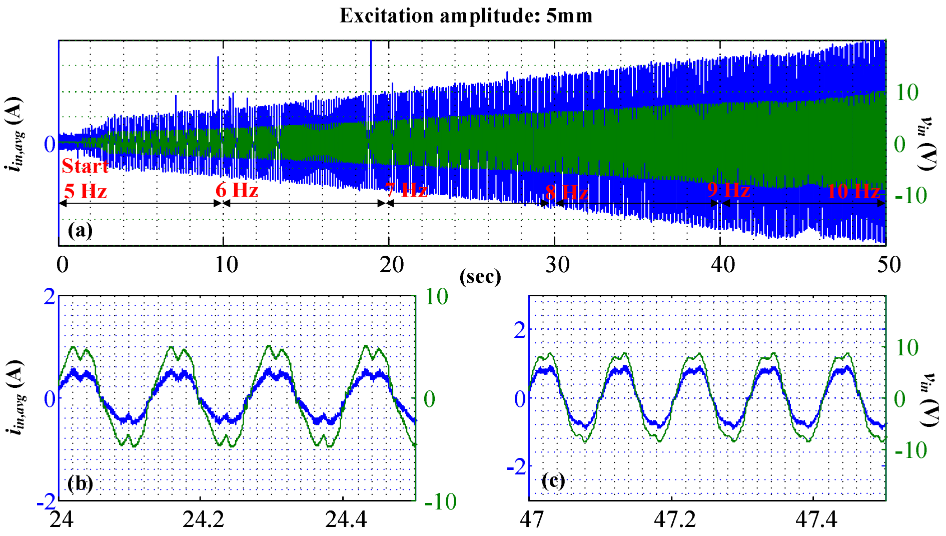

Figure 4-22: Sweeping of excitation frequency for nominal R_{in} = 10 Ω with detailed instantaneous waveform of v_{in} vs. $i_{in,avg}$ at (b) $f_i \approx 7.4$ Hz and (c) $f_i \approx 9.7$ Hz.

4.8. Average Harvested Power

To verify maximum power transfer we repeat the same procedure depicted in Figure 4-22 for R_{in}= 30 Ω, 50 Ω, 100 Ω, and 200 Ω, respectively. Both instantaneous power (left z axis) and average harvested power (right z axis) are depicted in Figure 4-23 for various R_{in} (x axis) swept from f_i= 3-8 Hz in 35 (sec) period.

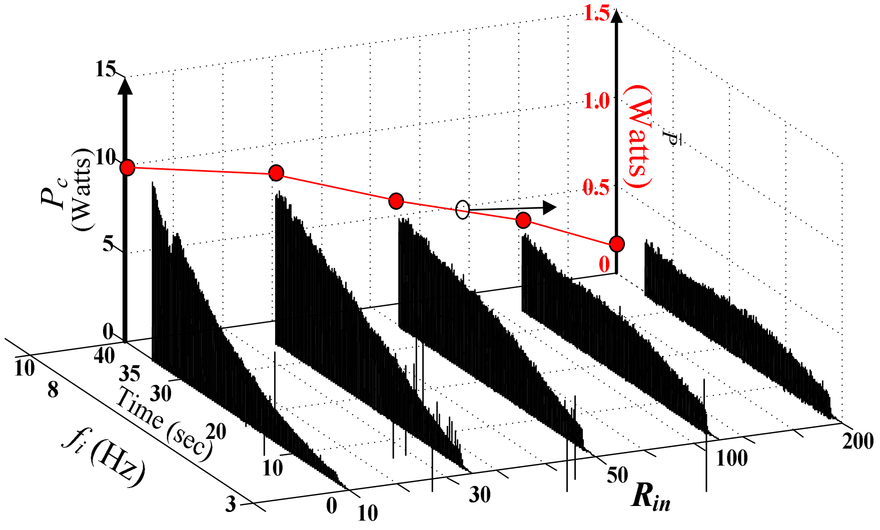

Figure 4-23: (left Z- axis): Instantaneous and (right Z- axis): average harvested power over the excited frequencies (i.e. 5- 10 Hz) in 35 (sec).

The average power is obtained using

$$\bar{P} = \left(f_e - f_s\right)^{-1} \int_{f_s}^{f_e} P_c df_i \tag{4-17}$$

where the difference between f_e and f_s indicates the range of excitation frequencies f_i. Referring to Figure 3-30, Figure 4-19, and Figure 4-23, the average harvested power $\bar{P}$ (right *z*- xis) indicates that the maximum power transfer takes place at R_{in}= 10 Ω (approximates the equivalent resistor of the DC machine coil) and lowest overall experimental efficiency η. Recalling Figure 3-30, this is a trade-off observed for power regeneration and conversion efficiency.

4.9. Chapter Summary

In this chapter, we proposed a sensorless direct AC/DC converter, operating in DCM, and investigated its performance through simulation and experiments. Variable resistor synthesis and the boundary for DCM operation were obtained along with the equivalent circuits in different switching modes. Through detailed analysis between converter line voltage and current, the realized converter current can be adjusted with respect to duty cycles of the bi-directional MOSFETs; hence, accomplishing adjustable resistor synthesis. Furthermore, the converter was placed under variable line frequency sweep for different values of synthesized resistors to demonstrate maximum power transfer. The purpose is to show the direct AC/DC converter, with the aforementioned benefits, when operating in DCM, is able to capture DC machine EMF, inducted by seismic ground excitation through a small- scale suspension prototype. Through comparison, it is noted the proposed topology offers a simplistic sensorless alternative, to that of SMR, for capturing seismic road energy.

Chapter 5.

Autonomous Start/ Stop Algorithm

An electric vehicle (EV) not only drains battery power when operating, it comsumes power even while idling or turned off. The power drain during these events may lead to battery power loss and contributes to reduction of EV range capacities, which makes shutting off the battery power drain beneficial over time. For a Tesla Model S, the "vampire power drain" consumes roughly 14 (km) of range capacity, which accumulates to roughly 8000 km per year, making the reduction of this power loss imperative for EV range extension [121]-[122]. The mitigation of the quiescent power drain contributes to the development of "Sleep Mode" on a Tesla Motor firmware. According to [121], the feature claims to reduce the quiescent power loss to 0.2%.

The proposed algorithm is independent of power converter topologies. The concept of adaptive turn on/off is applied to a SMR for demonstrating autonomous start/stop the circuit's operation for minimizing electrical quiescent power loss. The core of the concept is to detect the average instantaneous input power over certain time duration and decide the optimal starting time to operate the harvesting circuits (see Figure 5-1) for the purpose of ensuring "net-positive" instantaneous power harvesting. Similarly, as the harvester (i.e. electromagnetic suspension) steps out of "net- positive" region the algorithm will disable the operation of the harvesting circuits until line voltage v_x (and converter current i_{in}) reaches minimal level. The term "net-positive" will be explained in the following sections.

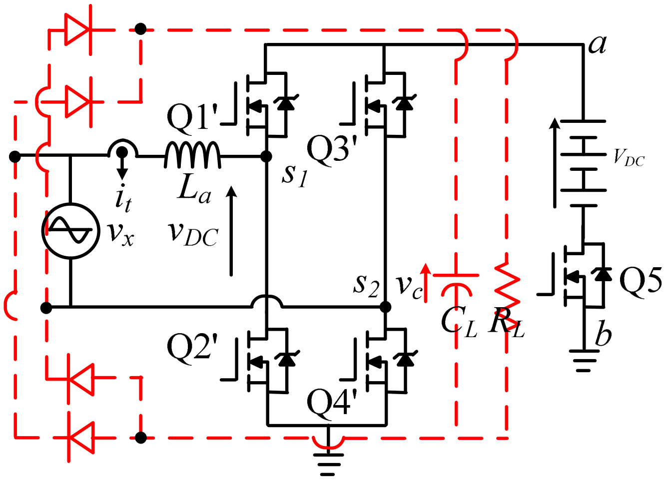

Figure 5-1: SMR (solid lines) with digitally implemented full- wave rectifier (dashed lines).

The term "net-positive" (i.e. P_{np}), defined in (5-1), is the difference between available instantaneous harvestable power P_{in} minus the sum of all power losses in a harvesting circuit P_{loss} (e.g. quiescent, conduction, and switching power losses)

$$P_{np}\left(t\right)=P_{in}\left(t\right)-P_{loss} \tag{5-1}$$

when $P_{np}> 0$ (Watts) the condition of net positive is met. As indicated in [122], an autonomous energy harvesting circuit should take into account quiescent power loss (P_q) while calculating total power loss during operation. In this work, P_{loss} for the SMR is the derived as

$$P_{loss}=P_{cond}+AP_{sw}+BP_{drv}+P_q+P_{aux} \tag{5-2}$$

where the coefficients A and B are dictated by number of MOSFETs and gate drivers. P_q is the IC quiescent power loss. P_{aux} is the auxiliary ICs operating power consumption. The total power loss is decomposed into conduction P_{cond}, switching P_{sw}, and gate driver losses P_{drv}, respectively. They are derived as

$$P_{cond}=i_t^2\left(aR_{ds,on}+R_{ESR}+R_{\text{int}}\right) \tag{5-3}$$

$$P_{sw} = 0.5 f_{sw} V_b i_t \left(t_{on} + t_{off} \right) \tag{5-4}$$

$$P_{drv} = V_{gs} Q_g f_{sw} \tag{5-5}$$

where $R_{ds,on}$, R_{ESR}, and R_{int} are the drain- source on- time resistor, inductor equivalent series resistor, and internal resistor of DC machine that represents the machine coil loss. i_t is the conducting current. V_b, t_{on}, and t_{off} are the MOSFET blocking voltage, turn- on and off time, respectively. V_{gs} and Q_g are the adopted MOSFET gate- source voltage and corresponding MOSFET gate charge. For the specific application, P_{sw} can be neglected due to level of i_t and switching delay time with adopted supply voltage (≈12 V).

As mentioned earlier, a Maxon DC motor (RE40-218011) with $R_{\text{int}} \approx 10\ \Omega > R_{ESR} >> R_{ds,on}$ was selected as the available power generator of the regenerative suspension prototype. In the proposed algorithm, when the SMR is disabled the load battery disconnects (after a time delay) the auxiliary circuits, therefore, making it possible for minimizing P_q. For the SMR prototype, $P_{aux}\approx$ 11 mw, which is explained in much details in later sections. Moreover, since $Q_g\approx$ 40 nC (at $V_{gs}= V_{ds}$ 12 V) for n- MOSFET IRFZ44N [124]. Hence, $P_{loss,r}$ can be simplified as

$$P_{loss,r} \approx i_t^2 R_{\text{int}} + P_{aux}\ . \tag{5-6}$$

According to (5-6), during road excitation, the main contributor of electrical efficiency degradation of the regenerative suspension is the internal resistance of the DC machine. While road excitation is absent (i.e. vehicle idle), the main contributor of overall efficiency degradation is the quiescent power loss P_q, which the proposed adaptive turn on/ off algorithm aims to mitigate.

In order to achieve the aforementioned requirements, an emulated full- wave rectifier (FWR) with parallel RC load has been digitally implemented (connected by dashed lines in Figure 5-1). The FWR line voltage v_x is estimated by DC machine encoder. Again, the purpose of FWR is for achieving “net- positive” operation and autonomous turn-off as the excitation voltage source exceeds and reduces to threshold level (e.g. vehicle braking/ idling), respectively. Averaging the rectified line voltage v_x results in the following

$$\overline{v}_x = \Delta T^{-1} \int_{t}^{t+\Delta T} \left| v_x \right| dt \tag{5-7}$$

where ΔT is nominal duration for averaging rectified v_x. In this work, $\Delta T = 1/60$ (sec). To ensure the SMR stays in "net- positive" region a threshold voltage $V_{th,,}$ is defined in the following

$$V_{th} = \sqrt{R_{in} \Delta T^{-1} \int_{t}^{t+\Delta T} P_{np} dt} \tag{5-8}$$

where R_{in} is the desired synthesized variable resistor value. The "net- positive" is established if $\overline{v}_x > V_{th}$. To illustrate, assuming sinusoidal v_x the time required for stepping in the "net- positive" region is derived as follows

$$T_c = \sin^{-1}\left(V_{th} \overline{v}_x^{-1} \right) \omega^{-1} \tag{5-9}$$

Similarly, as v_x reduces (e.g. vehicle idling) the time required to autonomously disable the auxiliary circuit is expressed as

$$T_d = -\tau \ln\left(V_{th} \overline{v}_x^{-1} \right) \tag{5-10}$$

where ω is the excitation angular frequency. The discharge time constant $\tau = R_L C_L$ is the product of load resistor and capacitor of the emulated FWR, respectively. It is worthy to note that since the battery is hard switched- off, by Q5 in Figure 5-1, from the auxiliary circuit, therefore it is imperative that it is performed after i_t has reduced to its' minimum level to prevent undesired current transients, which explains the purpose of (5-10) for delayed turn- off.

5.1. Auxiliary Circuit

In this work, the SMR prototype and the auxiliary circuit, powered by SLA battery, is depicted in Figure 5-2. The main components and ICs are tabulated in Table 5-1. As depicted in Figure 5-2 (a) and (b), the gate drivers are consisted of two floating type gate driver ICs (i.e. IR 2110), bootstrap capacitors c_b, and diodes D_b. According to [124]-[125], the IC quiescent power ≈ 5 mw (V_{DD}≈12 V). In addition, gate resistor R_g/ anti- parallel diodes D_g are placed for MOSFETs slow turn- on/ fast turn off. In addition, current sensing is accomplished by a bi- directional current sense amplifier (LT 1999- 20), which is supplied by a switch- mode voltage regulator (P7805), as shown in Figure 5-2 (c). The pin V_{out} indicates the bi- directional current reading. The pins V_{IN+} and V_{IN-} connect to current sense resistor R_s. The quiescent power of LT 1999-20 and P7805 are approximately as ≈ 7.5 mw (V^+≈ 5 V) and 0.45 mW, respectively [126]-[127]. The auxiliary circuit consumes total of P_{aus}≈ 11 mw and P_q≈ 13 mw.

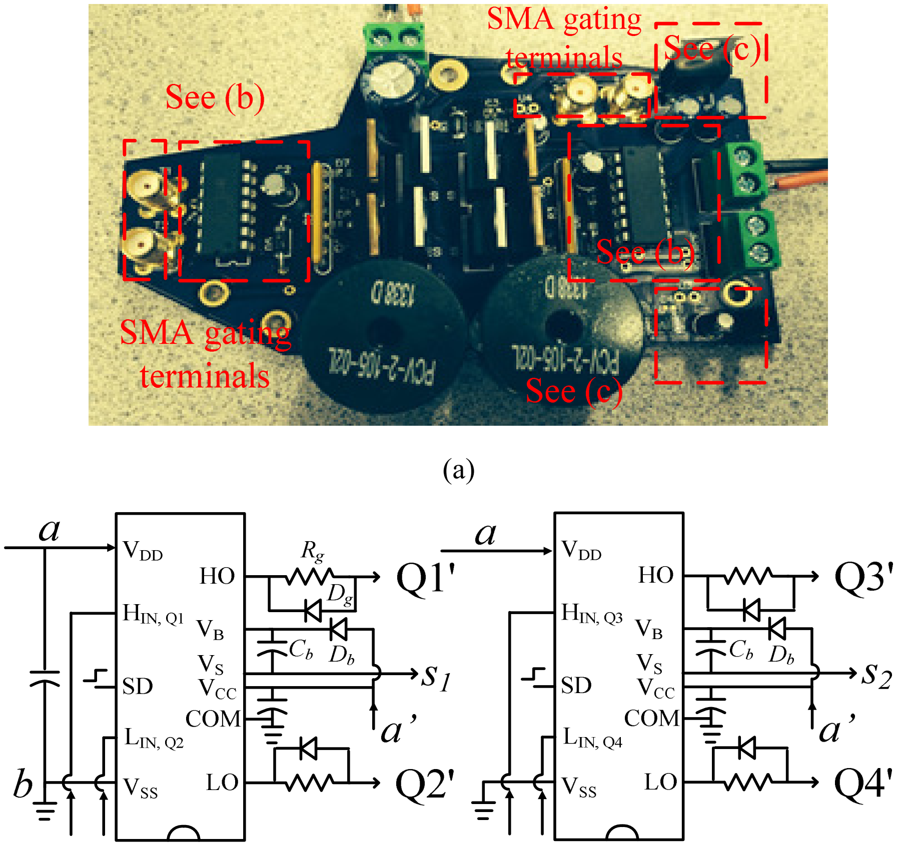

(a)

(b)

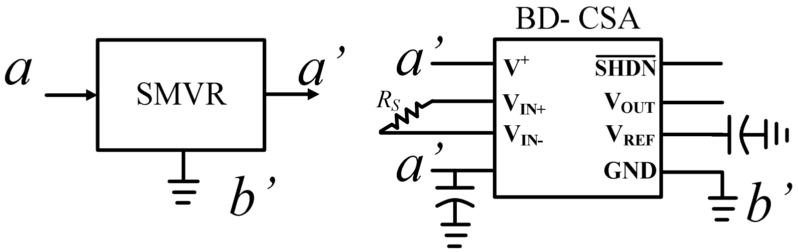

(c)

Figure 5-2: (a) SMR prototype and its' auxiliary circuit setup with (b) bootstrap gate driver (c) switch- mode voltage regulator, and current sense amplifier.

Table 5-1: Auxiliary circuit components and ICs

Component	Manufacture	Part number
Switch- Mode Voltage Regulator	CUIINC	P7805
Floating Gate drive	International Rectifier	IR 2110
Bi- directional Current Sense Amplifier	Linear Technology	LT 1999- 20
Gate Resistor (R_g)	Bourns	4608X-102-100LF
Bootstrap Diode (D_b)	AVX	478-7800-1
Bootstrap Capacitor (C_b)	Nichicon	493-11572-1
Current Sense Resistor (R_s)	VISHAY	WSLF-.025CT

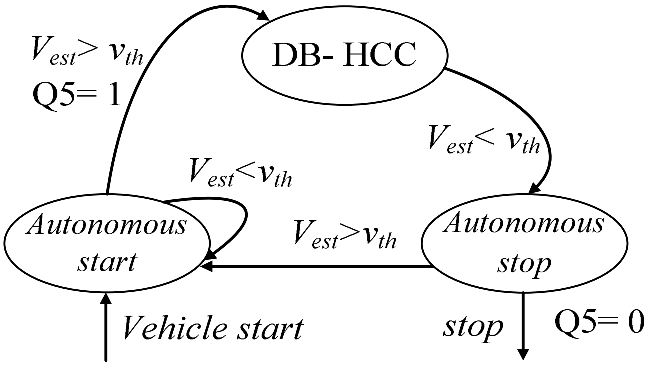

Figure 5-3: State diagram of DB- HCC with additional adaptive turn on/off state.

As indicated, “net- positive” is determined by P_{np}. Observing the DB- HCC state diagram with additional adaptive turn on/off state, in Figure 5-3, it is seen that the SMR is instructed to operate only when $P_{np} > 0$ (i.e. $\overline{v}_x > V_{th}$). As a result, Q5 is gated (see Figure 5-1), SD pin (i.e. pin 11 on IR2110) is pulled to ground, and SMR is operating in DB- HCC state diagram. During this process as $\overline{v}_x$ is monitored, when $\overline{v}_x < V_{th}$ (caused by either vehicle braking or idling) the operation of SMR terminates, Q5 is opened, and SD pin is gated. Consequently, the quiescent power loss is minimized.

5.2. Adaptive Algorithm with ISO-standard Drive Cycle

In this work, a nominal driving cycle has been architected in Figure 5-4. The driving cycle is essentially an International Standard Organization (ISO) 8608 Road class C roughness developed at different vehicle speeds. As indicated, the vehicle is nominally chosen to accelerate from static (0 km/h) to highest speed of 50 km/h and brake to idle.

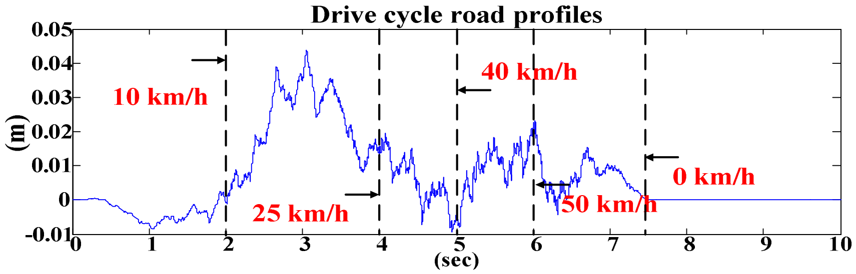

Figure 5-4: Variable speed class C roughness driving cycle.

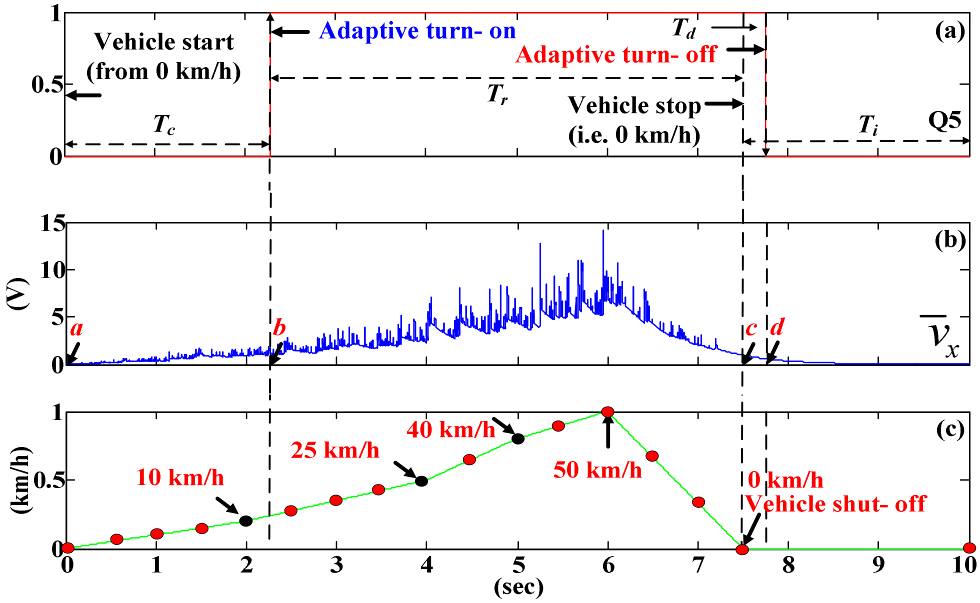

Figure 5-5: (a) Gating signal Q5 for powering auxiliary circuits, (b) rectified line voltage as result of (c) vehicle speed curve. Note: The dots indicate the time stamp of updating driving speed. Note: the 0 (sec) indicate the start of real-time data acquisition.

Referring to Figure 5-5 the SMR delays operation (point “*b*” in Figure 5-5 (b)), as Q5 is gated in Figure 5-5 (a), when the vehicle travels for ≈ 2.2 (sec) beyond 10 km/h (see Figure 5-5 (c)) with the rectified DC machine EMF $\overline{v}_x > V_{th}$, as indicated in Figure 5-5 (b). In other words, a harvesting circuit operates in the region of “*a-b*” consumes more power than the available power, therefore $P_{np}<0$. As a result, the purpose of energy harvesting is contradicted. Meaning, size of the region depends on the seismic environment and inherent loss of the harvesting circuit. Having a specific harvesting circuit, higher road classes lead to smaller region “*a-b*”. At point “*d*”, as $\overline{v}_x < V_{th}$ the harvesting circuit is turned off at roughly ≈ 0.25 (sec) in Figure 5-5 (c) after the vehicle reaches 0 km/hr, which is indicated by point “*c*” , shown in Figure 5-5 (b).

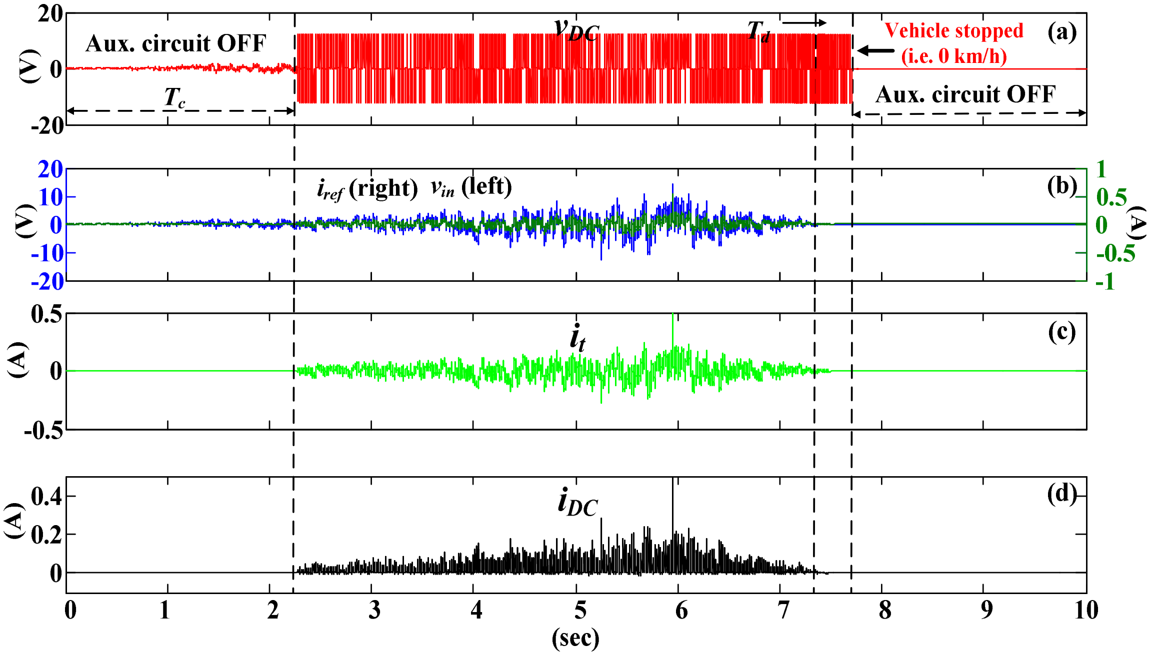

Figure 5-6: (a) inverter voltage, (b) left Y- axis: line voltage, right Y- axis: reference current, (c) controlled input current, and (d) rectified current for battery storage

The algorithm can also be verified by observing inverter voltage v_{DC}, line voltage v_{in}, reference current i_{ref}, input current i_{in}, and rectifier current i_{DC}. As indicated in Figure 5-6 (a) as $t< T_c$, v_{DC} equals to v_{in}. This represents an equivalent open- circuit, meaning not only i_t (shown in Figure 5-6 (c)) equals to 0 (A), theoretically, but also the auxiliary circuits are not in operation. As $t> T_c$, the SMR and its auxiliary circuits are in operation. In this work, a nominal R_{in}= 50 Ω has been chosen. In this mode, the i_{in} is controlled (by DB- HCC) to synthesize R_{in}= 50 Ω, which is verified through the corresponding amplitude ratio with v_{in} (shown in Figure 5-6 (b)). The rectified current i_{DC} for battery storage is depicted in Figure 5-6 (d). Lastly, as vehicle becomes idling the algorithm not only suspends the auxiliary circuit quiescent power consumption but also actuates the shut- down (SD) pin of the gate driver, resulting v_{DC} equals to 0 (V). For detailed instantaneous performance of the proposed autonomous algorithm with a Q- car electromagnetic suspension, a video of the real-time implementation was posted on [129].

5.3. Efficiency Enhancement

As indicated earlier, the ISO road profile is a stochastic process (non-deterministic), which implies that the induced motor EMF does not reach a pure sinusoidal state. Therefore, to calculate for power efficiency it is desired to normalize the averaged available power and power loss over the entire driving cycle. To obtain the available power P_{in} the sum of instantaneous input power have been normalized to the total driving cycle (see Figure 5-5 (a)) $T_{tot} = T_c + T_r + T_i = 10$ (sec) as follows

$$P_{in} = T_{tot}^{-1} \int_{t}^{t+T_r} v_x i_t \, dt \tag{5-11}$$

Recalling (5-2) - (5-6), the power efficiencies of the SMR with and without the autonomous start/ stop algorithm are written as the following, respectively

$$\eta_a \approx 1 - \left(T_{tot}^{-1} \left(\int_{t}^{t+T_r} i_t^2 R_{\text{int}} \, dt + T_r P_{aux} \right) + \left(T_d \right) T_{tot}^{-1} P_q \right) / \, P_{in} \tag{5-12}$$

$$\eta \approx 1 - \left(T_{tot}^{-1} \left(\int_{t}^{t+T_r} i_t^2 R_{\text{int}} \, dt + T_r P_{aux} \right) + \left(T_{tot} - T_r \right) T_{tot}^{-1} P_q \right) / \, P_{in} \tag{5-13}$$

where T_c, T_r, T_d, and T_i indicate the time of adaptive turn- on time, driving time, adaptive turn- off time, and vehicle idling time, respectively. The values for the nominal driving cycle are tabulated in Table 5-2.

Table 5-2: Composition of Driving Cycle Time.

Driving Cycle Time	Value (sec)
Total Driving Duration T_{tot}	10
Adaptive Turn- On T_c	2.2
Driving T_r	5.3
Adaptive Turn- Off T_d	0.2

Driving Cycle Time	Value (sec)
Vehicle Idling T_i	2.5
Rectfied Voltage Averaging Duration ΔT	1/60
Discharge Constant τ	0.01

For the adopted driving cycle, in Figure 5-5 (c), efficiency comparisons are tabulated in Table 5-3. The converter power efficiencies (SMR) efficiency are also obtained by omitting the source impedance of DC machine (i.e. $R_{\text{int}}= 0\ \Omega$). The results indicate that the efficiency improvement for ISO 8608 class C road profile is roughly 14%. The calculations are as follows

$$I \approx \left(\frac{\eta_a}{\eta}\right) - 1. \tag{5-14}$$

Table 5-3: Comparisons of conversion efficiency with start/ stop algorithm

SMR Efficiency	Power Efficiency	Improvements (I)
$\eta_a \approx 91\ \%$	$\eta_a \approx 76\ \%$	$I \approx 14\ \%$
$\eta \approx 80\ \%$	$\eta \approx 67\ \%$	$I \approx 14\ \%$

5.4. Chapter Summary

In this chapter, an autonomous start/ stop algorithm, for power conversion efficiency enhancement, wa implemented to provide a method to start/stop the harvesting circuit based on the estimated available power provided by the DC machine. Independent of vehicle velocity, the algorithm decides the optimum point for the converter to initiate harvesting behaviour by estimating the difference between its' auxiliary power consumption and available power induced by the seismic source (i.e. road). It is inherently adaptive to different road roughnesses. The converter operation is ceased, with a time delay (for avoiding undesired voltage/ current transients), after the induced EMF has diminished (e.g. vehicle idling). The start/ stop operation the exemplifing SMR is minaly accomplished by 1. Connect/ disconnect battery powered converter auxiliary circuits (i.e. current transducers, gate drivers, voltage regulators, etc) and 2. Gating the shutdown (SD) pins of MOSFETs gate driver ICs. To illustrate, the power conversion efficiency enhacement of 14% for the SMR has been documented on a class C variable speed drive cycle.

Chapter 6.

Conclusions and Suggestions for Future Work

A regenerative suspension system not only allows the possibility of road energy regeneration, but also, enables the control of vehicle sprung mass dynamics. The concept mitigates the conventional tradeoffs between active/semi-active (e.g. Sky-hook, RS) and passive control methods. Traditionally, active/semi-active control of a vehicle suspension system consumes electrical power (e.g. magic body control). Suspension passive control does not consume electrical power consumption; however, it can not accomplish variable control objectives. It is shown, throughout this work, the purposes of controlling suspension dynamics and harvesting road engeries can be met simultaneously, by the use of switched mode power electronics. The switched mode converters not only harvests the regenerated power, but also, provides variable levels of damping forces, in the electrical domain, to accomplished desired sprung mass control performance. To conclude my work, the summaries of the accomplished tasks are outlined in the following:

1. A regenerative suspension system prototype (i.e., SDOF system with ball- screw/DC machine) was illustrated, in great details, with respect to sprung mass dynamics and power harvesting. Through experimental results, different suspension dynamics scenarios were discussed. It is noted that the smaller the equivalent load resistor is, the higher amount of equivalent damping is provided to the suspension system. The FRF between both sprung mass acceleration and suspension relative displacements have been provided.

2. To achieve control and energy harvesting of a regenerative suspension system, a bi-directional SMR, controlled by DB-HCC, for variable resistors synthesis was designed, simulated, and fabricated. The purpose of the converter is twofold: (1) To present variable levels of electrical damping by adjusting the duty-cycles of the inverter, and (2) Harvest the dissipated energy by using the DC machine. To examine variable electrical

damping, we experimentally demonstrated regeneration and motoring modes. The results were demonstrated under variable excitation frequency and variable synthesized resistors. Moreover, the conversion efficiency of both mechanical suspension and power converter are identified. In addition, with the modelling of ISO road profile, the SMR is placed under both ISO 8608 class C and D excitation for variable damping provision and energy harvesting. According to the experimental waveforms, it is realized the converter controlled by DB- HCC is capable of regulating the desired line current, thus presenting the desired electrical damping.

3. In addition to constant damping, the converter is also implemented for applications in a semi-active control algorithm (i.e. Sky-hook). Conventionally, realizing semi- active control consumes power; the benefits of the proposed approach are towfolds: (1) Realize Sky-hook type damping, and (2) Regenerate energy. The FRF in terms of average regenerated power, sprung mass acceleration, and suspension relative displacement of the regenerative modified Sky-hook is obtained. In addition, the instantaneous waveforms indicating the converter responded to Sky-hook switching are documented. Also, the transient response of both Sky-hook and constant damping are presented. According to the experimental results, the DB- HCC controlled switch- mode rectifier (SMR) is able to generate equivalent electrical dampings, according to the Skyhook detection outcome, to the suspension system prototype. Therefore, it actively controls the suspension dynamic while mitigates the tradeoffs between suspension passive control (lack of control) and conventional active control (power consumption) methods.

4. A new direct AC/DC converter, operating in DCM, has been proposed. The purpose of the converter is to provide an alternative to the SMR for the purpose of energy harvesting. The benefits of such converter are simpler auxiliary circuit design, control, and smaller converter foot-print. Meaning, it is also suitable for very low available power applications (e.g. piezo-based transducer), since in such application the power consumption of auxiliary circuits should also be taken into account. Detailed analysis and modeling of the power converter in various switching modes were presented along with control strategy for input resistance synthesis. The experimental switching waveforms, such as line voltage, current, and rectified current correlated with that of theoretical analyses. The ability of regulating converter input resistance can be utilized

to emulate equivalent mechanical damping with regenerative capability. Experimental results of the converter connected to a regenerative vehicle suspension prototype for providing desired equivalent damping through vibrational energy regeneration is demonstrated. Furthermore, through synthesized resistor sweep over an extended range of frequency excitation the tradeoffs between power regeneration and conversion efficiency are also obtained experimentally.

5. An autonomous start/stop algorithm for energy harvesting power converter has been proposed. It allows power conversion efficiency enhancement by turning on/ off the circuit operation. According to the power level provided by the suspension prototype, the efficiency enhancement of 14 % is reported. In short, the algorithm ensures operations in positive conversion efficiency region. When the instantaneous road energy exceeds the converter quiescent power loss the converter starts to operate. When the vehicle idles, the algorithm shuts down the converter operation with a time delay for preventing undesired transients. The feature is synonymous to that of “Sleep- Mode” on a Tesla Model S firmware.

6.1. Suggestions for Future Work

6.1.1. A Bandwidth Enhanced Regenerative Suspension System

Recalling from Section 1.2, the generator will capture the maximum power at its resonant frequency. The potential future work outlined in the following have demonstrated great potentials in minimizing ground-tire relative displacements and maximizing energy harvesting in many applications [130]-[132]. In order to, overcome the limited bandwidth of linear resonant generator, the nonlinear strategies for the purpose of extending operating frequency region is examined. Several published works have focus on methods of expanding the power generation bandwidth by tuning the energy harvester where the excitation frequency is far from the mechanical resonance frequency. For example, a coupled shunt variable capacitor across a cantilevered piezoelectric beam for tuning the resonance frequency for the purpose of energy harvesting in implemented in [130]. The expansion of bandwidth for power generation by introduction parallel inductor and resistor to a piezoelectric based energy harvester is demonstrated in [131]. A linear spring compliance with added magnetic reluctance forces for providing a wider bandwidth of operation is experimentally demonstrated in [132]. A nonlinear mechanism with hardening stiffness, which provided a greater bandwidth, is investigated in [133].

6.1.2. Frequency Response and Jump phenomena

Recalling Section 2.1.2 one can construct the amplitude vs. frequency plot as shown in Figure 6-1. According to [133], by applying positive (negative) cubic stiffness force into a mass-spring system will result in bending of the amplitude frequency response curve, thus extending the available power bandwidth of the system into higher (lower) frequency region. It is seen that by adjusting the systems damping, stiffness, excitation amplitude different shapes and bending directions of the curves can be observed. It is realized that the curve bends left and right while having negative and positive α, also, the peak amplitude of the curve grows with increasing k and decreasing μ.

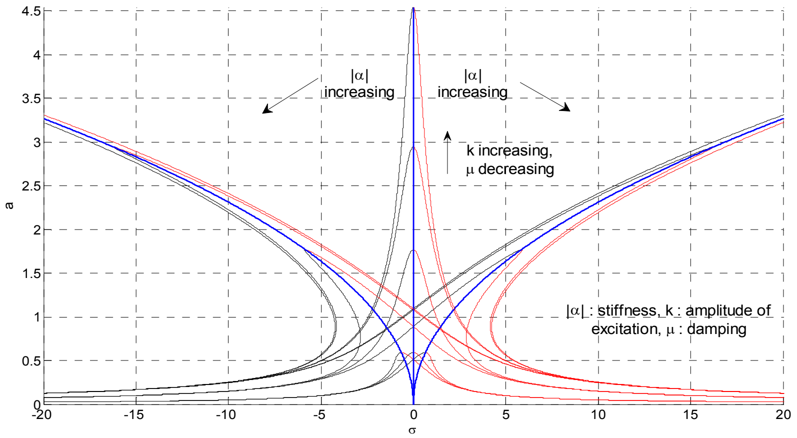

Figure 6-1: Amplitude vs. frequency curve with different nonlinearity, damping, and stiffness parameter values

The jump phenomena can be observed by looking at the amplitude vs. frequency curve in Figure 6-1 and Figure 6-2. To observe the phenomena one can increase the excitation frequency (with other parameters fixed) the response amplitude will follow the path of upper branch: B’→A→A’ by skipping the unstable region. When the same system with different initial conditions running at decreasing excitation frequency the response amplitude will follow the path of lower branch: A’→B→B’. The phenomenon is also investigated numerically (using ODE45) as shown in Figure 6-3. It is clearly shown with 2 different amplitude traces, which corresponds to the bending effect in analytical simulation. Also, the jump phenomenon is observed by forward and backward sweeping of the excitation frequency with 2 different initial conditions. It is seen that the blue curve increases in amplitude with increasing excitation frequency only until ≈2 the jump phenomena will occur and the amplitude jumps down to ≈0.4 and decreasing. When back sweeping the frequency the same phenomena occur but at a different point of excitation frequency. Therefore, from the numerical simulation it is shown that the unstable region shown in Figure 6-2 is not physically realizable.

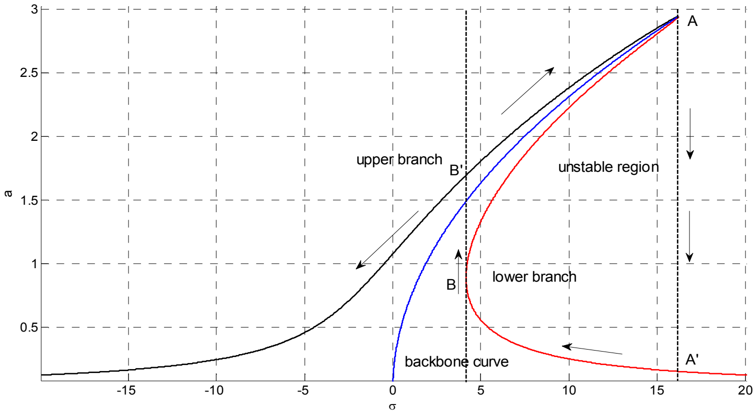

Figure 6-2: Amplitude vs. frequency curve indicating jump phenomena

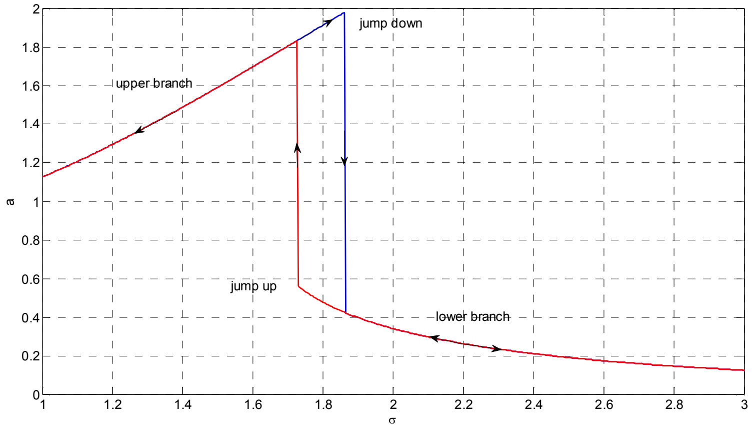

Figure 6-3: Numerical simulation of jump phenomena in amplitude

References

[1] United States Environmental Protection Agency, “Sources of Greenhouse Gas Emissions”, [online] 2014, http://www.epa.gov/climatechange/ghgemissions/sources.html (Accessed: 30 July 2014).

[2] D. Burtaw, M. Woerman, “ US Status of Climate Change Mitigation”, [online] 2014, http://www.rff.org/RFF/Documents/RFF-DP-12-48.pdf (Accessed: 30 July 2014).

[3] United States Department of Energy, “ One Million Electric Vehicle By 2015”, [online] 2014, http://www1.eere.energy.gov/vehiclesandfuels/pdfs/1_million_electric_vehicles_rpt.pdf (Accessed: 30 July 2014).

[4] CC Image courtesy of Maurizio Pesce on Flickr.

[5] CC Image courtesy of Steve Jurvetson on Flickr.

[6] M. Hanlon. “Audi's new magnetic semi-active suspension system”. Internet: http://www.gizmag.com/go/5752/, [Oct. 02, 2014].

[7] Hybrid Cars, “ Top 10 Most Fuel Efficient Non- Hybrid Cars- 2014”, [online] 2014, http://www.hybridcars.com/top-10-most-fuel-efficient-non-hybrid-cars-for-2014/11/ (Accessed: 30 July 2014).

[8] Hybrid Cars, “ 2013 Nissan Leaf Review”, [online] 2014, http://www.hybridcars.com/2013-nissan-leaf-review-video/(Accessed: 30 July 2014).

[9] Honda Power Equipement,"Wattage Calculator", [online] 2014, http://powerequipment.honda.com/generators/wattage-calculator (Accessed: 10 July 2014).

[10] Costco Wholesale," Nature Power High Output Monocrystalline Solar Panel", [online] 2014, http://www.costco.ca/Nature-Power-High-Output-Monocrystalline-Solar-Panel.product.100103950.html(Accessed: 30 July 2014).

[11] Go Power !," Recreational Vehicle and Marine Solar System and Inverter Selector ", [online] 2014, https://tools.carmanah.com/src.web/GoPowerCalculator.htm?state=RvDiv (Accessed: 30 July 2014).

[12] Mercedez Benz," Magic Body Control ", [online] 2014, http://www5.mercedes-benz.com/en/innovation/magic-body-control-s-class-suspension/ (Accessed: 30 July 2014).

[13] Suda, Yoshihiro, Shigeyuki Nakadai, and Kimihiko Nakano. "Hybrid suspension system with skyhook control and energy regeneration (development of self-powered active suspension)." *Vehicle system dynamics* 29.S1 (1998): 619-634.

[14] Lai, Chun Yu, and Wei-Hsin Liao. "Vibration control of a suspension system via a magnetorheological fluid damper." *Journal of Vibration and Control* 8.4 (2002): 527-547.

[15] Shen, Y., M. F. Golnaraghi, and G. R. Heppler. "Analytical and experimental study of the response of a suspension system with a magnetorheological damper." *Journal of intelligent material systems and structures* 16.2 (2005): 135-147.

[16] Yao, G. Z., Yap, F. F., Chen, G., Li, W. H., and Yeo, S. H., 2002, "MR damper and its application for semi-activecontrol of vehicle suspension system," *Mechatronics* 12, 963–973.

[17] Rakheja, S., and S. Sankar. "Vibration and shock isolation performance of a semi-active "on-off" damper." *Journal of Vibration and Acoustics* 107.4 (1985): 398-403.

[18] Peng, B. B., and X. Q. Huang. "A simulation test method for a half semi-active vehicle suspension based on the hierarchical modeling method." *Vehicular Electronics and Safety, 2006. ICVES 2006. IEEE International Conference on*. IEEE, 2006.

[19] Suda, Yoshihiro, Shigeyuki Nakadai, and Kimihiko Nakano. "Hybrid suspension system with skyhook control and energy regeneration (development of self-powered active suspension)." *Vehicle system dynamics* 29.S1 (1998): 619-634.

[20] Chen, Chao, and Wei-Hsin Liao. "A self-sensing magnetorheological damper with power generation." *Smart Materials and Structures* 21.2 (2012): 025014.

[21] Bianchi, N.; Bolognani, S.; Corte, D.D.; Tonel, F., "Tubular linear permanent magnet motors: an overall comparison," *Industry Applications, IEEE Transactions on* , vol.39, no.2, pp.466,475, Mar/Apr 2003.

[22] Jiabin Wang; Jewell, G.W.; Howe, D., "A general framework for the analysis and design of tubular linear permanent magnet machines," *Magnetics, IEEE Transactions on* , vol.35, no.3, pp.1986,2000, May 1999.

[23] Okada, Yohji, Sang-Soo Kim, and Keisuke Ozawa. "Energy regenerative and active control suspension." *ASME 2003 International Design Engineering Technical Conferences and Computers and Information in Engineering Conference*. American Society of Mechanical Engineers, 2003.

[24] Nakano, Kimihiko, Yoshihiro Suda, and Shigeyuki Nakadai. "Self-powered active vibration control using a single electric actuator." *Journal of Sound and Vibration* 260.2 (2003): 213-235.

[25] R.B. Goldner, P. Zerigan, "Electromagnetic Linear Generator and Shock Absorber", US Patent number 6952060, 2005.

[26] Tang, Xiudong, et al. "Improved design of linear electromagnetic transducers for large-scale vibration energy harvesting." *SPIE Smart Structures and Materials+ Nondestructive Evaluation and Health Monitoring*. International Society for Optics and Photonics, 2011.

[27] Wang, J.J.; Penamalli, G. P.; Lei Zuo, "Electromagnetic energy harvesting from train induced railway track vibrations," *Mechatronics and Embedded Systems and Applications (MESA), IEEE/ASME International Conference on* , vol., no., pp. 29-34, 2012.

[28] Peng Zeng; Khaligh, A., "A Permanent-Magnet Linear Motion Driven Kinetic Energy Harvester," *Industrial Electronics, IEEE Transactions on* , vol.60, no.12, pp.5737-5746, 2013.

[29] Hodgins, N.; Keysan, Ozan; McDonald, AS.; Mueller, M.A, "Design and Testing of a Linear Generator for Wave-Energy Applications," *Industrial Electronics, IEEE Transactions on* , vol.59, no.5, pp.2094,2103, May 2012.

[30] Gysen, B. L J; van der Sande, T.P.J.; Paulides, J. J H; Lomonova, E.A., "Efficiency of a Regenerative Direct-Drive Electromagnetic Active Suspension," *Vehicular Technology, IEEE Transactions on* , vol.60, no.4, pp.1384,1[3, May 2011.

[31] Xiudong Tang; Teng Lin; Lei Zuo, "Design and Optimization of a Tubular Linear Electromagnetic Vibration Energy Harvester," *Mechatronics, IEEE/ASME Transactions on* , vol.19, no.2, pp.615,622, April 2014.

[32] Martins, Ismenio, et al. "Permanent-magnets linear actuators applicability in automobile active suspensions." *Vehicular Technology, IEEE Transactions on* 55.1 (2006): 86-94.

[33] D. Karnopp, "Permanent Magnet Linear Motors Used as Variable Mechanical Dampers for Vehicle Suspensions," *Vehicle System Dynamics*, Vol. 18, pp. 187-200, 1989.

[34] Kim, Sang-Soo, and Yohji Okada. "Variable resistance type energy regenerative damper using pulse width modulated step-up chopper." *Journal of vibration and acoustics* 124.1 (2002): 110-115.

[35] Kawamoto, Y.; Suda, Y.; Inoue, H.; Kondo, T, "Modeling of electromagnetic damper for automobile suspension," *Journal of System Design and Dynamics*, 1(3): 524-535, 2007.

[36] Nakano, Kimihiko. "Combined type self-powered active vibration control of truck cabins." *Vehicle System Dynamics* 41.6 (2004): 449-473.

[37] Zuo, Lei, and Pei-Sheng Zhang. "Energy harvesting, ride comfort, and road handling of regenerative vehicle suspensions." *Journal of Vibration and Acoustics* 135.1 (2013): 011002.

[38] Zhongjie Li; Lei Zuo; Luhrs, G.; Liangjun Lin; Yi-Xian Qin, "Electromagnetic Energy-Harvesting Shock Absorbers: Design, Modeling, and Road Tests," *Vehicular Technology, IEEE Transactions on* , vol.62, no.3, pp. 1065-1074, 2013.

[39] Zuo, Lei, et al. "Design and characterization of an electromagnetic energy harvester for vehicle suspensions." *Smart Materials and Structures* 19.4 (2010): 045003.

[40] Li, Zhongjie, Zachary Brindak, and Lei Zuo. "Modeling of an electromagnetic vibration energy harvester with motion magnification." *ASME 2011 International Mechanical Engineering Congress and Exposition*. American Society of Mechanical Engineers, 2011.

[41] Choi, S. B., M. S. Seong, and K. S. Kim. "Vibration control of an electrorheological fluid-based suspension system with an energy regenerative mechanism." *Proceedings of the Institution of Mechanical Engineers, Part D: Journal of Automobile Engineering* 223.4 (2009): 459-469.

[42] Avadhany, Shakeel, et al. "Regenerative shock absorber." U.S. Patent No. 8,376,100. 19 Feb. 2013.

[43] Jazar, G. Nakhaie, et al. "Practical frequency and time optimal design of passive linear vibration isolation mounts." *Vehicle system dynamics* 39.6 (2003): 437-466.

[44] Narimani, A., M. E. Golnaraghi, and G. Nakhaie Jazar. "Frequency response of a piecewise linear vibration isolator." *Journal of Vibration and control* 10.12 (2004): 1775-1794.

[45] Jazar, N.G., Alkhatib, R., Golnaraghi, M.F., (2005) "Analytical Vibration Optimization of the Linear Quarter Car," *International Journal of Vehicle Mechanics and Mobility*, (*Vehicle System Dynamics*).

[46] Nakhaie Jazar, G., R. Alkhatib, and M. F. Golnaraghi. "Root mean square optimization criterion for vibration behaviour of linear quarter car using analytical methods." *Vehicle System Dynamics* 44.06 (2,006): 477-512.

[47] A.A. Shabana, *Theory of Vibration.* Springer Science & Business Media, 1995.

[48] Hartog, Den J. *et al*., Mechanical Vibrations, 4th edition. Dover Publications, 1985.

[49] Nayfeh A. H. and Mook D. T., *Nonlinear oscillations*, Wiley, New York, 2004.

[50] THK," Ball Screw General Catelog", [online] 2014, http://www.thk.com/sites/default/files/documents/uk_pdf/product/general/a/ee_A15.pdf (Accessed: 31 July 2014).

[51] de Rinaldis, A.; Scherpen, J. M A, "An Electrical Interpretation of Mechanical Systems via the Pseudo-inductor in the Brayton-Moser Equations," *Decision and Control, 2005 and 2005 European Control Conference. CDC-ECC '05. 44th IEEE Conference on* , vol., no., pp.5983,5988, 12-15 Dec. 2005.

[52] Gysen, B. L J; van der Sande, T.P.J.; Paulides, J. J H; Lomonova, E.A., "Efficiency of a Regenerative Direct-Drive Electromagnetic Active Suspension," *Vehicular Technology, IEEE Transactions on* , vol.60, no.4, pp.1384,1393, May 2011.

[53] Xiudong Tang; Teng Lin; Lei Zuo, "Design and Optimization of a Tubular Linear Electromagnetic Vibration Energy Harvester," *Mechatronics, IEEE/ASME Transactions on* , vol.19, no.2, pp.615,622, April 2014.

[54] Montazeri-Gh, M.; Soleymani, M.; Hashemi, S. "Impact of Traffic Conditions on the Active Suspension Energy Regeneration in Hybrid Electric Vehicles", *Industrial Electronics, IEEE Transactions on,* On page(s): 4546 - 4553 Volume: 60, Issue: 10, Oct. 2013.

[55] B. L. J. Gysen , J. J. H. Paulides , J. L. G. Janssen and E. A. Lomonova "Active electromagnetic suspension system for improved vehicle dynamics", *IEEE Trans. Veh. Technol.*, vol. 59, no. 3, pp.1156 -1163 2010.

[56] Ottman, G.K.; Hofmann, H.F.; Lesieutre, G.A., "Optimized piezoelectric energy harvesting circuit using step-down converter in discontinuous conduction mode," *Power Electronics, IEEE Transactions on* , vol. 18, no.2, pp. 696-703, 2003.

[57] Ottman, G.K.; Hofmann, H.F.; Lesieutre, G.A., "Optimized piezoelectric energy harvesting circuit using step-down converter in discontinuous conduction mode," *Power Electronics Specialists Conference, IEEE 33rd Annual*, vol.4, pp. 1988-1994, 2002.

[58] Ottman, G.K.; Hofmann, H.F.; Bhatt, A.C.; Lesieutre, G.A., "Adaptive piezoelectric energy harvesting circuit for wireless remote power supply," *Power Electronics, IEEE Transactions on* , vol.17, no.5, pp. 669-676, 2002.

[59] D'hulst, R.; Sterken, T.; Puers, R.; Deconinck, G.; Driesen, J., "Power Processing Circuits for Piezoelectric Vibration-Based Energy Harvesters," *Industrial Electronics, IEEE Transactions on* , vol.57, no. 12, pp. 4170-4177, 2010.

[60] Kim, Hyeoungwoo; Priya, S.; Stephanou, Harry; Uchino, Kenji, "Consideration of Impedance Matching Techniques for Efficient Piezoelectric Energy Harvesting," *Ultrasonics, Ferroelectrics and Frequency Control, IEEE Trans.*, vol.54, no. 9, pp. 1851-1859, 2007.

[61] Na Kong; Dong-Sam Ha, "Low-Power Design of a Self-powered Piezoelectric Energy Harvesting System With Maximum Power Point Tracking," *Power Electronics, IEEE Trans.*, vol.27, no.5, pp. 2298-2308, 2012.

[62] Shuo Cheng; Ying Jin; Yuan Rao; Arnold, D.P., "An Active Voltage Doubling AC/DC Converter for Low-Voltage Energy Harvesting Applications," *Power Electronics, IEEE Trans.* , vol.26, no.8, pp. 2258-2265, 2011.

[63] Lefeuvre, E.; Audigier, D.; Richard, C.; Guyomar, D., "Buck-Boost Converter for Sensorless Power Optimization of Piezoelectric Energy Harvester," *Power Electronics, IEEE Tran.*, vol. 22, no.5, pp. 2018-2025, 2007.

[64] Lesieutre G, Ottman G and Hofmann H., "Damping as a result of piezoelectric energy harvesting," *J. Sound Vib*. 269 991–1001, 2004.

[65] Zuo, Lei, and Xiudong Tang. "Large-scale vibration energy harvesting." *Journal of intelligent material systems and structures* 24, no. 11 (2013): 1405-1430.

[66] Kawamoto, Y.; Suda, Y.; Inoue, H.; Kondo, T, "Modeling of electromagnetic damper for automobile suspension," *Journal of System Design and Dynamics*, 1(3): 524-535, 2007.

[67] Zhongjie Li; Lei Zuo; Luhrs, G.; Liangjun Lin; Yi-Xian Qin, "Electromagnetic Energy-Harvesting Shock Absorbers: Design, Modeling, and Road Tests," *Vehicular Technology, IEEE Transactions on* , vol.62, no.3, pp. 1065-1074, 2013.

[68] Ung, C.; Moss, S.D.; Vandewater, L.A.; Galea, S.C.; Chiu, W.K.; Crew, G., "Energy harvesting from heavy haul railcar vibrations," *Intelligent Sensors, Sensor Networks and Information Processing, IEEE Int. Conference on* , vol., no., pp. 95-98, 2013.

[69] Tang, Xiudong, et al. "Improved design of linear electromagnetic transducers for large-scale vibration energy harvesting." *SPIE Smart Structures and Materials+ Nondestructive Evaluation and Health Monitoring*. International Society for Optics and Photonics, 2011.

[70] Wang, J.J.; Penamalli, G. P.; Lei Zuo, "Electromagnetic energy harvesting from train induced railway track vibrations," *Mechatronics and Embedded Systems and Applications (MESA), IEEE/ASME International Conference on* , vol., no., pp. 29-34, 2012.

[71] Peng Zeng; Khaligh, A., "A Permanent-Magnet Linear Motion Driven Kinetic Energy Harvester," *Industrial Electronics, IEEE Transactions on* , vol.60, no.12, pp.5737-5746, 2013.

[72] Hodgins, N.; Keysan, Ozan; McDonald, AS.; Mueller, M.A, "Design and Testing of a Linear Generator for Wave-Energy Applications," *Industrial Electronics, IEEE Transactions on* , vol.59, no.5, pp.2094,2103, May 2012.

[73] Sabzehgar, R.; Moallem, M., "Modelling and control of a boost converter for irregular input sources," *Power Electronics, IET* , vol.5, no.6, pp. 702-709, 2012.

[74] Xiudong Tang; Lei Zuo, "Simulation and experiment validation of simultaneous vibration control and energy harvesting from buildings using Tuned Mass Dampers," *American Control Conference (ACC), 2011* , vol., no., pp.3134,3139, June 29 2011-July 1 2011.

[75] Li, Peng, Chongxiao Zhang, Junyoung Kim, Liangyao Yu, and Lei Zuo., "Buck-boost converter for simultaneous semi-active vibration control and energy harvesting for electromagnetic regenerative shock absorber." In *SPIE Smart Structures and Materials+ Nondestructive Evaluation and Health Monitoring*, pp. 90570K-90570K. International Society for Optics and Photonics, 2014.

[76] International Organization for Standardization (ISO), *International Standard ISO 8608: Mechanical vibration - Road surface profiles - Reporting of measured data,* 1995.

[77] G. Rill, Road Vehicle Dynamics: Fundamentals and Modeling, CRC Press, 2011 .

[78] L. Zuo and P.-S. Zhang, "Energy harvesting, ride, comfort, and road handling of regenerative vehicle suspensions," *Journal of Vibration and Acoustics,* vol. 135, 2013.

[79] US Department of Engery, " Engery Efficiency & Renewable Enrtgy, " [online] 2014, http://www.fueleconomy.gov/feg/Find.do?action=sbs&id=32557(Accessed: 07 August 2014).

[80] Honda Power Equipement, "Wattage Calculator, " [online] 2014, http://powerequipment.honda.com/generators/wattage-calculator (Accessed: 10 July 2014).

[81] Montazeri-Gh, M.; Soleymani, M.; Hashemi, S., "Impact of Traffic Conditions on the Active Suspension Energy Regeneration in Hybrid Electric Vehicles," *Industrial Electronics, IEEE Transactions on* , vol.60, no.10, pp.4546,4553, Oct. 2013.

[82] Rodriguez, J.; Franquelo, L.G.; Kouro, S.; Leon, J.I; Portillo, R.C.; Prats, M.AM.; Perez, M.A, "Multilevel Converters: An Enabling Technology for High-Power Applications," *Proceedings of the IEEE* , vol.97, no.11, pp.1786,1817, Nov. 2009.

[83] Shukla, A.; Ghosh, A.; Joshi, A., "Hysteresis Modulation of Multilevel Inverters," *Power Electronics, IEEE Transactions on* , vol.26, no.5, pp.1396,1409, May 2011.

[84] Attaianese, C.; Di Monaco, M.; Tomasso, G., "High Performance Digital Hysteresis Control for Single Source Cascaded Inverters," *Industrial Informatics, IEEE Transactions on* , vol.9, no.2, pp.620,629, May 2013.

[85] YouTube. “Energy Harvesting from ISO standard road profile. Gdn0= 64e-6.”. *Youtube.com.* [Online]. Available http://y2u.be/sOXkBfvgI8A [Accessed with Firefox: 07 August 2014].

[86] Marchesoni, M., "High performance current control techniques for applications to multilevel high power voltage source inverters," *Power Electronics Specialists Conference, 1989. PESC '89 Record., 20th Annual IEEE* , vol., no., pp.672,682 vol.2, 26-29 Jun 1989.

[87] Dahono, P.A., "New hysteresis current controller for single-phase full-bridge inverters," *Power Electronics, IET* , vol.2, no.5, pp.585,594, Sept. 2009.

[88] Dahono, P.A., "New current controllers for single-phase full-bridge inverters," *Power System Technology, 2004. PowerCon 2004. 2004 International Conference on* , vol.2, no., pp.1757,1762 Vol.2, 21-24 Nov. 2004.

[89] Zare, F.; Ledwich, G., "A hysteresis current control for single-phase multilevel voltage source inverters: PLD implementation," *Power Electronics, IEEE Transactions on* , vol.17, no.5, pp.731,738, Sep 2002.

[90] Gautam, S.; Gupta, R., "Switching Frequency Derivation for the Cascaded Multilevel Inverter Operating in Current Control Mode Using Multiband Hysteresis Modulation," *Power Electronics, IEEE Transactions on* , vol.29, no.3, pp.1480,1489, March 2014.

[91] Loh, P. C.; Bode, G.H.; Tan, P-C, "Modular hysteresis current control of hybrid multilevel inverters," *Electric Power Applications, IEE Proceedings -* , vol.152, no.1, pp.1,8, 7 Jan. 2005.

[92] Purohit, P.; Dubey, M., "Analysis and design of hysteresis current controlled multilevel inverter fed PMSM drive," *Electrical, Electronics and Computer Science (SCEECS), 2014 IEEE Students' Conference on* , vol., no., pp.1,5, 1-2 March 2014.

[93] Bode, G.H.; Holmes, D.G., "Hysteresis current regulation for single-phase multilevel inverters using asynchronous state machines," *Industrial Electronics Society, 2003. IECON '03. The 29th Annual Conference of the IEEE* , vol.2, no., pp.1203,1208 Vol.2, 2-6 Nov. 2003.

[94] Shukla, A.; Ghosh, A.; Joshi, A. "Improved Multilevel Hysteresis Current Regulation and Capacitor Voltage Balancing Schemes for Flying Capacitor Multilevel Inverter", *Power Electronics, IEEE Transactions on,* On page(s): 518 - 529 Volume: 23, Issue: 2, March 2008.

[95] Poh Chiang Loh; Bode, G.H.; Holmes, D.G.; Lipo, T.A, "A time-based double-band hysteresis current regulation strategy for single-phase multilevel inverters," *Industry Applications, IEEE Transactions on* , vol.39, no.3, pp.883,892, May-June 2003.

[96] Loh, P.C.; Holmes, D.G.; Fukuta, Y.; Lipo, T.A, "A reduced common mode hysteresis current regulation strategy for multilevel inverters," *Applied Power Electronics Conference and Exposition, 2003. APEC '03. Eighteenth Annual IEEE* , vol.1, no., pp.576,582 vol.1, 9-13 Feb. 2003.

[97] Xue, X.D.; Cheng, K.W.E.; Zhang, Z.; Lin, J.K.; Wang, D.H.; Bao, Y.J.; Wong, M.K.; Cheung, N. "Investigation on parameters of automotive electromagnetic active suspensions", *Power Electronics Systems and Applications (PESA), 2011 4th International Conference on,* On page(s): 1 – 5.

[98] Xue, X.D.; Cheng, K.W.E.; Zhang, Z.; Lin, J.K.; Wang, D.H.; Bao, Y.J.; Wong, M.K.; Cheung, N. "Study of art of automotive active suspensions", *Power Electronics Systems and Applications (PESA), 2011 4th International Conference on,* On page(s): 1 – 7.

[99] Gysen, B.L.J.; van der Sande, T.P.J.; Paulides, J.J.H.; Lomonova, E.A. "Efficiency of a Regenerative Direct-Drive Electromagnetic Active Suspension", *Vehicular Technology, IEEE Transactions on,* On page(s): 1384 - 1393 Volume: 60, Issue: 4, May 2011.

[100] Hsieh, Chen-Yu; Huang, Bo; Golnaraghi, Farid; Moallem, Mehrdad, "Sky-Hook Control for a Regenerative Suspension System," *Vehicular Technology Conference (VTC Fall), 2014 IEEE 80th* , vol., no., pp.1,6, 14-17 Sept. 2014.

[101] Karnopp, Dean, Michael J. Crosby, and R. A. Harwood. "Vibration control using semi-active force generators." *Journal of Manufacturing Science and Engineering* 96.2 (1974): 619-626.

[102] Liu, Y., T. P. Waters, and M. J. Brennan. "A comparison of semi-active damping control strategies for vibration isolation of harmonic disturbances."*Journal of Sound and Vibration* 280.1 (2005): 21-39.

[103] Fallah, M.; Bhat, R.B.; Wen-Fang Xie, "Optimized Control of Semi active Suspension Systems Using H_∞ Robust Control Theory and Current Signal Estimation," *Mechatronics, IEEE/ASME Transactions on* , vol.17, no.4, pp.767,778, Aug. 2012.

[104] Bai, Xian-Xu; Wereley, Norman M., "A fail-safe magnetorheological energy absorber for shock and vibration isolation," *Journal of Applied Physics*, vol.115, no.17, pp.17B535,17B535-3, May 2014.

[105] Sankaranarayanan, V.; Emekli, M.E.; Gilvenc, B.A.; Guvenc, L.; Ozturk, E.S.; Ersolmaz, E.S.; Eyol, I.E.; Sinal, M., "Semiactive Suspension Control of a Light Commercial Vehicle," *Mechatronics, IEEE/ASME Transactions on* , vol.13, no.5, pp.598,604, Oct. 2008.

[106] Zapateiro, M.; Pozo, F.; Karimi, H.R.; Ningsu Luo "Semiactive Control Methodologies for Suspension Control With Magnetorheological Dampers", *Mechatronics, IEEE/ASME Transactions on,* On page(s): 370 - 380 Volume: 17, Issue: 2, April 2012.

[107] J. J. H. Paulides , L. Encica , E. A. Lomonova and A. J. A. Vandenput "Design considerations for a semi-active electromagnetic suspension system", *IEEE Trans. Magn.*, vol. 42, no. 10, pp.3446 -3448 2006.

[108] Rakheja, S., and S. Sankar. "Vibration and shock isolation performance of a semi-active "on-off" damper." *Journal of Vibration, Acoustics Stress and Reliability in Design* 107, no. 4 (1985): 398-403.

[109] Shen, Y., M. F. Golnaraghi, and G. R. Heppler. "Semi-active vibration control schemes for suspension systems using magnetorheological dampers." *Journal of Vibration and Control* 12, no. 1 (2006): 3-24.

[110] Bolandhemmat, Hamidreza, Christopher M. Clark, and Farid Golnaraghi. "Development of a systematic and practical methodology for the design of vehicles semi-active suspension control system." *Vehicle System Dynamics*, 48, no. 5 (2010): 567-585.

[111] Bolandhemmat, Hamidreza, Christopher M. Clark, and Farid Golnaraghi. "Toward Systematic Approaches to Design and Implement Vehicles Semi-Active Control Systems." *Computer Science and Software Engineering* (2008): 58.

[112] Xue, X.D.; Cheng, K.W.E.; Zhang, Z.; Lin, J.K.; Wang, D.H.; Bao, Y.J.; Wong, M.K.; Cheung, N. "Investigation on parameters of automotive electromagnetic active suspensions", *Power Electronics Systems and Applications (PESA), 2011 4th International Conference on,* On page(s): 1 – 5.

[113] Xue, X.D.; Cheng, K.W.E.; Zhang, Z.; Lin, J.K.; Wang, D.H.; Bao, Y.J.; Wong, M.K.; Cheung, N. "Study of art of automotive active suspensions", *Power Electronics Systems and Applications (PESA), 2011 4th International Conference on,* On page(s): 1 – 7.

[114] Gysen, B.L.J.; van der Sande, T.P.J.; Paulides, J.J.H.; Lomonova, E.A. "Efficiency of a Regenerative Direct-Drive Electromagnetic Active Suspension", *Vehicular Technology, IEEE Transactions on,* On page(s): 1384 - 1393 Volume: 60, Issue: 4, May 2011.

[115] Dayal, R.; Dwari, S.; Parsa, L., "Design and Implementation of a Direct AC–DC Boost Converter for Low-Voltage Energy Harvesting," *Industrial Electronics, IEEE Transactions on* , vol.58, no.6, pp.2387,2396, June 2011.

[116] D.M. Mitchell, "AC-DC Converter having an improved power factor," U.S. Patent 4,412,277, Oct. 25, 1983.

[117] Huber, L.; Yungtaek Jang; Jovanovic, M.M., "Performance Evaluation of Bridgeless PFC Boost Rectifiers," *Power Electronics, IEEE Transactions*, vol. 23, no. 3, pp. 1381-1390, 2008.

[118] Bowden, J, Clare, L & Burrow, S 2010, ‘Unity Power Factor Correction For Electromagnetic Vibration Harvesters’, *PowerMEMS 2010 Leuven Belgium*., pp. 151 – 154, 2010.

[119] Fairchild Semiconductor, Appl. Note 9721.

[120] Linear Technology, “LT 4356-1/ LT 4356-2 Surge Stopper” LT 4356 datasheet.

[121] Green Car Reports, “Life With 2013 Tesla Model S: 'Vampire' Thirst For Electricity At Night?”, [online] 2013, http://www.greencarreports.com/news/1082949_life-with-2013-tesla-model-s-vampire-thirst-for-electricity-at-night. (Accessed: 5 Aug 2014).

[122] ECOMENTO, “Tesla update stops the Model S losing charge when it’s turned off”, [online] 2013, http://ecomento.com/2013/08/19/tesla-update-stops-the-model-s-losing-charge-when-its-turned-off/. (Accessed: 19 Aug 2014).

[123] Szarka, G.D.; Burrow, S.G.; Stark, B.H., "Ultralow Power, Fully Autonomous Boost Rectifier for Electromagnetic Energy Harvesters," *Power Electronics, IEEE Transactions on* , vol.28, no.7, pp.3353,3362, July 2013.

[124] International Rectifier, “HEXFET Power MOSFET” IRFZ44N datasheet.

[125] International Rectifier, “XPHASE3^{TM} Dual Phase IC” IR 3527 datasheet.

[126] International Rectifier, “HIGH AND LOW SIDE DRIVER” IR 2110 datasheet.

[127] Linear Technology, “High Voltage, Bi – directional Current Sense Amplifier” LT 1999 datasheet.

[128] CUIINC, “NON- ISOLATED SWITCHING REGULATOR” P 7805- S datasheet.

[129] YouTube. “SMR Autonamous Start/ Stop Under ISO 8608 Excitation (2)”. *Youtube.com.* [Online]. Available http://y2u.be/udyR4KQSnhY [Accessed with Firefox: 10 July 2014].

[130] Wu W J, Chen Y Y, Lee B S, He J J and Peng Y T 2006, Tunable resonant frequency power harvesting devices *Proc. SPIE* 6169 61690A1- 8.

[131] Renno J M, Daqaq M F and Inman D J 2009 On the optimal energy harvesting from a vibration source *J. Sound Vib*. 320 386- 405

[132] Tang, Lihua, Yaowen Yang, and Chee Kiong Soh. "Toward broadband vibration-based energy harvesting." *Journal of Intelligent Material Systems and Structures* 21.18 (2010): 1867-1897.

[133] Burrow, S. G., et al. "Vibration energy harvesters with non-linear compliance."*The 15th International Symposium on: Smart Structures and Materials & Nondestructive Evaluation and Health Monitoring*. International Society for Optics and Photonics, 2008.